2019

MECHANICAL PROPERTIES AND DEGRADATION OF HIGH CAPACITY BATTERY ELECTRODES: FUNDAMENTAL UNDERSTANDING AND COPING STRATEGIES

Yikai Wang
University of Kentucky, ywa286@g.uky.edu
Author ORCID Identifier:
https://orcid.org/0000-0002-1156-0324
Digital Object Identifier: https://doi.org/10.13023/etd.2019.315

STUDENT AGREEMENT:

I represent that my thesis or dissertation and abstract are my original work. Proper attribution has been given to all outside sources. I understand that I am solely responsible for obtaining any needed copyright permissions. I have obtained needed written permission statement(s) from the owner(s) of each third-party copyrighted matter to be included in my work, allowing electronic distribution (if such use is not permitted by the fair use doctrine) which will be submitted to UKnowledge as Additional File.

I hereby grant to The University of Kentucky and its agents the irrevocable, non-exclusive, and royalty-free license to archive and make accessible my work in whole or in part in all forms of media, now or hereafter known. I agree that the document mentioned above may be made available immediately for worldwide access unless an embargo applies.

I retain all other ownership rights to the copyright of my work. I also retain the right to use in future works (such as articles or books) all or part of my work. I understand that I am free to register the copyright to my work.

REVIEW, APPROVAL AND ACCEPTANCE

The document mentioned above has been reviewed and accepted by the student's advisor, on behalf of the advisory committee, and by the Director of Graduate Studies (DGS), on behalf of the program; we verify that this is the final, approved version of the student's thesis including all changes required by the advisory committee. The undersigned agree to abide by the statements above.

Yikai Wang, Student

Dr. Yang-Tse Cheng, Major Professor

Dr. Matthew Beck, Director of Graduate Studies

MECHANICAL PROPERTIES AND DEGRADATION OF HIGH CAPACITY BATTERY ELECTRODES: FUNDAMENTAL UNDERSTANDING AND COPING STRATEGIES

DISSERTATION

A dissertation submitted in partial fulfillment of the
requirements for the degree of Doctor of Philosophy in the
College of Engineering at the University of Kentucky

By
Yikai Wang
Lexington, Kentucky
Director: Dr. Yang-Tse Cheng, Professor of Chemical and Materials Engineering
Lexington, Kentucky
2019

ABSTRACT OF DISSERTATION

MECHANICAL PROPERTIES AND DEGRADATION OF HIGH CAPACITY BATTERY ELECTRODES: FUNDAMENTAL UNDERSTANDING AND COPING STRATEGIES

Rechargeable lithium ion and lithium (Li) metal batteries with high energy density and stability are in high demand for the development of electric vehicles and smart grids. Intensive efforts have been devoted to developing high capacity battery electrodes. However, the known high capacity electrode materials experience fast capacity fading and have limited cycle life due to electromechanical degradations, such as fracture of Si-based electrodes and dendrite growth in Li metal electrodes. A fundamental understanding of electromechanical degradation mechanisms of high capacity electrodes will provide insights into strategies for improving their electrochemical performance. Thus, this dissertation focuses on mechanical properties, microstructure changes, and degradation mechanisms of Si composite electrodes and Li metal electrodes. Based on these findings, possible coping strategies are proposed to improve the cycling stability of both electrodes.

The poor cycling life of Si-based electrodes is caused by the repeated lithiation/delithiation-induced huge volumetric change in Si particles, which leads to the fracture of particles, excessive formation of solid electrolyte interphase on the newly exposed surface, as well as the loss of electronic conductivity between Si particles and the conductive matrix. The expansion/contraction of Si particles during cycling also causes the changes in the mechanical properties, microstructure, and porosity of Si composite electrodes. Understanding the relationship between mechanical property evolution, microstructure degradation, and capacity fading is essential for the design of Si composite electrodes. Using an environmental nanoindentation system, *in situ* microscope cell, and electrochemical impedance spectroscopy, I investigated the mechanical properties, cracking behavior, and lithiation/delithiation kinetics of Si composite electrodes made with different polymeric binders, including polyvinylidene fluoride, Nafion, sodium-carboxymethyl cellulose, and sodium-alginate, in their realistic working environment. The mechanical property evolution is determined by the state-of-charge, porosity, irreversible volume change, and mechanical behavior of binders. Periodical crack opening and closing happens in Si composite electrodes prepared with binders that have strong adhesion with Si. Mechanical degradations, *e.g.*, irreversible volume change, cracking, and debonding between binders and Si particles, are correlated with the evolution of lithiation/delithiation kinetics and the capacity fading of Si composite electrodes. Based on these findings, a partial charging approach is proposed and confirmed experimentally to improve the cycling stability of Si composite electrodes.

Li metal electrodes suffer from the low Coulombic efficiency, high electrochemical reactivity with the electrolytes, and the safety hazards caused by the uncontrollable dendrite growth during cycling. Mechanical suppression by using solid electrolytes and artificial SEI is a promising strategy to inhibit the formation of Li dendrites. Mechanical properties of bulk and mossy Li are required for designing mechanical inhibitors and improving the stability of the Li | inhibitor interface. Using an environmental nanoindentation system, I studied the mechanical behavior, especially the time-dependent behavior, of bulk Li and porous mossy Li at ambient temperature. By combining finite element (FE) modeling with experiments, a constitutive law was determined for the viscoplastic deformation of Li metal. FE modeling also demonstrates that the elasticity has a negligible influence on the indentation deformation of bulk Li. Flat punch indentation measurements showed that mossy Li has significantly higher deformation and creep resistance than bulk Li despite of its porous microstructure. The mechanical parameters of bulk and mossy Li may be helpful to develop of dendrite-free Li metal electrodes.

KEYWORDS: Silicon Electrodes, Lithium Metal Electrode, Polymeric Binders, Degradation, Mechanical Properties, Indentation

Yikai Wang

(Name of Student)

04/29/2019

Date

MECHANICAL PROPERTIES AND DEGRADATION OF HIGH CAPACITY BATTERY ELECTRODES: FUNDAMENTAL UNDERSTANDING AND COPING STRATEGIES

By
Yikai Wang

Dr. Yang-Tse Cheng
Director of Dissertation

Dr. Matthew Beck
Director of Graduate Studies

04/29/2019
Date

Dedicated to my family

.

ACKNOWLEDGMENTS

First, and most of all, I would like to express my heartiest gratitude to my advisor, Prof. Yang-Tse Cheng, for his precious suggestions, continuous encouragements, and great support in the past four years. His critical thought, rigorous attitude towards scientific problems, and active lifestyle also benefit my life a lot.

I am also grateful to my committee members, Drs. Xingcheng Xiao, Y. Charles Lu, Beth S. Guiton, and Jonathan T. Pham, and the Outside Examiner, Dr. Daniel Pack, for their time, efforts, and suggestions on my research and dissertation.

I would like to express my deep sense of thanks to my lab mates and friends, Dingying Dang, Jiazhi Hu, Shuang Gao, Xiaowen Zhan, Ming Wang, and Andrew Meyer, former group members, Drs. Juchuan Li, Qinglin Zhang, Jiagang Xu, Jie Pan, Tao Chen, and Baleegh Alobaid, and our visiting scholars, Dr. Dawei Li and Yan Sun for their help and collaborations.

Specially, I would like to thank Dr. Chunmei Ban at Virginia Tech for offering me a three-month visit at National Renewable Energy Laboratory (NREL) in 2018 and Dr. Xingcheng Xiao at General Motors R&D Center for supportive collaborations. Professors and staff members at University of Kentucky, including Dr. Doo Young Kim, Nancy Miller, Dr. Nicolas Briot, and Dr. Dali Qian, are also acknowledged for their help with experiments.

I would also acknowledge the funding agencies, NSF and DOE, for supporting this dissertation.

Finally, I would like to thank my parents and sisters for their support.

TABLE OF CONTENTS

LIST OF TABLES

LIST OF FIGURES

CHAPTER 1. INTRODUCTION

Lithium ion batteries (LIBs) and lithium metal-based (Li-air and Li-sulfur) batteries have higher energy density and power density than other battery systems, hence are promising in various applications, especially electric vehicles (EVs) and grid-scale energy storages. Motivated by the energy storage market, Si electrodes and Li metal electrodes are favorable choices for next-generation batteries due to their ultrahigh capacity. However, both of them suffer electrochemical-mechanical degradation, which lead to safety issues, fast capacity fading, and short cycle life of batteries.

1.1 Lithium Ion Batteries (LIBs)

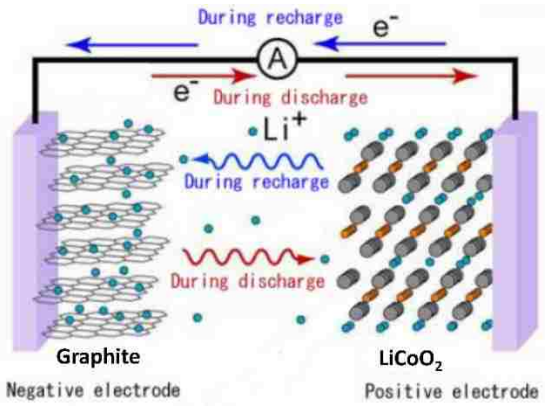

Figure 1.1. A schematic diagram of a typical LIB cell based on a graphite negative electrode and a $LiCoO_2$ positive electrodes [1].

Typically, a lithium ion battery cell consists of a positive electrode, a negative electrode, a separator, and liquid organic electrolyte, as shown in Figure 1.1. Typical positive electrode materials are transition metallic oxides, including layer structure $LiCoO_2$ and $LiNiO_2$, spinel structure $LiMn_2O_4$, olivine structure $LiFePO_4$ and their derivatives (such as $LiNi_xCo_yMn_zO_2$, NCM). Negative electrode materials include graphite, graphene, Si, SiO_x, and Sn. The separator (mesoporous polypropylene membrane) is to prevent short circuit by separating the negative and positive electrodes apart. The electrolyte is composed of lithium salt (*e.g.*, $LiPF_6$ or LiTFSI) and organic solvent, such as diethyl carbonate (DEC) and ethylene carbonate (EC). The electrolyte is required to be ionically conductive and electronically insulative [2, 3].

The working mechanism of LIBs is the reversible Li ion intercalation and deintercalation of either the positive electrode or the negative electrode. Meanwhile, electrons transfer between the positive and the negative electrodes through the external circuit. The voltage of a LIB cell is determined by the chemical potential difference between the positive and the negative electrodes.

1.2 Lithium Metal-Based Rechargeable Batteries

Li metal-based rechargeable batteries use Li metal as the negative electrode. Li-sulfur (Li-S) batteries and Li-air (or Li-O_2) batteries are two major categories of Li metal-based rechargeable batteries.

Li-sulfur (Li-S) batteries

As shown in Figure. 1.2 (a), a typical Li-S cell consists of a Li metal negative electrode, a porous separator, organic electrolyte, and a sulfur-based positive electrode. Its working mechanism is based on the electrochemical reaction between Li and sulfur. Major challenges of Li-S batteries are (1) poor electronic conductivity of S, Li-S compounds, especially insulating nature of Li_2S, (2) the solubility of polysulfides (Li_2Si_x, $3 < x < 8$) in to the electrolyte, and (3) the growth of Li dendrites [4-6].

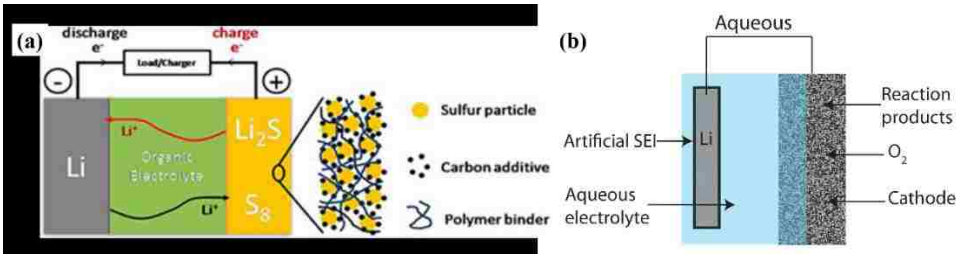

Figure 1.2. Schematics of (a) a typical Li-S cell [4] and (b) a typical aqueous Li-air cell [7].

Li-air batteries

Figure 1.2 (b) shows a typical configuration of a Li-air cell. It consists of a Li metal electrode, a separator, electrolyte, and an oxygen positive electrode. Based on the electrolyte, Li-air batteries can be categorized into 4 types: aqueous, non-aqueous, hybrid, and solid-state batteries [8, 9]. The specific electrochemistry of Li-air batteries depends on the electrolyte. In general, during discharging, the Li metal negative electrode is oxidized;

O_2 is reduced in the porous positive electrode. Primary difficulties in the application of Li-air batteries are the poor stability and rate capability as well as the safety hazard from Li dendrites.

1.3 High Capacity Battery Electrodes

1.3.1 Si Composite Electrodes

Silicon is a promising candidate as negative electrode materials due to (1) its high gravimetric capacity (3579 mAh g^{-1}, based on $Li_{15}Si_4$) and volumetric capacity (9786 mAh cm^{-3}, based on the initial volume of Si) [10, 11]; (2) low delithiation potential (~ *ca.* 0.4 V vs. Li/Li^+); (3) low voltage hysteresis and high energy efficiency [12]; and (4) abundance in earth. The main challenge for the commercialization of Si-based electrodes is the drastic volume change (~ 300 %) during lithiation/delithiation [13, 14], which causes pulverization and fractures of Si [13-15], and continuous formation of SEI on the fractured Si surfaces [16, 17]. These mechanical and chemical degradation lead to capacity loss and low Coulombic efficiency of Si electrodes. Recently, approaches based on nanotechnology have been proposed to tackle the mechanical degradation of Si particles and thin films. Significant improvements in capacity retention and charging rate performance have been achieved with 0D (nanoparticles) [18, 19], 1D (nanowires and nanotubes) [20, 21], and 2D (thin films) [22, 23] sSi materials. Key factors contributing to the enhanced cycling performance of nanostructured Si are (1) dramatically improved damage tolerance due to high surface energy [24] and (2) rapid Li ion transport rate due to shortened Li diffusion and electron transport paths.

Composite electrodes, consisting of Si particles, polymeric binders, and conductive additives, are the most likely commercial Si electrodes for future LIBs from cost and energy density considerations. However, mechanical degradation, such as irreversible volume change, destruction of the conductive network, cracks, and the delamination, is still a major barrier to commercializing Si composite electrodes [25, 26], even these made of nanostructured Si. To improve the mechanical and microstructure integrity of composite electrodes, various strategies have been developed.

- *Polymeric binders* play a critical role in accommodating the volume change of Si particles. Preferred characteristics of effective binders for Si electrodes are suggested as

(1) inert to the electrolyte; (2) robust adhesion with Si particles and the current collector; (3) recoverable but with enough mechanical stiffness; and (4) ionically conductive [26-28]. Si composite electrodes made with the conventional polyvinylidene fluoride (PVDF) as a binder have severe polarization issues during lithiation/delithiation and suffer fast capacity degradation. By replacing PVDF with Nafion [25, 29], sodium carboxymethyl cellulose (Na-CMC) [28], and Na-alginate [30], the capacity of Si composite electrodes can be improved to be over 1500 mAh g^{-1} for 100 cycles. As shown in Chapter 2 and 3, mechanical degradation still exists in Si composite electrodes with existing state-of-the-art binders. Mechanical integrity and cycling stability of Si-based electrodes need further improvements.

- *Surface modifications* with stretchable and conformal films, such as polymeric aluminum glycerol (AlGL) [31, 32] and self-healing elastic polymer [33], can strengthen the composite matrix, reduce the irreversible volume change of composite electrodes, prevent the insulation of Si particles, and, therefore, improve the electrochemical performance of Si composite electrodes. For example, the capacity of Si/PVDF electrodes with a molecular layer deposition (MLD) coating remains 1500 mAh g^{-1} after 500 cycles [32].

1.3.2 Lithium Metal Electrodes

Due to the highest theoretical capacity (3862 mAh g^{-1}), low density (0.534 g cm^{-3}), and the lowest redox potential (-3.04 V *vs.* standard hydrogen electrode) [34, 35], Li metal is considered an ideal negative electrode for rechargeable Li-S and Li-air batteries. Different from the intercalation/deintercalation of Li into host materials, Li metal is directly plated on /stripped off the negative electrode during charging and discharging, respectively. The heterogeneous distribution of the current can cause the formation of Li dendrites during repeated plating/stripping [36, 37]. Li dendrites can penetrate through the polymer separator leading to the short circuit of cells. As the cycle number increases, bulk Li metal electrodes inevitably become porous mossy Li with a loose conductive network [34, 38]. In addition, the continuous formation of the solid electrolyte interphase (SEI) in fresh Li dendrite surfaces leads to the decomposing of the electrolyte and decreases Coulombic efficiency [34, 36]. Excessive Li dendrites and the low Coulombic efficiency during Li plating/stripping have impeded the application of Li metal electrodes since 1970s.

Various approaches have been developed to suppress Li dendrites and to improve the Coulombic efficiency of Li metal electrodes.

- *Electrolyte additives.* Electrolyte additives facilitate the formation of stable and compact SEI layers on Li surface and thus prevent the formation of Li dendrites. Effective additives include $LiNO_3$ [39] and alkali-metal ion additives (*e.g.*, Rb^+ and Cs^+ [40, 41]).
- *Micro/nanostructured frameworks for Li plating.* Increasing the surface area of the Li plating host framework will decrease the current density, uniform local current density and Li ion distribution, and delay the formation of Li dendrites [37, 42]. Micro-needle pre-treatment of Li metal [37], metal-based and carbon-based conductive nanostructured frameworks [43, 44], and non-conductive micro/nanostructured frameworks [45] have been demonstrated as effective methods to stabilize Li metal electrodes.
- *Mechanical suppression by artificial SEI and solid electrolytes.* Mechanical suppression is a promising and economic approach to inhibit Li dendrites. To prevent the penetration of Li dendrites, the elastic modulus of artificial SEI or solid electrolytes is believed to be at least twice of that of Li metal [46]. In addition, artificial SEI and solid electrolytes are expected to have high Li ion conductivity, electrochemical stability in a wide voltage window, and be interface compatible with Li metal [47-49].

1.4 Mechanical Characterization Techniques for Electrodes

At the electrode level, researchers are interested in the adhesion strength between the active layer and the current collector, the cohesion of the active layer, and the overall mechanical properties of electrodes. Mechanical characterization techniques to measure the above mechanical properties include peel tests, scratch tests, nanoindentation, and conventional tensile and compression tests.

1.4.1 Peel Tests

A good adhesion between the electrode and the current collector can promote the transfer of electrons and prevent the loss of "dead" active materials. Peel tests are one of the standard methods to study the adhesion strength between the electrode active layer and the current collector. There are different types of peel tests, such as 90° peel test, 180° peel test, and T peel test [50, 51]. The 180° peel test is commonly used for composite

electrodes due to its simple configuration geometry. To prepare samples for the 180° peel test, the current corrector is fixed to a vertical metallic plate, which is fixed to the instrument. As shown in Figure 1.3(a), a piece of tape (usually 3M Scotch tape) is firmly pressed on the surface of the electrode to ensure uniform strong adhesion between the tape and the electrode. During the peel test, the free end of the tape is pulled at a constant speed by the moveable end of the instrument at an angle of 180° regarding to the electrode surface. The force required to peel the tape is recorded by the load cell. If the electrode active layer is peeled off from the current collector, the adhesion strength can be determined by dividing the force by the peeled length (with a unit of N/cm).

The adhesion strength determined from peel tests is regarded as an important factor to optimize the electrode formulation, especially for flexible batteries [52, 53]. A positive correlation between the adhesion and the electrochemical performance has been found in graphite negative electrodes and $LiCoO_2$ (LCO) positive electrodes [52, 53].

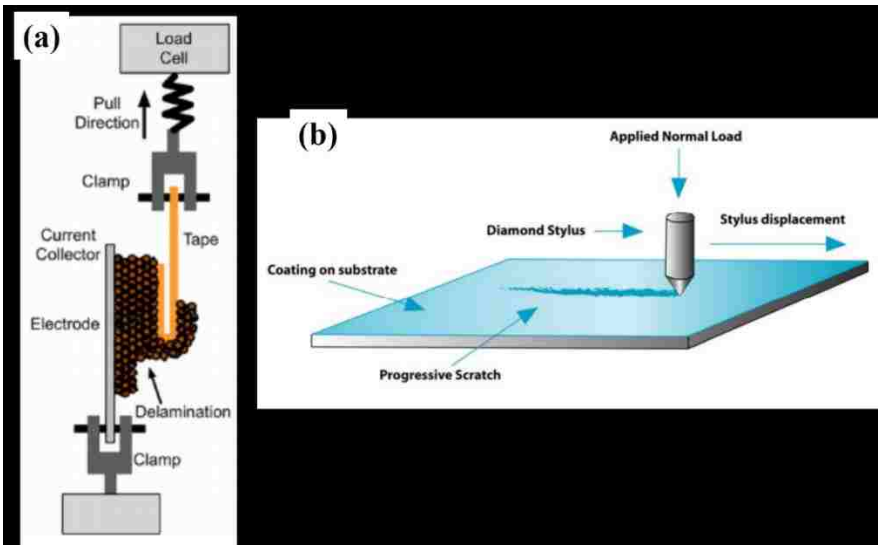

Figure 1.3. Typical schematic diagrams of (a) 180° peel tests [52] and (b) nano/micro scratch tests [54].

1.4.2 Scratch Tests

Scratch tests are an alternative method to characterize the adhesion strength between the electrode and the current collector and the cohesion of composite electrodes. Compared with peel tests, the scratch test has several advantages: (1) the dimension of

samples can be much smaller; and (2) it can reveal various failure mechanisms in coating/substrate systems and monitor the scratch damage recovery over time.

A schematic diagram of a scratch test is shown in Figure 1.3(b). During a scratch test, a tip or stylus (usually diamond conical tip) will penetrate into the coating/film with a linearly increasing normal load at a constant speed. The scratch system will record the normal force, the tangential force, and the friction coefficient. When the failure occurs in the film/substrate system, the magnitude of the friction coefficient will change abruptly. The failure points, failure mechanisms, and the critical failure load can be correlated with each other. The scratch adhesion of a coating/substrate system can be evaluated by the critical load of adhesive failures.

The application of the scratch test in electrodes is mainly to qualitatively assess whether a functional coating or film will strengthen the cohesion of the matrix and improve the adhesion strength between the electrode layer and the current collector [52, 55].

1.4.3 Nanoindentation

Nanoindentation is a powerful technique to measure mechanical properties of a wide range of materials. During nanoindentation measurements, the indenter will be forced into the sample, making an indent, and then be removed from the sample. The indentation system records the load, penetration depth, and time information during the whole test procedure. Based on the Oliver-Pharr method [56], the following mechanical properties can be determined from the load-displacement curve (Figure 1.4).

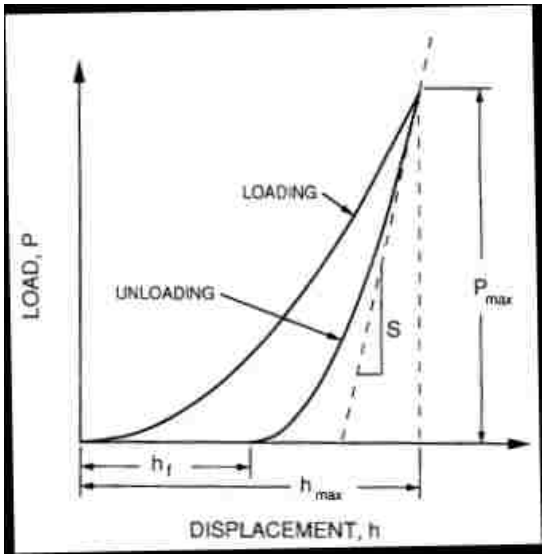

Figure 1.4. A schematic diagram of a typical load-displacement curve obtained by nanoindentation [56].

The reduced modulus is determined by,

$$E_r = S \cdot \frac{\sqrt{\pi}}{2\beta\sqrt{A}} \tag{1.1}$$

where S is the initial slope (dP/dh) of the unloading curve, β is a geometry constant ($\beta = 1.034$ for a Berkovich indenter), and A is the projected contact area of the indent.

The Young's modulus, E_s, of the sample is calculated by,

$$E_s = \frac{1-\upsilon_s^2}{\frac{1}{E_r}-\frac{1-\upsilon_i^2}{E_i}} \tag{1.2}$$

where υ_s is Poisson's ratio of the sample, υ_i and E_i are Poisson's ratio and elastic modulus of the indenter, respectively. For a diamond indenter, E_i = 1141 GPa and υ_i = 0.07.

The hardness of the sample is determined by,

$$H = \frac{P_{max}}{A} \tag{1.3}$$

where P_{max} is the maximum load.

Besides Young's modulus and hardness, other mechanical properties, such as the viscoelastic parameters [57, 58] and the strain-rate sensitivity [59], can also be investigated using different nanoindentation modes. In addition, constitutive equations for the

deformation behavior of materials can be derived by combining nanoindentation data with finite element (FE) modeling [60, 61].

Since the dimension of indents can be at nano or micro meter level, nanoindentation is a unique and increasingly popular tool to characterize mechanical behavior of various composite electrodes, including Si composite electrodes [33] and NCM composite electrodes [62, 63]. Nanoindentation results of composite electrodes depend on the ratio of the maximum indentation depth (h_{max}) to the particle size in composite electrodes. If h_{max} is more than tens of times larger than the particle size, the measured E and H are an averaged or an overall mechanical property of the composite. If h_{max} is on the same order or smaller than the particle size, the mechanical property of individual particles will dominate indentation measurements.

CHAPTER 2. ENVIRONMENTAL NANOINDENTATION: A POWERFUL TOOL FOR MEASURING MECHANICAL PROPERTIES OF SILICON COMPOSITE ELECTRODES DURING ELECTROCHEMICAL CYCLING[1]

2.1 Summary

Mechanical degradation is largely responsible for the short cycle life of silicon (Si)-based electrodes for future lithium-ion batteries. An improved fundamental understanding of the mechanical behavior of Si electrodes, which evolves, as demonstrated in this Chapter, with the state-of-charge (SOC) and the cycle number, is a prerequisite for overcoming mechanical degradation and designing high capacity and durable Si-based electrodes. In this study, Young's modulus (*E*) and hardness (*H*) of Si composite electrodes at different SOCs and after different cycle numbers are measured by nanoindentation under both dry and wet (liquid electrolyte) conditions. Unlike electrodes made of Si alone, *E* and *H* values of Si composite electrodes increase with increasing Li concentration. The composite electrodes under wet conditions are softer than that under dry conditions. Both *E* and *H* decrease with the cycle number. These findings highlight the effects of porosity, liquid environment, and degradation on the mechanical behavior of composite electrodes. The methods and results of this study on the mechanical property evolution of Si/polyvinylidene fluoride (PVDF) electrodes form a basis for exploring more effective binders for Si-based electrodes. Furthermore, the evolving nature of the mechanical behavior of composite electrodes should be taken into consideration in future modeling efforts of porous composite electrodes.

2.2 Introduction

Rechargeable lithium-ion batteries (LIBs) with high energy density are attractive choices for grid energy storage and electric vehicles (EVs). Intensive efforts have been devoted to developing electrode materials with high capacity and long cycle life. Si is considered as one of the most promising negative electrode materials not only because of its high gravimetric capacity (3579 mAh g^{-1}, based on $Li_{15}Si_4$) [10, 64], high volumetric

[1] Reproduced from *Wang, Yikai, Qinglin Zhang, Dawei Li, Jiazhi Hu, Jiagang Xu, Dingying Dang, Xingcheng Xiao, and Yang-Tse Cheng. "Mechanical property evolution of silicon composite electrodes studied by environmental nanoindentation." Advanced Energy Materials, 8, no. 10 (2018): 1702578.*

capacity (9786 mAh cm^{-3}, based on the initial volume of Si) [11], but also because of its low delithiation potential (~ca. 0.4 V vs. Li/Li^+), low voltage hysteresis [12], and thus high energy efficiency. However, the huge volume change (~300%) of Si during the lithiation/delithiation process leads to high mechanical stress, pulverization and fracture of Si particles [13, 14]. The continuous formation of the solid electrolyte interphase (SEI) on the fractured Si surfaces consumes lithium, and, consequently, leads to capacity fading [17, 65]. Although the fracture of individual Si particles can be mitigated by reducing the particle size down to 150 nm [13], the mechanical degradation of composite electrodes (the typical form for commercial LIBs), such as fracture, irreversible volume change, delamination and the breaking of the conductive network, remains a major challenge that impedes the commercialization of Si composite electrodes [25, 26, 31].

There has been an increasing number of theoretical modeling and experimental studies on the mechanical behavior, including deformation, internal stress, and fractures, of high capacity electrode materials during the lithiation/delithiation process [14, 15, 66-69]. Mechanical properties of electrodes are indispensable in developing and testing models for LIBs. First-principles calculations showed that the Young's modulus of Li_xSi compounds decreases from 95 GPa (x = 0, amorphous Si) to 38 GPa (x = 3.75, $Li_{15}Si_4$) as the Li concentration increases [70, 71], which is confirmed by *in situ* and *ex situ* nanoindentation measurements [72, 73]. However, future commercial Si electrodes for high energy applications are most likely to be composite electrodes instead of Si thin film electrodes from energy density and economic considerations. The mechanical properties of Si composite electrodes and Si film electrodes cannot be assumed the same because of the complex porous microstructure of Si composite electrodes, consisting of Si particles, polymeric binders, and conductive additives. During the lithiation/delithiation process, the porosity of Si composite electrodes changes along with the expansion/contraction of Si particles [26, 31, 74]. The rule of mixture may also be inapplicable to porous composite electrodes [75, 76].

Mechanical measurements of electrodes after electrochemical tests are challenging because, (1) some SEI components, such as LiOH and RCHOLi, are highly reactive with oxygen and water vapor [77, 78] and (2) Li_xSi compounds in the electrode are thermodynamically metastable [79] - oxidation is likely to happen after exposing

electrodes (after cycling) to the air. Therefore, sample preparation and mechanical property measurements of Si composite electrodes after electrochemical cycling must be conducted in an inert environment. On the other hand, LIBs electrodes operate under wet conditions (in liquid electrolyte, such as ethylene carbonate (EC) and diethyl carbonate (DEC) organic solvent-based electrolytes). Polymeric binders, such as polyvinylidene fluoride (PVDF), can swell and soften in the electrolyte [28, 30]. The swelling of binders may also change the porosity of composite electrodes. Thus, mechanical properties of composite electrodes under wet conditions may be significantly different from that under dry conditions. Furthermore, the phase transformation and the expansion/contraction of active particles make the mechanical behavior of composite electrodes more complex. Presently, there are only a few studies of mechanical properties of as-made composite electrodes under dry conditions [80, 81]. Fewer data are available for the mechanical properties of Si composite electrodes at different SOCs in electrolytes. The lack of mechanical property data of electrodes during lithiation/delithiation also makes theoretical electro-mechanical analyses and predications difficult.

In this study, we conducted nanoindentation measurements of Si composite electrodes under both dry and wet conditions. The environmental nanoindentation system is installed inside an argon-filled glovebox to prevent the contamination of oxygen and moisture. In our previous study, this nanoindentation system was successfully used to characterize the viscoplastic properties of Li metal [60]. A typical composite electrode made of Si particles, PVDF, and carbon black (CB) was selected because the Si/PVDF/CB composite electrode has been widely used as a baseline system for improving the performance and durability of Si composite electrodes, though mechanisms responsible for its relatively poor performance are not well-understood [25, 28, 82]. Recently, significant improvements in the electrochemical performance of Si/PVDF electrodes have been made by using an alucone coating (by molecular-layer deposition, MLD) [31, 32].

2.3 Experimental

2.3.1 Electrode Preparation

Si composite electrodes were prepared by 50 wt% silicon powder (d = 30-50 nm, Nanostructured & Amorphous Materials), 25 wt% PVDF (Alfa Aesar), and 25 wt% conductive carbon black (CB, Super C65, TIMCAL). The N-methyl-2-pyrrolidone (NMP, 99.5%, Alfa Aesar) solvent was used to dissolve PVDF. A planetary mixer (Mazerustar, KK-250S) was used to prepare uniform slurry. The slurry was casted on a battery grade Cu foil (thickness, 24 μm) with a blade (gap, 127 μm). The electrode was dried in a vacuum oven at 120℃ for 12h and calendered to a final thickness of 42 μm. Electrode discs with a diameter of 12 mm were used for electrochemical tests. The average mass loading of the as-made electrode is 0.86 ± 0.04 mg cm^{-2}.

2.3.2 Swagelok Cells

Swagelok cells, as shown in Figure 2.1(a) were used to obtain composite electrodes with different SOCs and to avoid deformation and external stress in the electrode during the cell disassembling process. The applied stress can be controlled through the deformation of the spring. In this study, the compression stress after assembling is determined to be about 0.1 MPa . As shown in Figure 2.1(b), the electrochemical performance of the Si/PVDF composite electrode in the Swagelok cell is comparable with that in the coin cell [29].

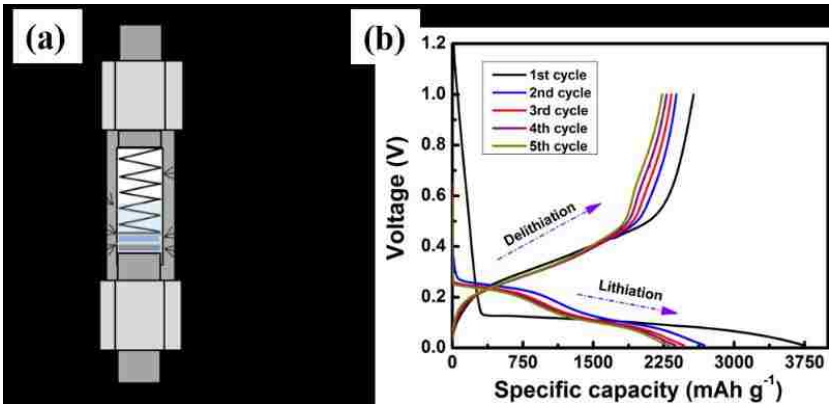

Figure 2.1. (a) The schematic diagram of the Swagelok cell and (b) the voltage-capacity profiles of the Si/PVDF composite electrode cycled with a Swagelok cell.

2.3.3 Electrochemical Tests

All Swagelok cells were assembled and cycled in an argon-filled glovebox (H_2O < 0.1 ppm, O_2 < 0.1 ppm, MBRAUN) using lithium foil (0.75mm, Alfa Aesar) as the counter electrode. Celgard 2400 separator was used in this study. The electrolyte was 1M $LiPF_6$ in a mixture solution of ethylene carbonate and diethyl carbonate (EC: DEC = 1:1 wt%, BASF) with 10 wt% fluoroethylene carbonate (FEC, BASF) additive. A galvanostatic-potentiostatic mode was used to cycle Swagelok cells by using a Bio-Logic potentiostat (VMP-3). All the electrodes were cycled at C/40 between 1.0 and 0.01 V. In the 2nd cycle, the galvanostatic mode was changed to the potentiostatic mode (with a current density limit of 1.5 μA cm^{-2}) when the charge/discharge capacity is 300 mAh g^{-1} less than the pre-determined SOCs. To prepare electrodes after long-term cycling, electrodes were cycled at C/40 for the first and the last cycles, and C/10 for the rest cycles. The potentiostatic mode (with a current density limit of 1.5 μA cm^{-2}) was used for the last cycle. Post-cycled electrodes were obtained by disassembling the Swagelok cell. The electrodes were immersed in 25 mL dimethyl carbonate (DMC, BASF) for 5 min, and then rinsed with 2mL fresh DMC with a dropper to remove the residual $LiFP_6$ and EC.

2.3.4 Microstructure Characterizations

The mass and thickness of composite electrodes before and after electrochemical cycling were measured by a balance (XS205 Dual Range Analytical Balance) and a micrometer (Mitutoyo), respectively. The microstructure of composite electrodes before and after electrochemical cycling was investigated by a field emission scanning electron microscope (SEM, FEI Quanta 250). The cross-section of indents along the median were prepared by using a focused ion beam (FIB, FEI Helios Nanolab 660). The regional porosity was analyzed using ImageJ. *Ex situ* X-ray diffraction (XRD) analyses were conducted by using Siemens D5000 (Cu Kα radiation, λ= 0.154 nm, 40 kV, 30 mA, 0.02°/step, 0.5°/min). The post-cycled electrodes were sealed with Kapton tapes (KPTLS-1, *www. Kaptontape.com*) in the glovebox to insulate the sample from the air. This Kapton tape has been used for *in situ* XRD cells due to its reliable leak-proof [83].

2.3.5 Environmental Nanoindentation

As shown in Figure 2.2, the environmental nanoindentation system consists of a Nanoindenter G200 (Agilent) inside an argon-filled glovebox and a cell made of J-B weld epoxy glue, which enables us to conduct nanoindentation measurements in the liquid electrolyte. We confirmed the reliability of the liquid cell by comparing the indentation results of a stainless steel disc (mounted with the same epoxy glue) under dry and wet conditions. As shown in Figure 2.3, the load-displacement (L-D) curves under wet conditions match well with that under dry conditions. Reproducible and consistent indentation results were obtained for the stainless steel under dry and wet conditions, as shown in Table 2.1.

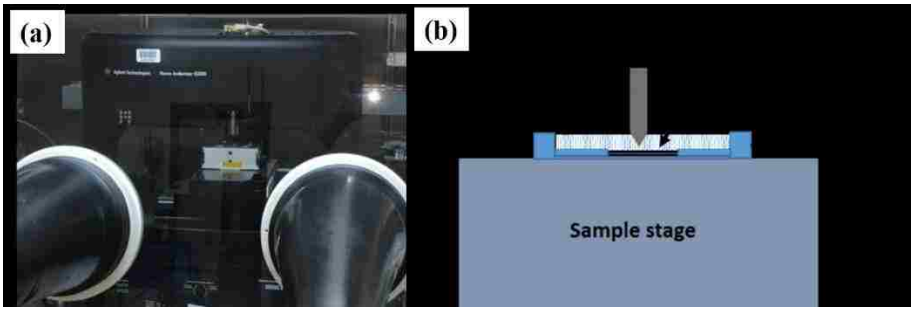

Figure 2.2. (a) The G200 nanoindentation system inside an argon-filled glovebox and (b) the schematic of the liquid cell used for indentation measurements under wet conditions.

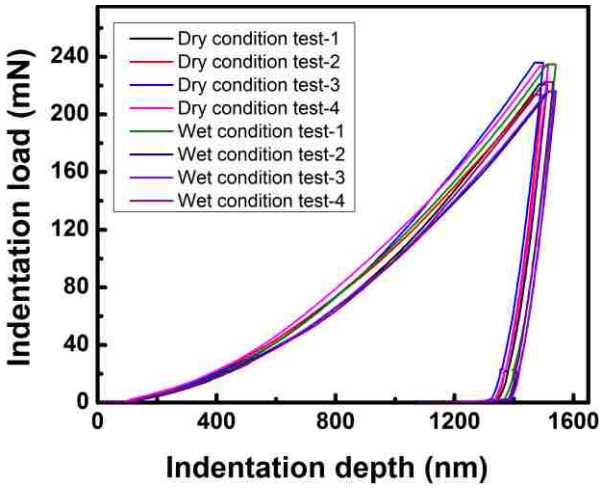

Figure 2.3. Nanoindentation L-D curves of the stainless steel mounted by J-B weld glue measured under dry and wet conditions.

Table 2.1. Nanoindentation results of the stainless steel measured under dry and wet conditions.

Test #	Dry condition		Wet condition	
	E/GPa	H/GPa	E/GPa	H/GPa
1	240.95	3.16	254.88	3.08
2	253.57	3.09	250.46	3.43
3	262.10	3.42	238.82	4.03
4	235.00	3.35	241.38	3.24
5	264.36	3.82	243.68	2.95
6	259.23	3.54	262.00	3.53
Average value	252.54	3.40	248.54	3.38
Standard deviation	10.95	0.24	8.11	0.35

A depth-controlled mode was adopted with an indentation strain rate of 0.05 s^{-1} and the maximum depth of 1500 nm. The indenter was held for 10 seconds at the maximum load. Thermal drift calibration (100 seconds) were conducted after unloading. The substrate effect can be neglected since the maximum depth is less than 1/10 of the thickness of the electrode. The elastic modulus and hardness were determined based on the Oliver-Pharr's method [56]. Environmental nanoindentation tests under wet conditions were carried out with the liquid cell. The electrolyte was changed every 40 min to avoid the influence of precipitated EC and $LiPF_6$ (due to the evaporation of DEC) on nanoindentation measurements. The weight reduction rate of the electrolyte is 4.19 ± 0.65% /cm^2 in the glovebox during the 40 min. This minor composition change will not influence the nanoindentation measurements under wet conditions. During the test, the indenter was immersed into the electrolyte. Therefore, the surface tension of the electrolyte will not influence the nanoindentation result. 100 and 50 nanoindentation tests were conducted in each sample under dry and wet conditions, respectively. Indentation results were analyzed by Gaussian function,

$$f(x) = f_0 + Ae^{-\frac{(x-\mu)^2}{2\sigma^2}} \quad \text{Eq. (2.1)}$$

where μ is the expectation at the center position of the bell curve, σ is the standard deviation, and σ^2 is the variance.

2.3.6 Porosity Measurements of the Electrodes

The porosity of composite electrodes was determined by,

$$\text{Porosity}(\%) = (1 - \frac{\rho_{measured}}{\rho_{theoretical}}) \times 100 \quad \text{Eq. (2.2)}$$

where $\rho_{measured}$ is the measured density of the electrodes,

$$\rho_{measured} = \frac{m_{electrode} - m_{Cu}}{tA} \quad \text{Eq. (2.3)}$$

where *t* is the thickness of the active layer in the electrode and *A* is the area of the electrode disc. $\rho_{theoretical}$ is the theoretical density of the electrodes with a porosity of zero.

$$\rho_{theoretical} = \frac{1}{\frac{w_{LixSi}}{\rho_{LixSi}} + \frac{0.5(1-w_{LixSi})}{\rho_{PVDF}} + \frac{0.5(1-w_{LixSi})}{\rho_{CB}}} \quad \text{Eq. (2.4)}$$

where w_{LixSi} is the weight ratio of Li_xSi of the electrode. It is 50% for the as-made electrode. At certain SOCs, w_{LixSi} is determined based on the mass of Si in the electrode,

$$w_{LixSi} = \frac{\frac{m_{Si}}{M_{Si}} \times (M_{Si} + xM_{Li})}{\frac{m_{Si}}{M_{Si}} \times (M_{Si} + xM_{Li}) + m_{PVDF} + m_{CB}} \quad \text{Eq. (2.5)}$$

where M_{Si} and M_{Li} are the atomic mass of Si and Li, respectively. *x* could be determined by,

$$x = \frac{Q_{discharge}}{3579} * 3.75 \ \ (\text{during lithiation}) \quad \text{Eq. (2.6)}$$

$$x = \frac{(3579 - Q_{charge} + 697)}{3579} * 3.75 \ \ (\text{during delithiation}) \quad \text{Eq. (2.7)}$$

where $Q_{discharge}$ is the discharge capacity corresponding to SOCs during the lithiation process, Q_{charge} is the charge capacity corresponding to SOCs during the delithiation process. The average capacity difference between the fully delithiated state and 3579 mAh g^{-1} (theoretical capacity) of four Swagelok cells is 697 ± 73 mAh g^{-1}. Therefore, *x* of electrodes at SOCs in the delithiation process is normalized by 697 mAh g^{-1} in Eq. (2.7). We assume $x = 0$ and $x = 3.75$ for electrodes after full delithiation and lithiation, respectively. The densities of Li_xSi components used for the above calculations are from Kim's work [70].

2.4 Results and Discussion

The Si composite electrodes were electrochemically lithiated/delithiated to various SOCs. Then, nanoindentation measurements were carried out in those electrodes under dry and wet conditions.

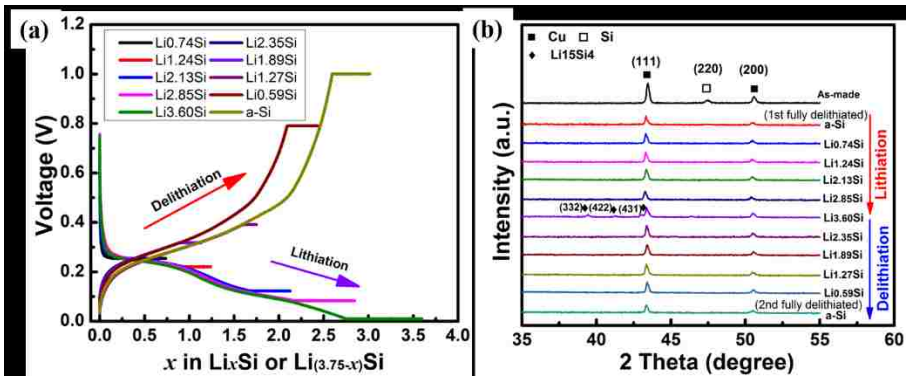

Figure 2.4. (a) Voltage-SOC profiles of Si/PVDF electrodes during the 2nd cycle and (b) XRD patterns of composite electrodes with different SOCs.

Due to the phase transformation from crystalline Si to amorphous Li_xSi and the formation of a large amount of SEI in the 1st cycle, electrodes with different SOCs were obtained in the 2nd cycle, as shown in Figure 2.4(a). The X-ray diffraction (XRD) patterns of composite electrodes are shown in Figure 2.4(b). The Si (220) peak is clearly observed in the as-made electrode since crystalline Si particles are used to make the electrode. After the 1st cycle, the Si peaks disappear as the crystalline Si transforms to amorphous Li_xSi [84-86]. There is no peak of Li_xSi compounds in the XRD patterns of electrodes at other SOCs, except that three peaks of $Li_{15}Si_4$ are found in the fully lithiated electrode. These findings confirm the phase transformation of Si during the lithiation/delithiation process reported in the literature: crystalline Si starts to transform to amorphous Li_xSi compounds upon lithiation, and amorphous Li_xSi transforms to crystalline $Li_{15}Si_4$ when the potential is below a critical value (ranging from 70 mV to 30 mV, depending on the size and the morphology of Si) [84-86]. During delithiation, $Li_{15}Si_4$ gradually transforms to amorphous Li_xSi compounds and amorphous Si remains after Li is completely extracted from Li_xSi.

Depth-controlled nanoindentation measurements were conducted to obtain E and H of electrodes at different SOCs. The indentation depth was set at 1500 nm to reduce the

influence of the surface roughness and tiny cracks. Effects of the substrate on nanoindentation are negligible because the maximum indentation depth is less than 1/10 the thickness of the electrode. Since the indentation depth is much larger than the diameter of Si particles ($d = 30$ to 50 nm) in the electrode, the mechanical properties determined from nanoindentation tests are the overall or average mechanical properties of the composite electrode.

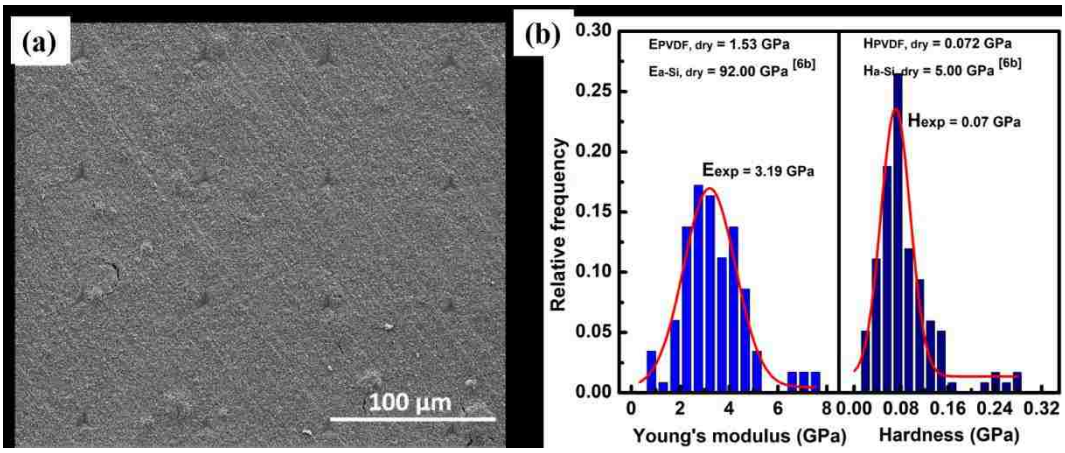

Figure 2.5. (a) A typical indentation array in the Si/PVDF electrode at the 1st full delithiation sate and (b) the distribution histograms of Young's modulus and hardness of the Si/PVDF electrode after the 1st full delithiation under dry conditions.

A typical indentation array under dry conditions is shown in Figure 2.5(a). Due to the random nature of the porous composite electrodes, the measured *E* and *H* values at each SOC have a distribution. For example, *E* and *H* of the 1st fully delithiated electrodes range from 0.59 to 7.76 GPa and from 0.01 to 0.29 GPa, respectively, as shown in Figure 2.5(b). A similar situation has also been found in the mechanical characterizations of SEI by atomic force microscope (AFM) and porous ceramics by nanoindentation [87-89]. Here, we use Gaussian function to describe the distribution of *E* and *H*. The expectation values of Gaussian function are plotted against the Li concentration (x in Li_xSi) in Figure 2.6 (a) and (b). Under both dry and wet conditions, both *E* and *H* change with the Li concentration as a hysteresis loop, that is, *E* and *H* increase with increasing Li concentration in the lithiation process, reach the peak value at the fully lithiated state, and then decrease with decreasing Li concentration in the delithiation process. This trend is opposite to that of lithiated Si films, that is, *E* and *H* decrease as the Li concentration increases [70-73].

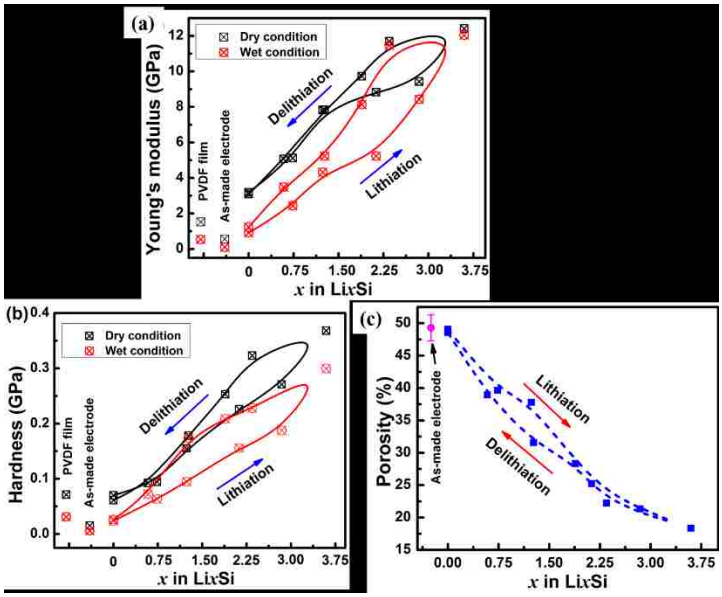

Figure 2.6. The change of (a) Young's modulus and (b) hardness of the Si/PVDF composite electrode with Li concentration (x in Li_xSi) during the 2nd lithiation/delithiation process. Since the expectation values of E and H under both dry and wet conditions were plotted against x, there is no error bar in (a) and (b). (c) The change of the porosity of composite electrodes with Li concentration (x in Li_xSi) under dry conditions. The influence of SEI on the porosity is neglected here.

Different from the compact structure of Si films, the composite electrode has a complex porous structure composed of Si particles, PVDF and CB. The porosity of the electrode can be determined based on the relationship between density, mass, thickness and area of the electrode (Eq. (2.2)-(2.7)). The porosity of the as-made electrode and the 1st fully delithiated electrode are as high as $49 \pm 2.3\%$ under dry conditions. During lithiation, the expansion of active particles will effectively reduce the porosity of the electrode, which is a densification process. The porosity gradually decreases to 18% during the 2nd lithiation and gradually increases, along a hysteresis loop, to 49% (close to that after the 1st full delithiation), as shown in Figure 2.6(c), during delithiation due to the contraction of active particles. This trend matches with the cross-sectional microstructure of electrodes in different SOCs. As shown in Figure 2.7(a), (b) and (d), many voids are visible in the as-made and fully delithiated electrodes; while smaller and fewer voids can be found in the fully lithiated electrode (Figure 2.7(c)). Because of these voids in all SOCs, nanoindentation would densify the porous composite electrode. As indicated by the dashed

lines in Figure 2.7 (b)-(d), there is a porosity gradient underneath the indents – the porosity increases with increasing distance from the apex of the indenter.

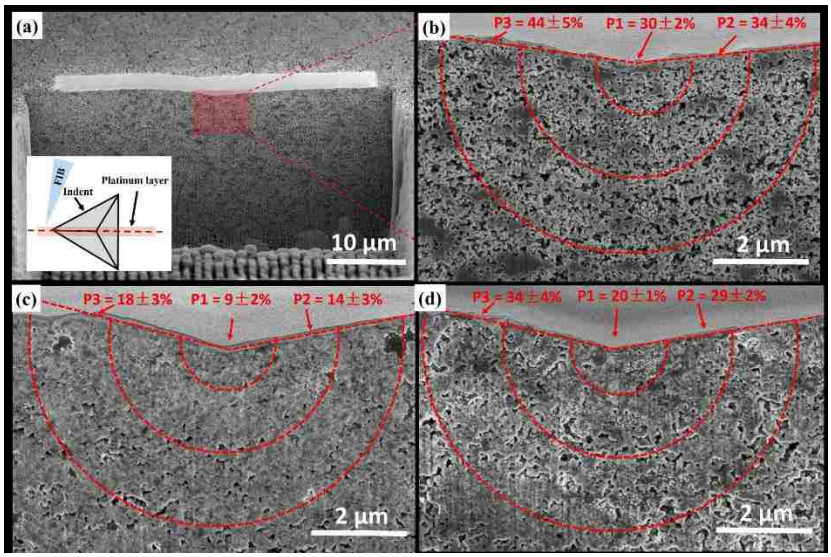

Figure 2.7 (a) A typical cross-sectional SEM image of an indent in the as-made electrode. The cross section was prepared by a focused ion beam (FIB) along the median of each triangular indent, as shown in the inserted schematic diagram. High magnification cross-sectional SEM images of (b) the as-made electrode; (c) the electrode after the 2nd full lithiation and (d) the electrode after the 2nd full delithiation. The regional porosity (analyzed by ImageJ, P1, P2 and P3) underneath the indent increases with increasing distance from the apex of the indent.

Figure 2.8(a) and (e) show that most Si particles in the electrode remain undeformed after nanoindentation. Many Si particles in the electrodes after the 1st and 2nd full delithiation are also undeformed by indentation, as shown in Figure 2.8(b), (d), (f) and (h). Therefore, the PVDF scaffold, instead of active particles, dominates the indentation-induced deformation in the highly porous composite electrodes, as shown in Figure 2.8(i) and (j). Si particles may rotate, move, and rearrange to accommodate the indentation-induced deformation. As shown in Figure 2.6(a) and (b), the *E* and *H* values of the PVDF film measured by nanoindentation (under dry conditions) are 1.53 GPa and 0.072 GPa, respectively. Both are much smaller than that of crystalline Si [70], amorphous Si, and Li_xSi compounds [70-72]. Since the PVDF framework has even smaller *E* and *H* considering of its highly porous structure, the *E* and *H* values of the as-made and fully

delithiated electrodes are expected to be much smaller than that of crystalline and amorphous Si.

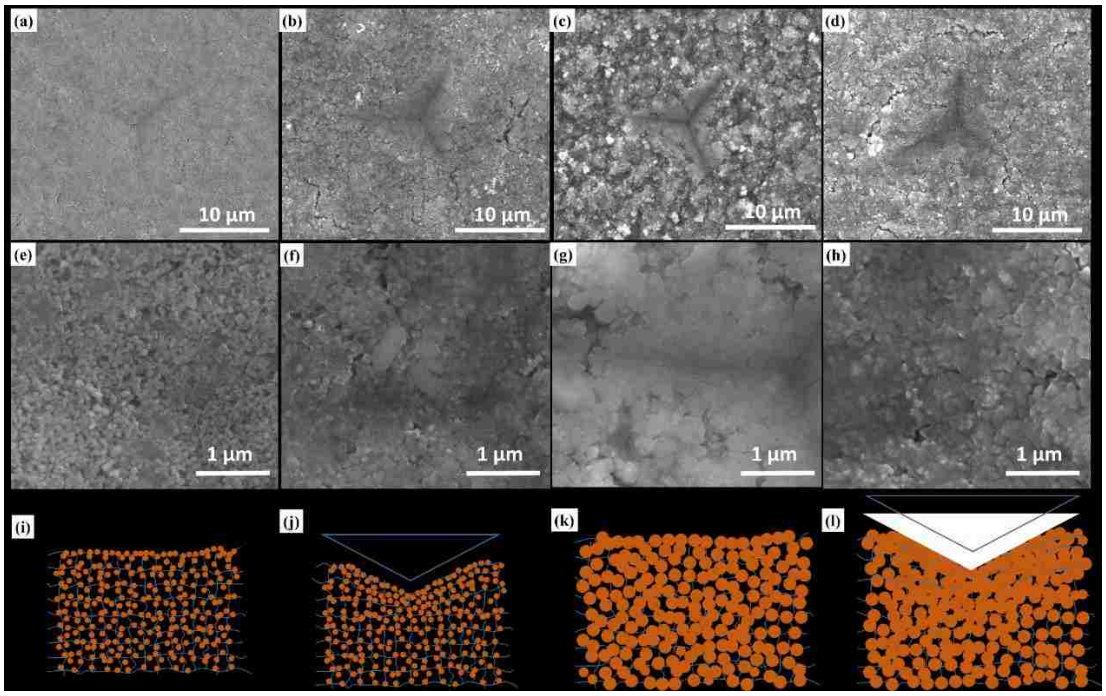

Figure 2.8. Typical indent morphologies in (a) the as-made electrode; and composite electrodes after (b) the 1st delithiation; (c) the 2nd lithiation and (d) the 2nd delithiation. (e)-(h) are enlarged microstructure in indents corresponding to (a)-(d), respectively. At the fully delithiated state, nanoindentation induces the densification of the porous structure, and the Si particles underneath the indenter remain undeformed. In fully lithiated composite electrodes with low porosity, active particles deform after localized densification under the indenter is accomplished. (i) and (j) are schematic diagrams of the indentation deformation of highly porous electrodes at the fully delithiated state. (k) and (l) are schematic diagrams of the indentation deformation of electrodes with low porosity at the lithiation state.

During the lithiation process, active particles (Li_xSi) soften and the porosity of composite electrodes decreases, as shown in Figure 2.6(c). The deformation of active particles contribute gradually to the indentation-induced deformation as the local densification under the indenter continues in the composite electrode. In particular, the local porosity right underneath the indent in the fully lithiated electrode is only $9\pm2\%$ (Figure 2.7(c)). Most active particles underneath the indenter are severely deformed, as shown in Figure 2.8(c) and (g). In the fully lithiated state, the mechanical behavior of active particles plays an important role in the nanoindentation responses of composite electrodes.

The coupling effect of the reduced porosity, the softening of active particles, and the increasing deformation ratio of active particles to the PVDF scaffold results in increasing E and H values of the composite electrode during lithiation. Due to the same coupling effect, the composite electrode softens (with smaller E and H) during the delithiation process despite the increasing modulus of the active particles [72]. After the 2nd full delithiation, E and H decrease to 1.24 GPa and 0.026 GPa under wet conditions, respectively, both of which are close to that of the 1st fully delithiated electrode. The expansion/contraction of the active particles leads to a periodic porosity change of composite electrodes during the repeated lithiation/delithiation cycling, as shown in Figure 2.6(c). Consequently, the mechanical property evolution of the composite electrode in subsequent cycles is likely to follow the same trend as the 2nd cycle, that is, both E and H increase with increasing Li concentration.

Figure 2.6(a) and (b) show that E and H values under wet conditions are always smaller than that under dry conditions, which can be attributed to the softening of PVDF in the electrolyte [28, 30]. E and H of the PVDF film under wet conditions are 35.7% and 43.4% of that under dry conditions, respectively, as shown in Figure 2.6(a) and (b). The difference in E between dry and wet conditions decreases with x in both lithiation and delithiation processes. At the 2nd fully lithiated state, the difference in E is negligible, even though the difference in H is larger than that under other SOCs. Since mechanical property measurements under dry conditions may overestimate E and H [81], cautions should be taken when using mechanical data obtained under dry conditions for electro-mechanical models of composite electrodes.

As discussed previously, nanoindentation measurements reflect the overall mechanical response of composite electrodes, including the influence of SEI. SEI may strengthen the porous structure of composite electrodes, since both E and H of the electrodes after the 1st and 2nd full delithiation are larger than the as-made electrode in spite of similar porosity. The mechanical properties and the components of SEI depend on the charging/discharging potential in the 1st lithiation of Si [89, 90]. Yet, the interaction between SEI and binders and the adhesion between SEI and active particles are unknown.

It is, therefore, difficult to separate and quantify the effect of SEI on the mechanical properties of composite electrodes.

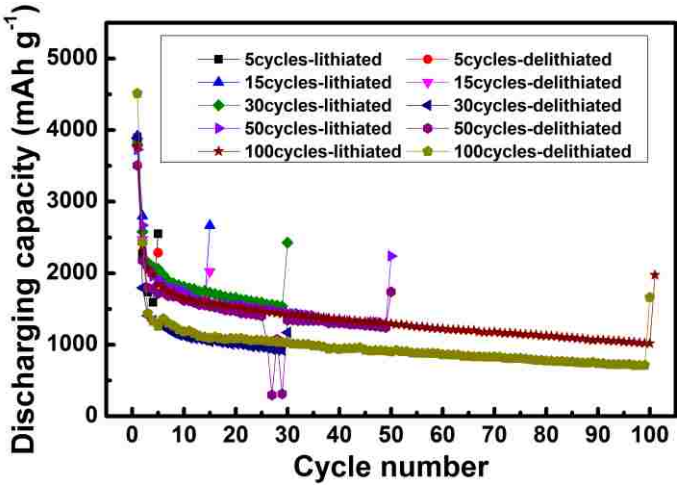

Figure 2.9. Electrochemical performance of Si/PVDF electrodes. The high discharging capacity in the last cycle is due to the low C-rate (C/40) and the potentiostatic holding at the cutoff voltage. The discharging capacity degrades slowly compared with reference [29] since the electrodes were cycled at a lower C-rate (C/10) and the electrolyte amount was abundant.

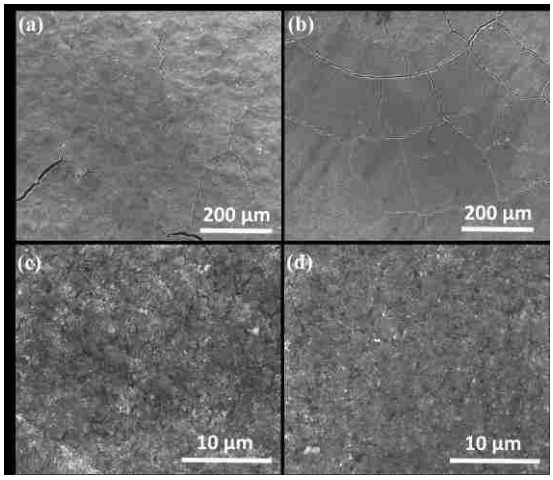

Figure 2.10. The surface morphology of Si/PVDF electrodes at (a) and (c) the full lithiation state, (b) and (d) the full delithiation state after 100 cycles.

In order to determine how mechanical properties would change during long-term cycling, we measured *E* and *H* of composite electrodes at the full lithiation and delithiation states up to 100 cycles (Figure 2.9) under dry and wet conditions. The surfaces of the electrodes are still smooth enough for nanoindentation measurements even after 100 cycles

(Figure 2.10). As shown in Figure 2.11(a) and (b), *E* and *H* at the fully lithiated state are always larger than that at the fully delithiated state, which, again, results from the coupling effect of mechanical properties of Li_xSi, the porosity change and the deformation mechanisms of electrodes. Again, *E* and *H* under wet conditions are smaller than that under dry conditions due to the softening of PVDF in the electrolyte. *E* and *H* values are stable within 15 cycles. After 15 cycles, *E* and *H* under both dry and wet conditions decrease as the cycle number increases. To the best of our knowledge, this is the first experimental observation of the mechanical property degradation of composite electrodes during electrochemical cycling.

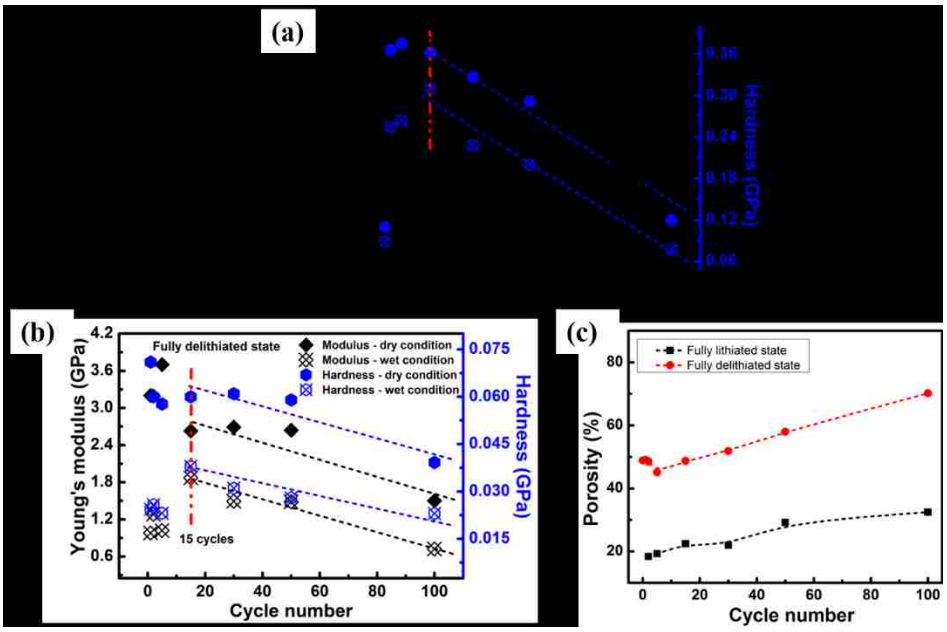

Figure 2.11. The evolution of Young's modulus and hardness of the composite electrodes as the cycle number increases: (a) at the fully lithiated state and (b) at the fully delithiated state. Since the expectation values of *E* and *H* under both dry and wet conditions were plotted against *x*, there is no error bar in (a) and (b). (c) The change of the porosity (under dry conditions) with the cycle number.

The mechanical property degradation of composite electrodes is likely caused by the irreversible volume change of the electrode. The potentiostatic mode of cycling was not used for each lithiation/delithiation process during the long-term cycling. Due to polarization, some Li atoms are still left in the Si particles at the cutoff voltage of delithiation. There is residual expansion of the Si particles after each cycle. Thus, the electrode gradually thickens during electrochemical cycles and cannot recover even after

full delithiation. The increasing irreversible volume change of the composite electrode is associated with increasing porosity as shown in Figure 2.11(c). After 100 cycles, the porosity reaches 70% and 32% at the fully delithiated and lithiated states, respectively. The increasingly high porosity has a negative influence on the mechanical integrity and the load-bearing capability of the composite electrode. Consequently, both E and H at the lithiation and delithiation states decrease as the cycle number increases (after 15 cycles).

The increasing irreversible volume change of the composite electrode not only affects its mechanical integrity, but also breaks down the conductive network, leading to particle isolation and hence capacity fading. It is essential to develop mechanically robust Si composite electrodes for future LIBs. Three main approaches have been proposed for this purpose in the literature: 1) using stiff but recoverable polymeric binders, such as sodium alginate [25, 30], to enhance the mechanical integrity and reduce the irreversible volumetric change of composite electrodes; 2) coating active particles with compliant materials, including Al_2O_3, HfO_2, and LiF, to accommodate the continuous expansion/shrinkage of Si particles [65, 91, 92]; 3) modifying the surface of composite electrodes with stretchable, conformal films, such as polymeric aluminum glycerol (AlGL) or self-healing elastic polymers [31, 33, 82], to maintain mechanical integrity and electronic conductivity. The environmental nanoindentation approach developed in this Chapter can be used to evaluate these proposed approaches.

The Si particle size (d) can affect nanoindentation measurements. If the indentation depth is too small compared to the Si particle size, *e.g.*, $d/h_{max} > 50$, indentation results will be dominated by the mechanical properties of individual Si or Li_xSi particles. In this case, the modulus, E, values are expected to decrease with increasing lithium concentration according to density-functional theory calculations and *ex situ* nanoindentation results [70-72]. In order to measure the average or the overall mechanical property of the composite electrode, nanoindentation measurements should be conducted with a large maximum indentation depth, *e.g.*, $h_{max}/d > 30$, as in this study.

The porosity can strongly affect the mechanical property of the composite electrode. The porosity of the composite electrode was found to decrease from $65 \pm 5\%$ to $49 \pm 3\%$ after calendering. The porosity of electrodes without calendering also decreased

with increasing Li concentration. As a result, *E* and *H* values increase with increasing Li concentration. At each SOC, the calendered electrodes have larger *E* and *H* values than the un-calendered electrodes because the calendered electrodes have lower porosity. If the porosity of the electrode after calendering is very low (< 20%), the porosity could be reduced to near zero after full lithiation. Thus, *E* and *H* of the electrodes are likely to first increase (because of the reduced porosity) and then decrease (due to the softening of Li_xSi with increasing *x*) with increasing lithium concentration. The relationship between active particle size, initial porosity, mechanical properties, and the electrochemical performance of composite electrodes will be further investigated in the future.

2.5 Conclusions

Young's modulus and hardness of Si/PVDF composite electrodes at various SOCs and after different cycle numbers have been measured by environmental nanoindentation in an argon-filled glove box under both dry and wet conditions. In contrast to Si films, *E* and *H* values of Si composite electrodes, under both dry and wet conditions, increase with increasing Li concentration due to mainly porosity changes. The values of *E*, *H*, and the porosity change with the Li concentration along a hysteresis loop within a cycle. Both *E* and *H* under wet conditions are smaller than that under dry conditions as the binder, *i.e.* PVDF in this study, softens in the organic electrolyte. *E* and *H* at the fully lithiated and delithiated states decrease as the cycle number increases. The mechanical property degradation results from the increasing irreversible volume change of the composite electrode during cycling. The results show that mechanical integrity is essential to improve the electrochemical performance of composite electrodes. The measured *E* and *H* of composite electrodes at different SOCs and after cycling under wet conditions are useful input parameters for electro-mechanical models and pave the way for developing durable Si electrodes for the next generation LIBs. The environmental nanoindentation method developed in this study can be readily extended to the investigation of Si-composite electrodes using various polymeric binders, including better performing ones such as Na-carboxymethylcellulose (Na-CMC) and Na-alginate. Furthermore, the environmental nanoindentation method can be applied to the mechanical characterization of a wide range

of electrochemical energy storage materials, including but not limited to lithium-ion battery applications.

CHAPTER 3. INFLUENCE OF POLYMERIC BINDERS ON MECHANICAL PROPERTIES AND MICROSTRUCTURE EVOLUTION OF SILICON COMPOSITE ELECTRODES DURING ELECTROCHEMICAL CYCLING[2]

3.1 Summary

Polymeric binders are a critical component to enhance mechanical integrity, maintain electronic conductivity, and achieve long durability of silicon (Si)-based electrodes. A fundamental understanding of the relationship between binder properties and mechanical degradation of Si electrodes is indispensable to developing durable Si-based electrodes. Using an environmental nanoindentation system, we measured the mechanical properties of Si composite electrodes made with different binders, including polyvinylidene fluoride (PVDF), Nafion, sodium-carboxymethyl cellulose (Na-CMC), and sodium-alginate (SA), as a function of the state-of-charge and cycle numbers under both dry and wet conditions. In contrast to electrodes made of Si alone, both the elastic modulus (*E*) and hardness (*H*) of Si composite electrodes increase with lithium concentration within each cycle. *E* and *H* continuously decrease during long-term cycling. The mechanical property evolution of Si composite electrodes can be correlated with the porosity and irreversible thickness changes, which are largely determined by the mechanical properties of binders, instead of the adhesion strength between binders and Si. Electrodes under wet conditions have smaller *E* and *H* values than those under dry conditions because binders soften in the electrolyte. These findings not only provide useful mechanical parameters for battery modeling, but also may help design high performance and durable Si-based electrodes.

3.2 Introduction

Silicon (Si) has been considered one of the most promising negative electrode materials for the next generation high energy density lithium ion batteries (LIBs) because it can deliver a high theoretical specific capacity of 3579 mAh g^{-1} [12, 93, 94]. However, electromechanical degradation resulting from the substantial volume change (≈300 %) of

[2] Reproduced from *Wang, Yikai, Dang, Dingying, Dawei Li, Jiazhi Hu, and Yang-Tse Cheng. " Influence of Polymeric Binders on Mechanical Properties and Microstructure Evolution of Silicon Composite Electrodes during Electrochemical Cycling." Journal of Power Sources, 425 (2019): 170-178.*

Si during repeated lithiation/delithiation remains an obstacle to commercializing Si-based electrodes. Specifically, the repeated huge volume change of Si causes severe cracking and pulverization of Si particles and mechanical disintegration of electrodes [26, 95, 96]. Solid electrolyte interphase (SEI) continuously forms on the newly exposed surface of Si, consuming electrolytes and lithium ions, insulating Si particles, and leading to low Coulombic efficiency and fast capacity fading of Si electrodes [13, 25, 90]. Extensive efforts have been devoted to overcoming these challenges and improving the performance of Si-based electrodes, including nanostructured Si (*e.g.*, Si nanoparticles [13, 97] and Si nanowires [14, 98]), innovative coating technologies (*e.g.*, atomic layer deposition [65, 99] and molecular layer deposition [31, 32, 82]), and Si/graphite composite electrodes [100, 101].

Alternatively, using effective polymeric binders has been recognized as a facile, economical, and scalable method to significantly improve the electrochemical performance of Si composite electrodes [27, 30, 102], which consist of Si particles, carbon black (CB), binders, and pores. Binders are used to bind Si particles and CB together and adhere them to the current collector. Polyvinylidene fluoride (PVDF), the commonly used binder in the LIBs industry, is ineffective in maintaining the mechanical integrity of Si composite electrodes due to its weak van der Waals interaction with Si [28, 103, 104]. Instead, a wide range of natural polymeric binders, including sodium carboxymethyl cellulose (Na-CMC) [84, 105], sodium alginate (SA) [25, 30], poly(acrylic acid) (PAA) [28, 106, 107], and karaya gum (KG) [108], and synthetic binders, including Nafion [25, 29] and polyrotaxane-PAA [27], can form strong hydrogen and covalent bonds with the native SiO_2 layer on Si particles with their polar functional groups, such as –OH, –COO-R, and -SO_2O-R (R can be H, Na, or Li), maintain the microstructure integrity and electronic conductivity of the porous network, and, therefore, improve stability and durability of Si composite electrodes. Nevertheless, Si composite electrodes made of the state-of-the-art binders still inevitably experience irreversible volume change, cracking, and delamination during cycling [26, 95, 109]. But the relationship between binder properties and electromechanical degradation of Si composite electrodes is still unclear.

Furthermore, the mechanical properties of electrodes during cycling in realistic organic electrolyte environment are lacking for intensive experimental and theoretical

modeling efforts in understanding and overcoming electromechanical degradation of Si composite electrodes [110, 111]. Different from Si thin films and single crystal Si wafer electrodes [70-73], Si composite electrodes have porous microstructure. During electrochemical cycling, the phase transformation between Si and Li_xSi causes the expansion/contraction of Si particles and porosity changes. The formation of SEI may influence the adhesion between Si (or Li_xSi) particles and polymeric binders. Polymeric binders may also swell and soften in the organic electrolyte [28, 30]. These factors make mechanical properties and microstructure changes of Si composite electrodes very complex and theoretically unpredictable. Moreover, mechanical property measurements of Si composite electrodes are challenging because SEI components (such as LiOH), Li_xSi compounds, and electrolytes are sensitive to air and moisture [78, 79, 112]. We have recently developed an environmental nanoindentation system inside an argon-filled glovebox to overcome the challenges for mechanical property measurements of Si composite electrodes in the liquid electrolyte environment [113]. Our previous study showed that the elastic modulus (E) and hardness (H) of the Si/PVDF/CB composite electrodes increase with increasing lithium concentration although Li_xSi softens with increasing lithium concentration [78, 79, 112]. Since binders have different mechanical properties [25, 28, 30], adhesion strength with Si [103, 104], and swelling/softening behavior in the electrolyte [28, 30], it is necessary to investigate (1) whether a general trend in mechanical behavior exists in Si composite electrodes made of different binders and (2) the influence of binder properties on mechanical properties and microstructure changes of Si composite electrodes.

In this study, we selected four typical binders, polyvinylidene fluoride (PVDF), Nafion, sodium-carboxymethyl cellulose (Na-CMC), and sodium-alginate (SA), to study the influence of binders on the mechanical properties of Si composite electrodes at different states of charge (SOCs) and after different numbers of cycles under both dry and wet conditions using our environmental nanoindentation system. Porosity and irreversible thickness changes[3] during cycling were measured and compared by postmortem analysis. Mechanical properties of binders and the adhesion between binders and Si were correlated

[3] The irreversible thickness change is the thickness difference between the n-th delithiated electrode and the as-made electrode (after calendering).

with the mechanical property evolution and microstructure degradation of Si composite electrodes.

3.3 Experimental

3.3.1 Electrode Preparation

Si composite electrodes were prepared by 50 wt% Si powder (d = 30-50 nm, Nanostructured & Amorphous Materials), 25 wt% carbon black (CB, Super C65, TIMCAL), and 25 wt% binders, including PVDF (Alfa Aesar), Nafion dispersion liquid (D-520, Alfa Aesar), Na-CMC (Alfa Aesar), and SA (Sigma-Aldrich). Deionized water was used to dilute Nafion dispersion solution and dissolve Na-CMC and SA. PVDF was dissolved in N-methyl-2-pyrrolidone (NMP, 99.5 wt%, Alfa Asear). A planetary mixer (Mazerustar, KK-250S) was used to prepare uniform slurry, which was then casted on a battery grade Cu foil (thickness, 24 μm) using a doctor blade with a gap of 127 μm. After drying at room temperature for 12 h, the electrodes were dried in a vacuum oven at 100 ℃ for 12 h. Then, the electrodes were calendered multiple times until the porosity reaches 50±5 % using a rolling machine (MSK-HRP-MR100, MIT Co., Ltd.). The porosity (p) of the as-made electrodes was calculated based on Eq. (2.2) and (2.3). The densities of carbon black, binders, and Si are list in Table 3.1. The average thickness and mass loading of all electrodes are 41-43 μm and 0.85-0.95 mg cm^{-2}, respectively. Electrode discs with a diameter of 12 mm were used for electrochemical tests.

Table 3.1 Densities of Si, carbon black, and binders.

Materials	Density / g cm^{-3}
Silicon	2.33
Carbon black	1.60
PVDF	1.76
Na-CMC	1.59
Na-alginate (SA)	1.60
Nafion	1.97

3.3.2 Electrochemical Measurements

Swagelok cells were used for electrochemical tests to avoid introducing deformation and external stress in the cycled electrodes during the disassembling process [113]. All cells were assembled and cycled in an argon-filled glovebox (H_2O < 0.1 ppm,

O_2 < 0.1 ppm, MBRAUN) using lithium foil (0.75mm, Alfa Aesar) as the counter and reference electrodes and Celgard 2400 separator. The electrolyte was 1M $LiPF_6$ in a mixture solution of ethylene carbonate and diethyl carbonate (EC: DEC = 1:1 wt%, Gotion) with 10 wt% fluoroethylene carbonate (FEC, Gotion) as the additive. 500 µL electrolyte was used in each Swagelok cell. A galvanostatic-potentiostatic mode was used to cycle Swagelok cells with a Bio-Logic potentiostat (VMP-3). Si/Na-CMC, Si/SA, and Si/Nafion electrodes were cycled at C/20 between 1.00 and 0.01 V. Electrodes at different SOCs were obtained by changing the galvanostatic mode to the potentiostatic mode (with a current density limit of C/400 µA cm^{-2}) when the charge/discharge capacity is 300 mAh g^{-1} less than the pre-determined SOCs in the 2nd cycle. Figure 3.1(a) shows the voltage *vs*. lithium concentration (*x* in Li_xSi) profiles of Si/Na-CMC electrodes at different SOCs (we converted the lithiation/delithiation capacity to *x* in Li_xSi [113]). For long-term cycling, the electrodes were cycled at C/20 for the first 2 cycles and a galvanostatic-potentiostatic mode (with a current density limit of C/400 cm^{-2}) was used for the last lithiation/delithiation cycle. The cycling protocol of Si/PVDF electrodes can be found in our previous study [113]. The lithium concentration, *x* in Li_xSi, at different SOCs is determined based on the charging/discharging capacity. Post-cycled electrodes were obtained by disassembling Swagelok cells inside an argon-filled glovebox. Electrodes were immersed in 25 mL dimethyl carbonate (DMC, Gotion) for 5 min, and then rinsed with 2 mL fresh DMC with a dropper to remove the residual $LiFP_6$ and EC.

3.3.3 Microstructure Characterization

The mass and thickness of composite electrodes before and after electrochemical cycling were measured by a balance (XS205 Dual Range Analytical Balance) and a micrometer (Mitutoyo), respectively. The microstructure of composite electrodes was characterized by a field emission scanning electron microscope (SEM, FEI Quanta 250). X-ray diffraction analysis of as-made and cycled electrodes was conducted using Siemens D5000 (Cu Kα radiation, λ= 0.154 nm, 40 kV, 30 mA, 0.02°/step, 0.5°/min). The cycled electrodes were sealed with Kapton tapes (KPTLS-1, *www. Kaptontape.com*) in the glovebox to avoid air exposure. The X-ray diffraction patterns are shown in Figure 3.1(b).

3.3.4 Environmental Nanoindentation

Environmental nanoindentation measurements were conducted using the same method introduced in Chapter 2. The maximum depth for electrodes at different SOCs in the 2nd cycle and after long-term cycling was set as 1500 nm and 2500 nm, respectively. 100 and 50 nanoindentation tests were conducted in each sample under dry and wet conditions, respectively. Indentation results were statistically analyzed using Gaussian function, as shown in Figure 3.1(c) and (d).

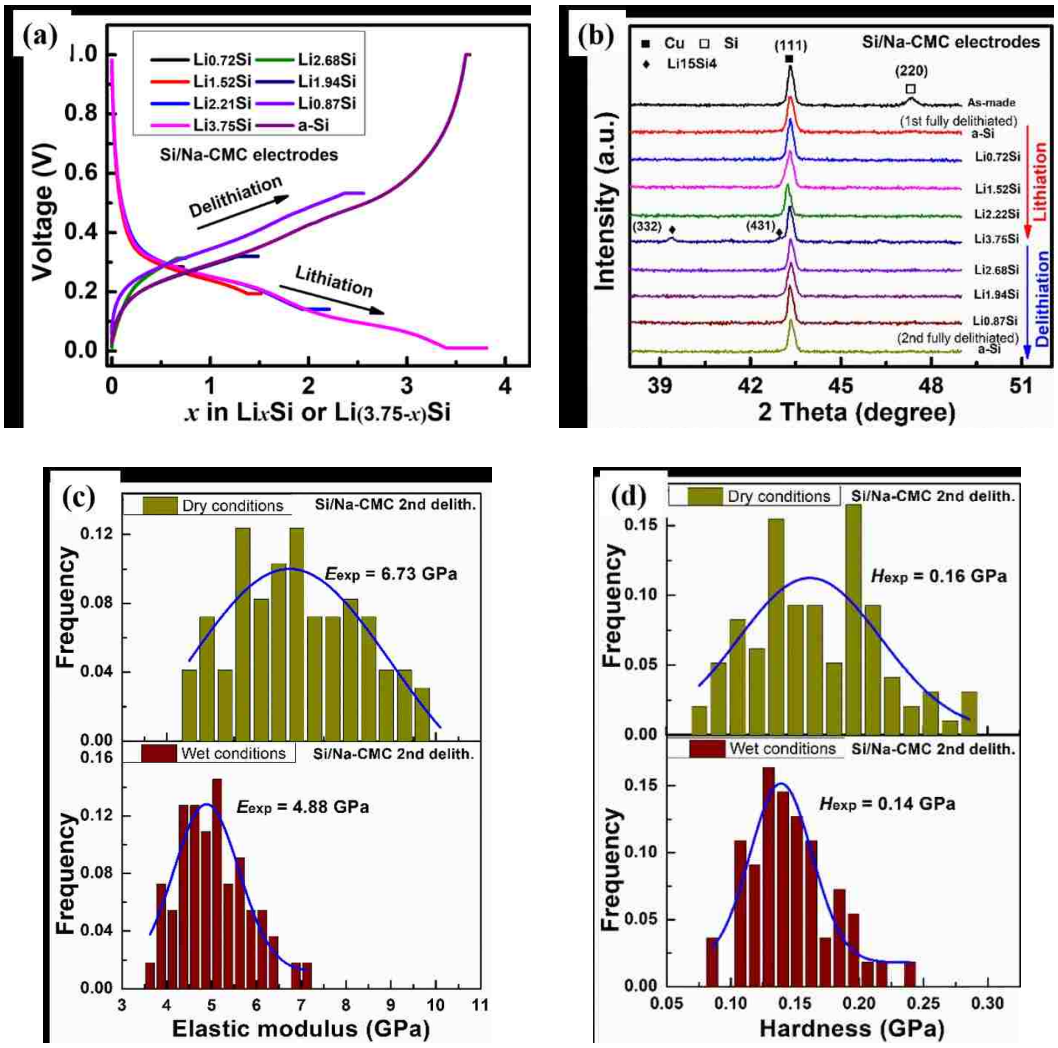

Figure 3.1 (a) Voltage profiles and (b) XRD patterns of Si/Na-CMC electrodes at different SOCs during the 2nd cycle. The 1st and 2nd fully delithiated Si electrodes were denoted as a-Si. Distribution histograms of the (c) elastic modulus and (d) hardness of Si/Na-CMC electrodes at the 2nd delithiation state.

Binder thin films (with thickness greater than 40 μm) were prepared by coating their solutions on Si wafers followed by drying on a hot stage (50 ℃ for overnight) for nanoindentation measurements. The elastic modulus and hardness of binder films under dry and wet conditions were measured by nanoindentation using the same procedure and parameters as that for the Si composite electrodes.

3.3.5 Adhesive Lap Joint Shear Tests

Lap joint samples were prepared by putting 100 μL binder solution (10 wt%) between two Si wafers ($5\ mm \times 50\ mm \times 0.35\ mm$, P-type Si (100) wafer, Wafer World, as shown in Figure 3.2) followed by drying on a hot stage (50 ℃ in a hood) for overnight. Shear tests were conducted using a universal mechanical test machine (Instron 3345). The speed was set at 10 mm/min. The engineering shear strength (τ) was calculated by $\tau = F_{cf}/A$, where F_{cf} is the critical fracture load and A is the area of the joint.

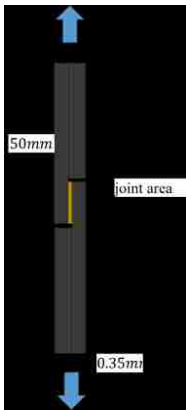

Figure 3.2 The schematic diagram of Si/binder/Si lap joint samples for shear tests.

3.4 Results and Discussion

As shown in Figure 3.1(b), X-ray diffraction (XRD) patterns show that crystalline Si particles in the as-made electrodes transform to amorphous Si after the 1st cycle. Li_xSi particles remain amorphous during the repeated lithiation/delithiation process, except that crystalline $Li_{3.75}Si$ forms at the full lithiation state. Similar phenomenon has been found in Si/PVDF electrodes [113]. Considering the phase transformation from pristine crystalline Si to amorphous Li_xSi and the excessive SEI formation in the 1st cycle, electrodes at different SOCs for nanoindentation measurements were obtained in the 2nd cycle. Due to

the random nature of porous composite electrodes, the measured E and H under both dry and wet conditions distribute in a range. We use Gaussian function (Eq. (2.1)) to analyze the distribution of E and H. Typical histograms of E and H are shown in Figure 3.1(c) and (d).

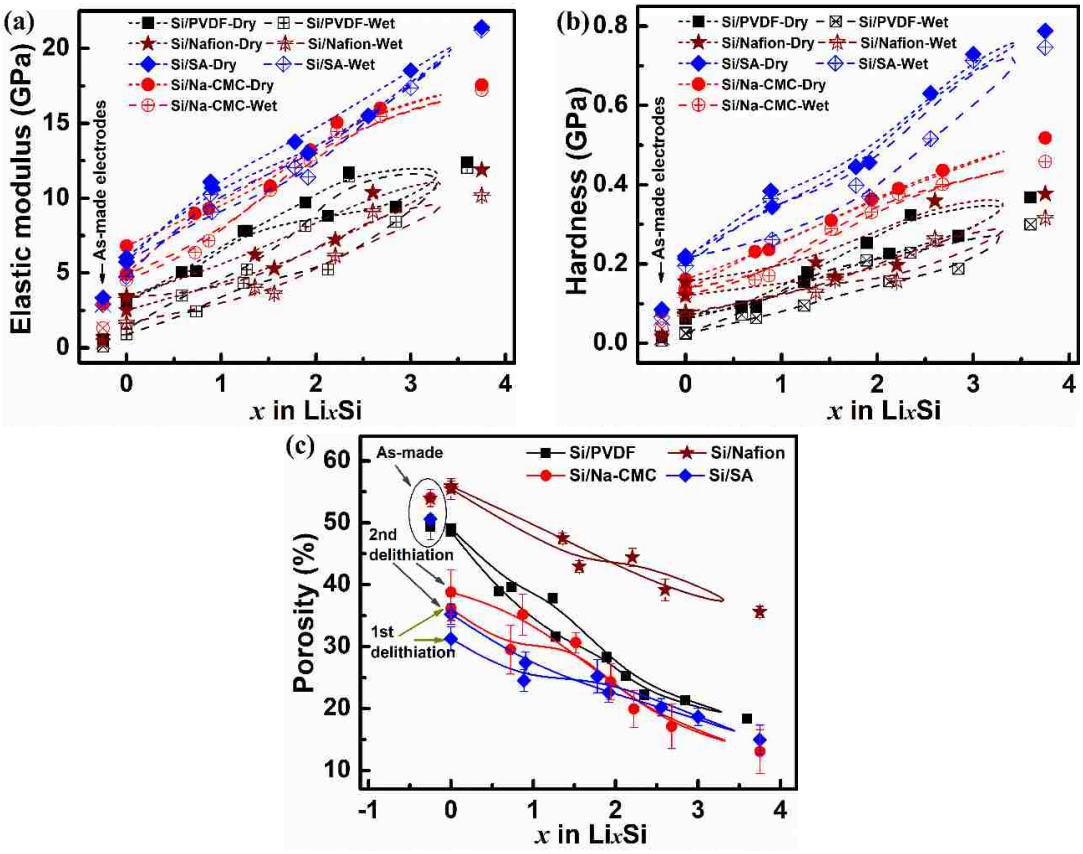

Figure 3.3 The evolution of the expectation values of (a) the elastic modulus and (b) hardness of Si composite electrodes measured under both dry and wet conditions. The values of E_{exp} and H_{exp} are listed in Table 3.2. (c) The evolution of the porosity of Si composite electrodes during the 2nd cycle. The porosity was determined using Eq. (2.2)-(2.5) with the mass and thickness of the cycled electrodes measured under dry conditions.

Figure 3.3(a), (b) and Table 3.2 show the expectation values of elastic modulus, E_{exp}, and hardness, H_{exp}, *vs.* the lithium concentration (x in Li$_x$Si), respectively. Both E_{exp}, and H_{exp} of the 1st and 2nd fully delithiated electrodes are higher than that of the as-prepared ones. In contrast to lithiation induced softening of electrodes made of Si alone (*e.g.*, Si individual particle, thin films, and Si wafer electrodes) [70-73], E_{exp} and H_{exp} of Si composite electrodes increase with increasing lithium concentration during lithiation

and decrease as lithium concentration decreases during delithiation. Electrodes at the full lithiation state have the largest E_{exp} and H_{exp}. For example, E_{exp} of Si/SA is 5.74 GPa at the 1st full delithiation state. It increases almost linearly to the peak value of 21.40 GPa at the 2nd full lithiation state and then decreases to 6.04 GPa during the 2nd delithiation process, as shown in Table 3.2. The magnitudes of E_{exp} and H_{exp} of electrodes at the same SOC follow the sequence of Si/Nafion < Si/PVDF < Si/Na-CMC < Si/SA. In addition, E_{exp} and H_{exp} measured under wet conditions are smaller than that under dry conditions. In the following sections, we propose the mechanisms responsible for (1) the increasing trend of *E* and *H* of Si composite electrodes with increasing lithium concentration, (2) binder-dependent *E* and *H* of Si composite electrodes, and (3) the softening behavior of Si composite electrodes in the electrolyte.

Table 3.2 Expectation values of the elastic modulus (*E*) and hardness (*H*) of Si composite electrodes at different SOCs

SOCs (*x* in Li_xSi)	**Si/Na-CMC**				**SOCs (*x* in Li_xSi)**	**Si/SA**				**SOCs (*x* in Li_xSi)**	**Si/Nafion**			
	Under dry conditions		Under wet conditions			Under dry conditions		Under wet conditions			Under dry conditions		Under wet conditions	
	E_{exp} / GPa	H_{exp} /GPa	E_{exp} / GPa	H_{exp} /GPa		E_{exp} / GPa	H_{exp} /GPa	E_{exp} / GPa	H_{exp} /GPa		E_{exp} / GPa	H_{exp} /GPa	E_{exp} / GPa	H_{exp} /GPa
As-made	2.93	0.08	1.32	0.04	As-made	3.35	0.09	2.89	0.06	As-made	0.47	0.02	0.42	0.01
0 (1st delith.)	4.97	0.13	4.52	0.12	0 (1st delith.)	5.74	0.21	4.75	0.19	0 (1st delith.)	2.51	0.12	1.66	0.07
0.72	8.98	0.23	6.37	0.16	0.89	11.11	0.38	10.26	0.36	1.56	5.30	0.17	3.65	0.16
1.52	10.82	0.31	10.54	0.29	1.78	13.77	0.45	12.05	0.40	2.2	7.22	0.20	6.14	0.16
2.22	15.07	0.39	14.46	0.38	3.00	18.53	0.73	17.37	0.71	3.75	11.89	0.38	10.19	0.32
3.75	17.58	0.52	17.22	0.46	3.75	21.40	0.79	21.22	0.75					
2.68	16.02	0.44	15.47	0.40	2.55	15.48	0.63	15.51	0.52	2.60	10.38	0.36	9.12	0.26
1.94	13.22	0.36	12.52	0.33	1.92	13.03	0.46	11.41	0.37	1.36	6.22	0.20	4.06	0.13
0.87	9.32	0.24	7.16	0.17	0.90	10.71	0.34	9.09	0.26	0	3.44	0.16	3.35	0.08
0	6.80	0.16	4.84	0.14	0	6.04	0.22	5.76	0.22					

The mechanical properties of porous composites highly depend on their porosity. We determined the porosity of Si composite electrodes under dry conditions based on the relationship between mass, volume, density of each component, and crack spacing in the electrodes. As shown in Figure 3.3(c), the porosity of composite electrodes decreases continuously during lithiation due to the volume expansion of Li_xSi particles. It reaches the lowest value after full lithiation and then gradually increases to a level close to that at the 1st delithiation state as Li_xSi particles contract during the 2nd delithiation process.

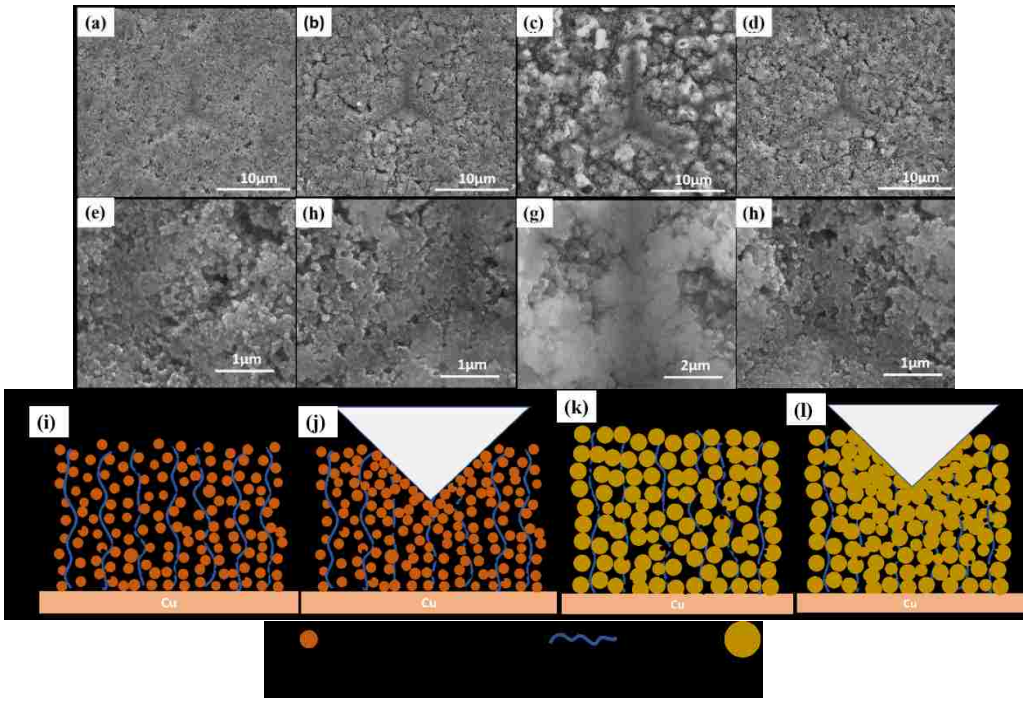

Figure 3.4 Typical indents in (a) the as-made, (b) the 1st delithiated, (c) the 2nd lithiated, and (d) the 2nd delithiated Si/Na-CMC electrodes. (e)-(h) are high magnification SEM images of indents corresponding to (a)-(d), respectively. (i) and (j) are schematic diagrams of the as-made and fully delithiated electrodes before and after indentation measurements, respectively. (k) and (l) are schematic diagrams of the fully lithiated electrodes before and after indentation measurements, respectively.

The deformation mechanism is strongly affected by the porosity of the composite electrodes. As shown in Figure 3.4(a)-(h), similar to Si/PVDF electrodes [113], most Si particles in the indents in the highly porous as-made, the 1st delithiated, and 2nd delithiated Si/Na-CMC electrodes remain undeformed. In contrast, Li_xSi particles in the 2nd lithiated electrode are clearly deformed by the indenter. Similar phenomenon has also been found in Si/SA and Si/PVDF electrodes. Based on these observations, we propose a porosity-dependent deformation mechanism as follows: since the as-made and fully delithiated electrodes have high porosity, nanoindentation would induce the densification of the highly porous composites instead of deforming the small and stiff Si particles, shown in Figure 3.4(i) and (j). Compared with crystalline and amorphous Si, the highly porous binder/CB matrix has much smaller E and H values. As a result, the measured E and H of the as-made and fully delithiated composite electrodes are small. As the lithium concentration increases, active particles expand and the porosity of electrodes decreases. Densification completes

at a shallow indentation depth, shown in Figure 3.4(k) and (l). The deformation of Li_xSi particles increasingly contributes to nanoindentation responses, resulting in higher *E* and *H* values although Li_xSi particles soften as the lithium concentration increases. The net effect of the porosity-dependent deformation mechanism (densification *vs.* deformation of Li_xSi particles) and the softening of Li_xSi particles is an increase in *E* and *H* of Si composite electrodes as the lithium concentration increases.

As shown in Figure 3.3(a) and (b), *E* and *H* of Si electrodes at the same SOC depend on the types of binders. Their values are, generally, in the sequence of Si/Nafion < Si/PVDF < Si/Na-CMC < Si/SA under both dry and wet conditions. The influence of binders on the mechanical properties of Si composite electrodes may be attributed to three major factors: (1) mechanical properties of binders, (2) porosity changes, and (3) the adhesion between binders and Si.

Nanoindentation measurements (Figure 3.5(a)-(c)) show that the magnitudes of *E* and *H* of binders under dry and wet conditions follow the sequence: SA > Na-CMC > PVDF > Nafion, which is consistent with the magnitudes of *E* and *H* of Si composite electrodes made of different binders. In our unpublished work, the magnitude of the instantaneous modulus of these binders follows the same trend. Lap joint shear tests (Figure 3.5(d)) show that the adhesion strength of the Nafion/Si interface is more than 80 times higher than that of the PVDF/Si interface and 4 times higher than that of the SA/Si and Na-CMC/Si interfaces. Nevertheless, the porosity of Si electrodes at different SOCs follows: Si/Nafion > Si/PVDF > Si/Na-CMC > Si/SA (as shown in Figure 3.3(c)), although Si/SA and Si/Na-CMC electrodes have very similar porosity when $x \geq 1.8$). Therefore, the mechanical properties of binders, instead of the adhesion between binders and Si, strongly affect the porosity change and the magnitude of *E* and *H* of Si composite electrodes during cycling. Compared with soft binders (Nafion and PVDF), stiff binders (Na-CMC and SA) can effectively bind and constrain active particles, suppressing the irreversible volume change, and strengthening the composite electrodes.

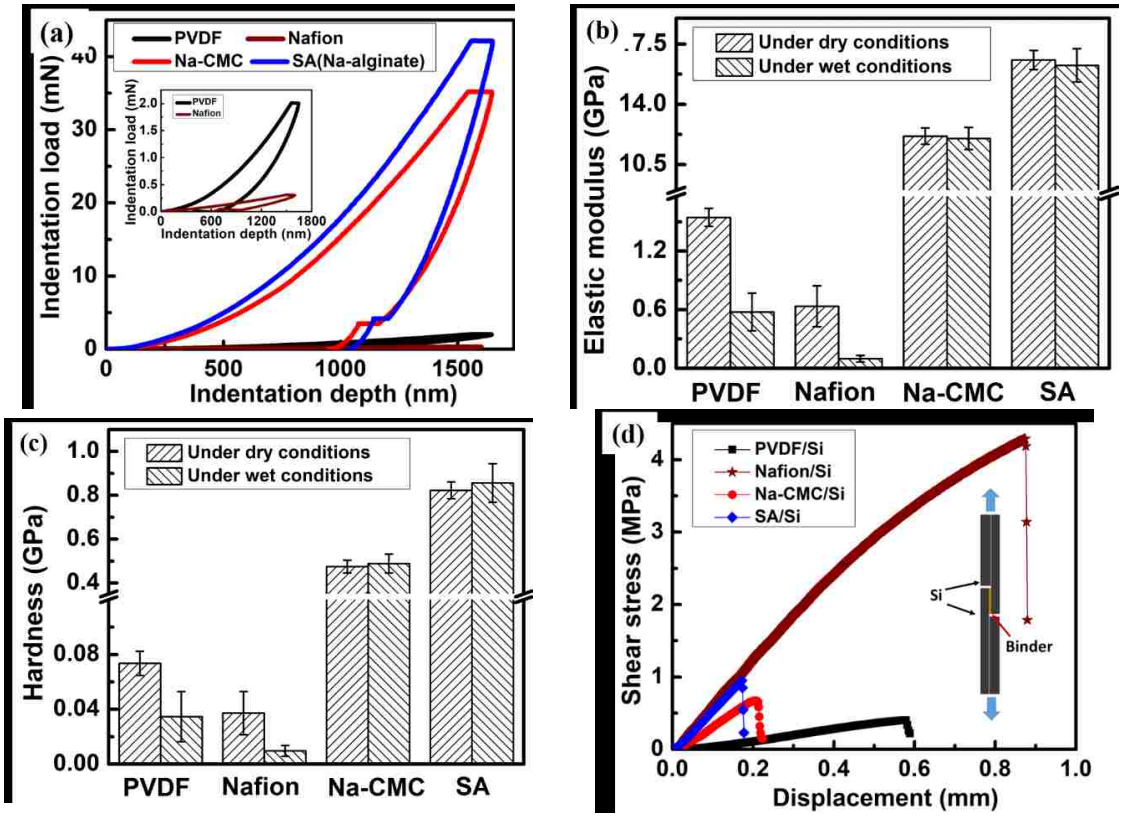

Figure 3.5. (a) Load-displacement curves of PVDF, Nafion, Na-CMC, and SA thin films. (b) The elastic modulus and (c) hardness of binder films measured under dry and wet conditions. (d) The shear stress-displacement profiles of Si/binder/Si lap joints.

To quantify the relationship between *E*, porosity, and binders of Si composite electrodes, we consider pores as a component in the composite electrodes. Based on the rule of mixture [114], theoretical modulus of Si composite electrodes is,

$$E_{theo} = \sum_1^i E_i V_i \tag{3.1}$$

where E_i is the elastic modulus and V_i is the volume ratio of the *i* component. *E* of pores is zero. *E* values of binders are measured by depth-controlled nanoindentation with the same measurement parameters as that used for measuring the Si composite electrodes. As shown in Figure 3.6(a), E_{theo} is different from E_{exp} measured by nanoindentation. The E_{exp}/E_{theo} *vs.* porosity profiles of Si/PVDF, Si/Na-CMC, and Si/SA electrodes follow the same trend, as shown in Figure 3.6(b). Because nanoindentation is unlikely to cause the interface separation between particles and binders in the cycled electrodes, we assume that the adhesion strength between particles and the matrix is strong and has negligible influence on *E* of Si composite electrodes. Analogous to Gibson and Ashby's model for cellular

solids [115], a polynomial relationship is proposed to describe the relationship between E_{theo}/E_{exp} and porosity (p),

$$E_{exp}/E_{theo} = 2.98p^2 - 2.72p + 1 \quad (3.2)$$

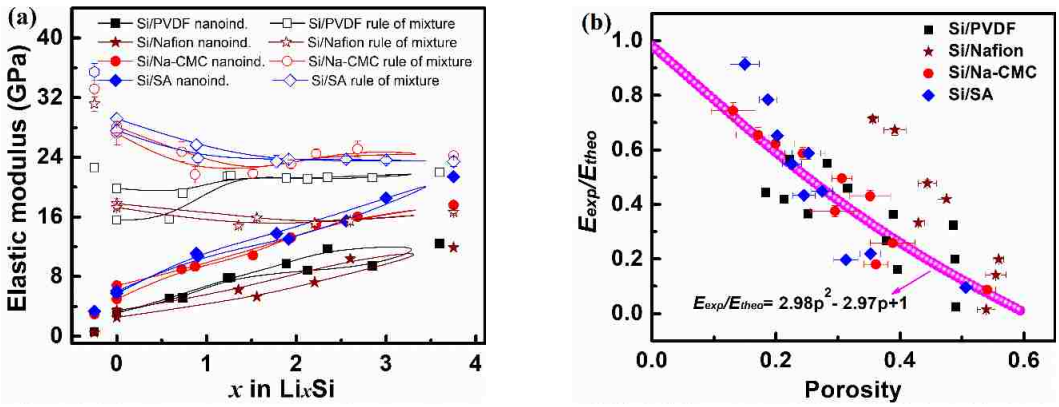

Figure 3.6. (a) A comparison between the elastic modulus measured by nanoindentation (under dry conditions) and calculated using the rule of mixture. (b) The relationship between the elastic modulus and porosity of Si composite electrodes in the 2nd cycle.

As shown in Figure 3.6(b), Eq. (3.2) fits well with the E_{exp}/E_{theo} *vs.* porosity profiles of Si/PVDF, Si/Na-CMC, and Si/SA electrodes. Conversely, E of these three composite electrodes after initial cycles may be obtained from Eq. (3.2) if the porosity and SOC of these electrodes are known. However, the relationship between E and porosity of Si/Nafion electrodes does not follow Eq. (3.2). We speculate that some $–SO_2OH$ in Nafion becomes $–SO_2OLi$ during electrochemical cycling, which is similar to the transformation of –COOH to –COOLi in the Si/PAA electrode during cycling [116]. Since the mechanical properties of Nafion-Li are different from Nafion [117], Eq. (3.1) and (3.2) cannot correctly predict E_{theo} of cycled Si/Nafion electrodes using the elastic modulus of Nafion.

As shown in Figure 3.3(a) and (b), E and H of electrodes measured under wet conditions are smaller than those measured under dry conditions as binders soften in the organic electrolyte. Binders also influence the softening behavior of Si composite electrodes under wet conditions. As shown in Figure 3.5(b) and (c), PVDF and Nafion films significantly soften in the electrolyte. For example, E and H of the Nafion film under wet conditions are 16 % and 26 % of that under dry conditions, respectively, while, E and H of Na-CMC and SA films under wet conditions are very close to that under dry conditions. The softening behavior of binders in the electrolyte effects the mechanical

properties of Si composite electrodes under wet conditions. As shown in Figure 3.3(a) and (b), Si/PVDF and Si/Nafion electrodes soften more than Si/Na-CMC and Si/SA electrodes in the electrolyte. Besides softening, swelling is another characteristic of Si composite electrodes and binders under wet conditions. Swelling ellipsometry measurements indicated that the thickness of a PVDF thin film increased by 18 % after immersed in the DEC vapor for 1000 s, while Na-CMC and SA films swelled only 0.5 % and negligibly, respectively [28, 30]. Therefore, the swelling of Si composite electrodes made with different binders is expected to be different. Since organic electrolytes cause softening and swelling of binders and composite electrodes, cautions should be taken when selecting mechanical properties and geometry dimensions of composite electrodes for electromechanical modeling.s

To better understand mechanical degradation, the irreversible thickness change and mechanical properties of Si composite electrodes during long-term cycling, up to 100 cycles, have also been investigated. Because Si/Nafion electrodes became very loose and disintegrated during the washing process in DMC after 10 cycles (see Figure 3.7), we focused on the mechanical degradation of Si/PVDF, Si/Na-CMC, and Si/SA electrodes.

Figure 3.7 A photo of a Si/Nafion electrode (after 10 cycles) rinsed with DMC. Most part of the electrode disintegrated and dispersed in DMC.

As shown in Figure 3.8(a), the thickness of electrodes, at full lithiation and delithiation states, increases with the cycle number. Due to the volume expansion of active particles, the thickness increment at the full lithiation state is larger than that at the full delithiation state. The irreversible thickness change of Si composite electrodes depends on the binders: (1) Si/SA and Si/Na-CMC electrodes have much smaller irreversible thickness change than the Si/PVDF electrode because Na-CMC and SA are much stiffer than PVDF and can restrict some expansion of the composite electrodes during lithiation and (2) the

strong interfaces in Si/Na-CMC and Si/SA, along with high stiffness, enable more volume contraction than Si/PVDF electrodes during delithiation.

The accumulated irreversible thickness change can lead to mechanical degradation of the Si composite electrodes during long-term cycling. As shown in Figure 3.8(b) and (c), *E* and *H* of Si electrodes at both fully lithiated and delithiated states decrease continuously during cycling. Due to the expansion of Si particles, the porosity of the fully lithiated electrode is smaller than that of the fully delithiation one. Porosity-dependent indentation deformation mechanisms (*e.g.*, densification *vs.* deformation of particles) result in larger *E* and *H* at the lithiation state than those at the delithiation state. During long-term cycling, Si composite electrodes under wet conditions have smaller *E* and *H* than those under dry conditions, which, again, can be attributed to the softening of binders in the electrolyte.

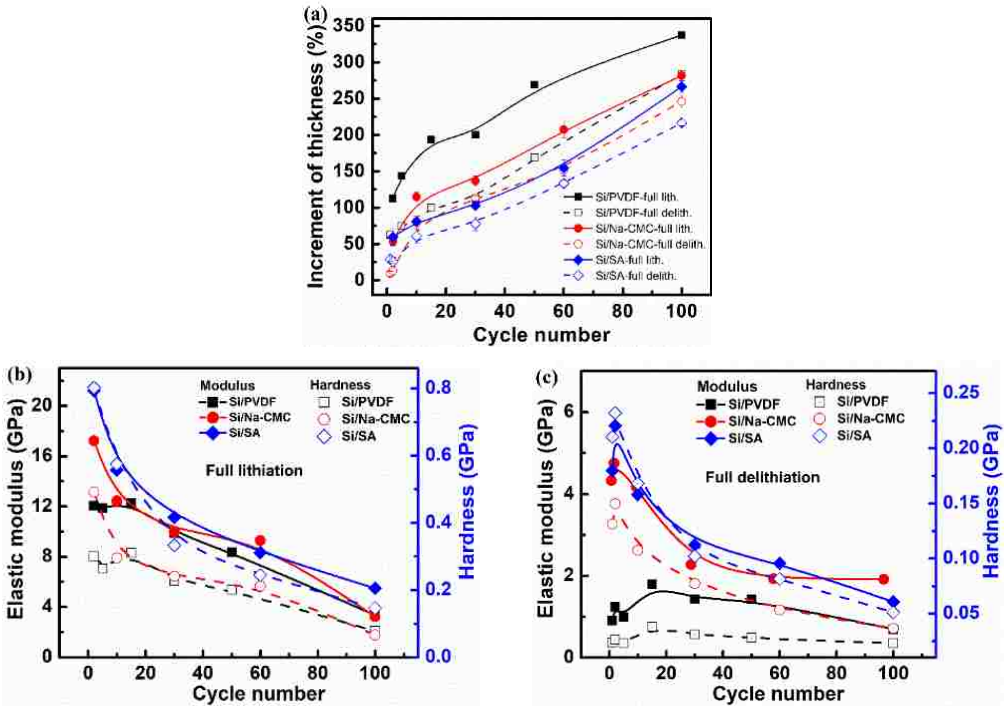

Figure 3.8. The thickness evolution of Si composite electrodes at the lithiation and delithiation states during long-term cycling. The evolution of *E* and *H* of Si composite electrodes at (b) the lithiation state and (c) the delithiation state during long-term cycling.

As the cycle number increases, the influence of binders on the values of *E* and *H* of Si composite electrode diminishes. For example, *E* of Si/SA electrodes at the 2nd lithiation

state is 9.8 GPa larger than that of Si/PVDF electrodes, while this difference reduces to 2.1 GPa after 100 cycles. As shown in Figure 3.5(a) and (b), the magnitudes of *E* and *H* of Si electrodes within 10 cycles are distinct, that is, Si/SA > Si/Na-CMC > Si/PVDF. After additional cycling, *E* and *H* of these three electrodes, especially at the full lithiation state, are quite close although they have different thickness changes and their binders have distinctly different mechanical properties. This diminishing effect of binders on mechanical properties of Si composite electrodes may be attributed to microstructure degradation.

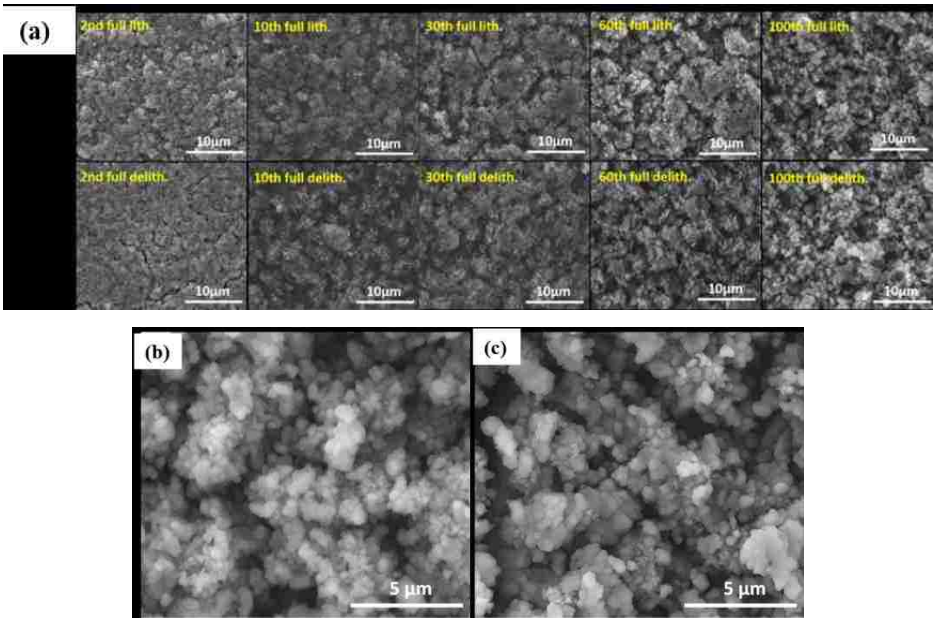

Figure 3.9 (a) The surface morphology change of the Si/Na-CMC electrodes during long-term cycling. High magnification SEM images of Si/Na-CMC electrodes after electrochemical cycling: (b) 100 cycles, at the full delithiation state, and (c) 100 cycles, at the full lithiation state.

As shown in Figure 3.9(a), an increasing number of Li_xSi particles agglomerate on the electrode surface as the cycle number increases. Recent X-ray tomography studies also observed similar phenomenon inside Si composite electrodes [26, 118]. The agglomerated particles on the surface remain the same size at the lithiation and delithiation states because they have, most likely, detached from the electrode (Figure 3.9(c) and (d)) and become inactive (due to poor electronic connection with the matrix). The spatial distribution of binders and CB also changes as particles agglomerate. In addition, pores in composite

electrodes may be filled with side reaction products, as confirmed by Radvanyi *et al*. [119] and Oumellal *et al*. [120]. These factors highlight the importance of measuring the mechanical properties of Si composite electrodes as a function of SOC and the cycle number since they may be too complex to be predicted theoretically.

Figure 3.10 shows the electrochemical performance of Si composite electrodes in half cells. The discharging capacity of Si/PVDF electrodes degrades quickly to 372 mAh g^{-1} after only 75 cycles at 0.2 C (1 C = 3579 mAh g^{-1}). In contrast, Si/Nafion, Si/Na-CMC, and Si/SA electrodes retain, after 100 cycles, a high capacity of 1295, 1680, and 1984 mAh g^{-1}, respectively. The better electrochemical performance of Si/Nafion, Si/Na-CMC, and Si/SA electrodes than the Si/PVDF electrode is consistent with previous studies [25, 28-30, 103].

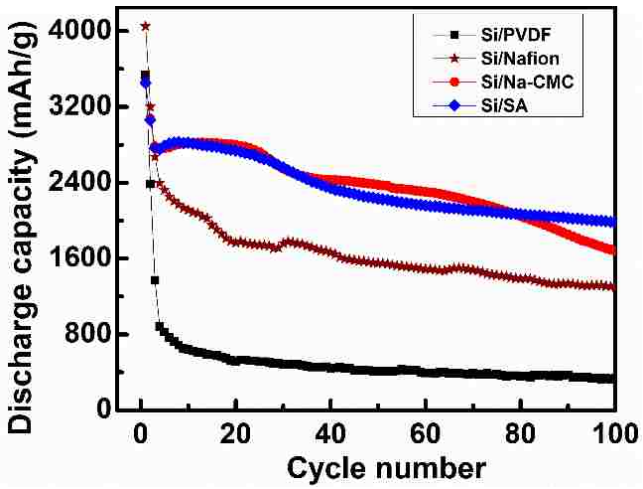

Figure 3.10. Electrochemical performance of Si composite electrodes made with different polymeric binders.

It has been recognized that the capacity fading of Si composite electrodes may be mainly attributed to electromechanical degradation, which includes irreversible volume change, delamination, fracture of Li_xSi particles, and loss of mechanical contacts, which reduced electronic conductivity between binders and Si particles [28, 30, 93, 94]. Although PVDF has fairly high *E* and *H*, the weak adhesion between PVDF and Si causes the faster degradation of Si/PVDF electrodes than Si/Nafion electrodes [103, 104]. Despite that Na-CMC and SA have lower adhesion strength with Si than Nafion, their high stiffness could well interlock Si particles and render Si composite electrodes better capacity retention. Our

comparative studies indicate that effective binders for Si composite electrodes can either have high *E* and *H* with sufficient adhesion with Si particles or have very strong adhesion with Si but low *E* and *H*. A balance between the binder/Si adhesion and mechanical properties may exist for effective binders, the quantifying and optimization of which need further investigations.

3.5 Conclusions

We measured mechanical properties of Si composite electrodes made of different binders at different SOCs and after different cycle numbers under both dry and wet conditions using an environmental nanoindentation system. Although lithiation induces softening of Si particles and thin films, the values of *E* and *H* of Si composite electrodes within each cycle increase with the lithium concentration due to the porosity change and porosity-dependent deformation mechanisms (densification *vs.* deformation of individual particles). We proposed an empirical model for predicating *E* of Si/PVDF, Si/Na-CMC, and Si/SA electrodes for short-term cycles, *i.e.*, first two cycles. The values of *E* and *H* of Si composite electrodes at the lithiation and delithiation states decrease as the cycle number increases. Mechanical property degradation is caused by the accumulated irreversible volume change during cycling. Si composite electrodes under wet conditions have smaller *E* and *H* than those under dry conditions because binders soften in the organic electrolyte. The softening behavior of Si composite electrodes depends on the softening of binders in the electrolyte. Although the adhesion strength between binders and Si is important for the electrochemical performance of Si composite electrodes, mechanical properties of binders largely determine the porosity, irreversible thickness changes, and magnitudes of *E* and *H* of Si composite electrodes at the same SOC during cycling. These results show that it is crucial to include the binder-, SOC-, and environment-dependent mechanical properties and microstructure in electromechanical modeling and analysis of Si composite electrodes and cell design. To fully understand the mechanical behavior of Si composite electrodes, one should further study the effects of particle size, initial porosity, ratio of components, external pressure, and electrolytes. Advanced electrochemical characterization techniques and our environmental nanoindentation provide a good opportunity to systemically study the influence of these factors on the electromechanical degradation of Si composite electrodes. Moreover, the environmental nanoindentation method, as shown in this study,

can measure mechanical properties of a wide range of electrochemical energy storage materials and electrodes in their realistic working environment, providing often unknown mechanical parameters for electromechanical analysis.

CHAPTER 4. CRACKING BEHAVIOR OF SI COMPOSITE ELECTRODES DURING ELECTROCHEMICAL CYCLING

4.1 Summary

Mechanical degradation caused by lithiation/delithiation-induced stress and large volume change is the primary cause of fast capacity fading of silicon (Si)-based electrodes. Although intensive efforts have been devoted to understanding electromechanically induced fractures of electrodes made of Si alone (*e.g.*, Si particles, Si thin films, and Si wafers), the cracking behavior of Si/polymeric binders/carbon black composite electrodes is unclear and poorly understood. Here, we investigate, by *in situ* and *ex situ* techniques, the cracking behavior of Si composite electrodes made with different binders, including polyvinylidene fluoride (PVDF), sodium-alginate (SA), sodium-carboxymethyl cellulose (Na-CMC), and Nafion. It is found that cracks form during the 1st delithiation process, periodically open and close during subsequent lithiation/delithiation cycles at the same locations in the Si composite electrodes made with SA, Na-CMC, and Nafion. In contrast, no crack forms in Si/PVDF electrodes. A possible mechanism is proposed to help understand the effects of binders on the cracking behavior (*e.g.*, crack spacing and island size) of Si composite electrodes. We also suggest possible approaches, including reducing the electrode thickness, patterning electrodes, and using highly recoverable binders, to inhibit cracks and improve the mechanical integrity of Si composite electrodes.

4.2 Introduction

Lithium ion batteries (LIBs) with high energy density and long cycle life play an essential role in the development of electric vehicles (EVs) and grid energy storage technology [121, 122]. To improve the energy density of LIBs, intensive efforts have been devoted to developing high capacity silicon (Si) negative electrodes because Si can deliver a high capacity of 3579 mAh g^{-1}, which is about ten times of that of commercial graphite electrodes [93, 123, 124]. However, it is still challenging to achieve satisfactory capacity retention and cycling stability of Si electrodes since the massive volume change ($\approx$300 %) of Si during repeated lithiation/delithiation causes fracture and electrical isolation of Si particles and continuous formation of solid electrolyte interphase (SEI) [13, 15, 125, 126]. One effective strategy to mitigate the electromechanical degradation of Si electrodes is to

use nanostructured Si [127], which are less likely to fracture during lithiation/delithiation due to the large constraint from their high surface energy [24]. For example, Li *et al.* found that a Si thin film could keep intact during electrochemical cycling if its thickness is less than 100 nm [15]. Using an *in situ* transmission electron microscopy, Liu *et al*. observed that the fracture of individual Si particles is inhibited by reducing the particle size down to 150 nm [13]. On this account, Si nanoparticles have been extensively used in composite electrodes, which are the most likely form of Si electrodes for LIBs from the consideration of energy density and cost. Typical Si composite electrodes are porous composites consisting of Si particles, carbon black (CB), and polymeric binders. Binders can bind Si particles and CB, maintain electronic network, and are, therefore, crucial to the performance of Si composite electrodes. It is known that polyvinylidene fluoride (PVDF) cannot accommodate the large volume change of Si particles due to its weak van der Waals interaction with Si [28, 30, 103, 104]. In contrast, binders with –OH, –COO-R, and -SO_2O-R (R can be H, Na, and Li) functional groups, such as sodium carboxymethyl cellulose (Na-CMC) [28, 84], sodium alginate (SA) [25, 30], poly(acrylic acid) (PAA) [27, 28], and Nafion [25, 29], can form strong hydrogen bonds with Si, maintain the electronic connection between Si and the binder/CB matrix, and improve the performance of Si electrodes.

During lithiation/delithiation, the volumetric expansion/contraction of Si particles causes structural changes of Si composite electrodes. Recent research has found that Si composite electrodes, even made with Si nanoparticles, can crack at the micrometer length scale during electrochemical cycling [109, 116, 128, 129]. Moreover, binders influence the cracking features, such as crack density and crack spacing, of Si composite electrodes [109, 116, 130]. These cracks may facilitate the degradation of Si composite electrodes and should, therefore, be considered in the design of Si composite electrodes and LIBs. However, it is still unclear (1) why and how cracks form, (2) how cracks evolve during electrochemical cycling, (3) what is the relationship between the cracking behavior and properties of binders, and (4) how to inhibit cracks in Si composite electrodes.

To understand the above questions, we investigate the cracking behavior of Si composite electrodes made with different binders, including SA, Na-CMC, Nafion, and PVDF. The evolution of cracks during electrochemical cycling is captured by both *in situ*

and *ex situ* techniques. Mechanical properties, including the elastic modulus and hardness, of binders and Si composite electrodes and the adhesion between Si and binders, were compared to explore the mechanism on how binders influence the cracking behavior of Si composite electrodes. A model was proposed for the formation and evolution of cracks in Si composite electrodes. Furthermore, we suggest several methods to inhibit cracks in Si composite electrodes during cycling.

4.3 Experimental

4.3.1 Electrode Preparation

A detailed procedure for preparing Si composite electrodes with different binders can be found in Chapter 2 and 3. All electrodes were calendered to a porosity of 50±5 % with average thickness and mass loading of 41-43 μm and 0.85-0.95 mg cm^{-2}, respectively.

4.3.2 Electrochemical Tests

Half-cell tests were conducted using a Bio-Logic potentiostat (VMP-3) with a lithium foil (0.75 mm, Alfa Aesar) as the counter and reference electrodes. Swagelok cells were used to avoid deformation and cracking of electrodes during the disassembling process [113]. The electrolyte is 1M $LiPF_6$ in ethylene carbonate and diethyl carbonate solution (EC: DEC = 1:1 wt%, Gotion) with 10 wt% fluoroethylene carbonate (FEC, Gotion) as the additive. A galvanostatic-potentiostatic mode with a voltage window of 0.01 to 1.00 V was used to homogenize the distribution of lithium in Si composite electrodes. The discharging/charging rate of the galvanostatic mode and the current limit of the potentiostatic mode are C/20 and C/400, respectively.

4.3.3 Microstructure Characterizations

The microstructure of Si composite electrodes at different states of charge (SOCs) was characterized by a scanning electron microscope (SEM, FEI Quanta 250). Cross-sections of electrodes at the 2nd delithiation state were prepared with ion milling (Hitachi IM 4000 Plus). *In situ* observations of the crack evolution were conducted using a digital microscope (Dino-Lite Pro AM4113T) and a homemade optical cell, as shown in Figure 4.1. Many bubbles were generated during the 1st lithiation, which obscured the *in situ*

observation. We tilted the optical cell to remove the bubbles after the 1st cycle. Both Video 1 and 2 start from the 2nd cycle.

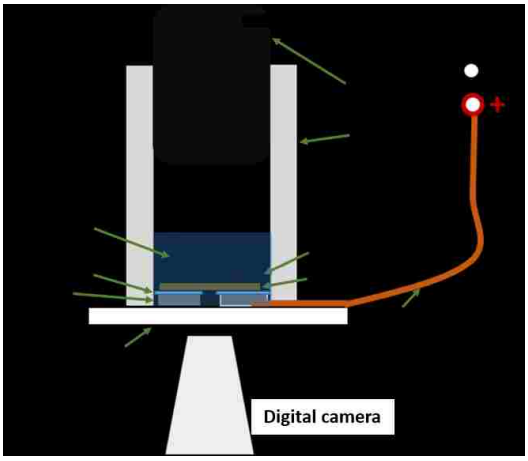

Figure 4.1. A schematic diagram of the optical cell for *in situ* observations the cracking behavior of Si composite electrodes.

4.4 Results and Discussion

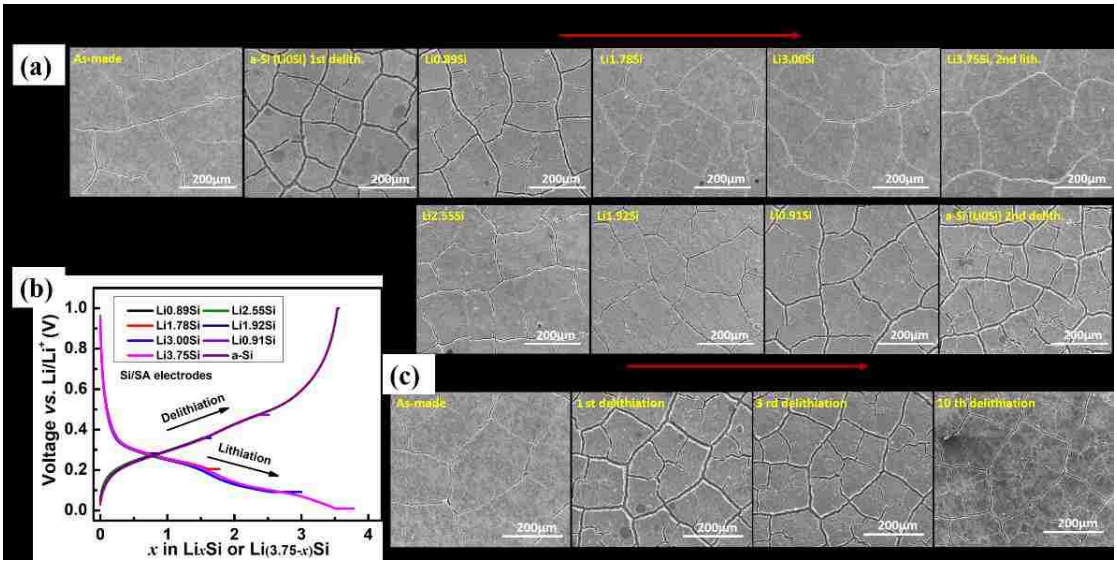

Figure 4.2. (a) *Ex situ* observations of the crack evolution in Si/SA electrodes during the 2nd cycle. (b) Voltage profiles of Si/SA electrodes at different SOCs in the 2nd cycle. (c) *Ex situ* observations of cracks in Si/SA electrodes at the same locations during multiple cycles.

As shown in Figure 4.2(a) and Figure 4.3, cracking happened in the as-made Si electrodes with SA, Na-CMC, and Nafion as binders due to the in-plane tensile stress

induced by the fast evaporation of their solvent (*i.e.*, H_2O), while cracks were not found in the as-made Si/PVDF electrode, as shown in Figure 4.3(m), probably because of the slow evaporation rate of NMP, which renders particles enough time to rearrange their positions to relax the drying-induced tensile stress [131, 132].

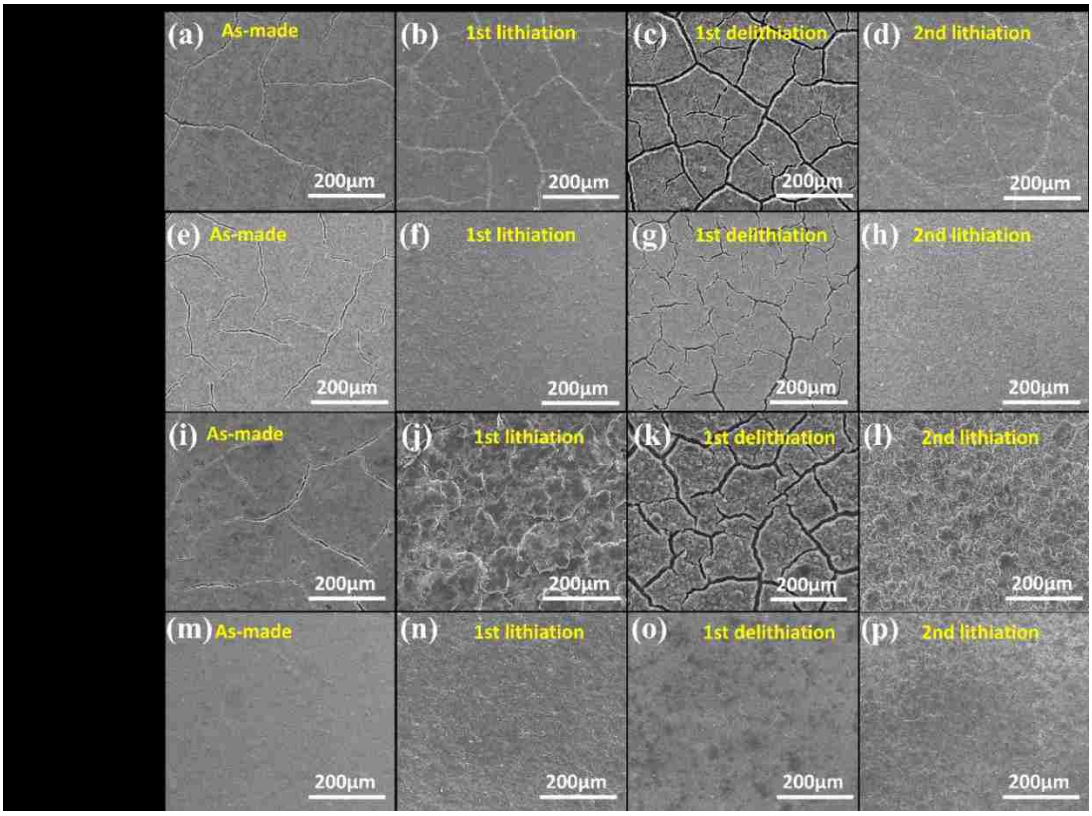

Figure 4.3 The microstructure evolution of Si composite electrodes during initial cycles.

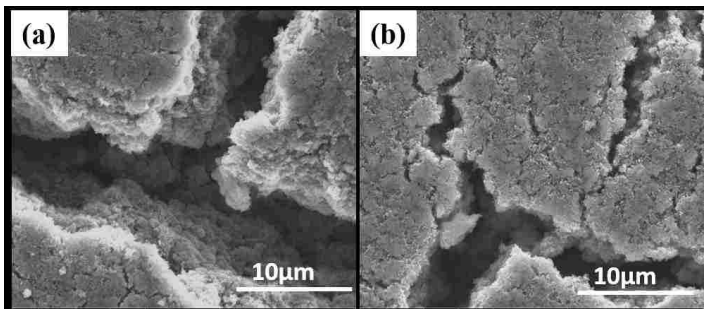

Figure 4.4 High magnification SEM images of cracks in (a) Si/SA and (b) Si/Na-CMC electrodes.

As shown in Figure 4.3, cracks in the as-made electrodes close after the 1st lithiation, while extensive random channel cracks form in the Si/SA, Si/Na-CMC, and

Si/Nafion electrodes after the 1st delithiation. For example, the Si/SA electrode is separated into many irregular shaped islands separated by wide and deep primary cracks. Some narrow secondary cracks form within individual islands. Since the dimension of primary cracks is much larger than that of Si nanoparticles (Figure 4.4), the fracture of the binder/CB matrix, instead of individual Si particles, is the likely cause of the cracks. In the 2nd cycle, cracks formed after the 1st full delithiation gradually close during lithiation and reopen during the subsequent delithiation (see Figure 4.2(a)). At the 2nd delithiation state, the island size and the spacing of primary cracks are similar to those at the 1st delithiation state. As shown in Figure 4.2(c), *ex situ* SEM observations show that cracks in the as-made Si/SA electrode reappear with larger crack spacing after the 1st delithation. Although additional secondary cracks form during subsequently cycling, all primary cracks at the 1st, 3rd, and 10th full delithiation states occur at the same locations. *In situ* digital microscope observations (Video 1) also show that cracks open and close periodically at the same locations during cycling. Remarkably, few delamination (*i.e.*, separation at the interface between the electrode and the copper conductor) events were observed despite of the large number of channel cracks. The periodic opening and closing of channel cracks suggest that the individual islands are electronically connected to the copper foil, allowing for the transport of electrons in and out of the islands during lithiation and delithiation.

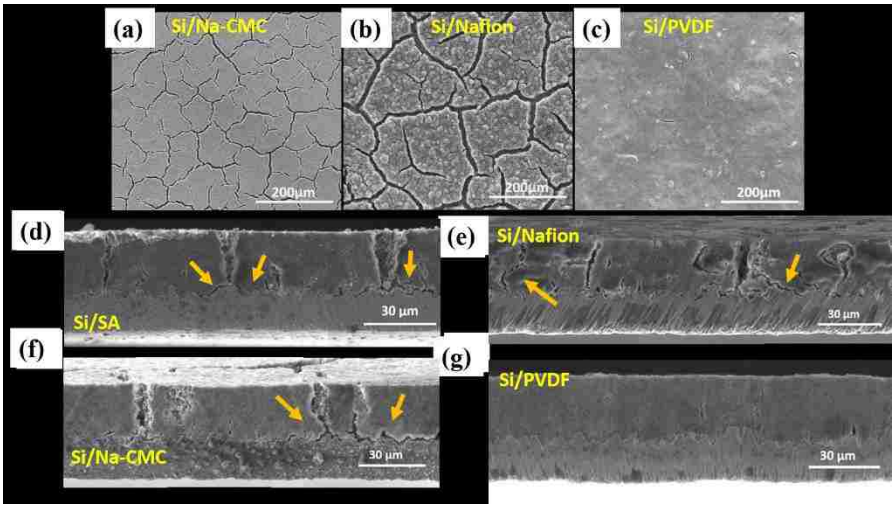

Figure 4.5 Surface morphology of (a) Si/Na-CMC, (b) Si/Nafion, and (c) Si/PVDF electrodes after the 1st delithiation. Cross sectional microstructure of (d) Si/SA, (e) Si/Nafion, (f) Si/Na-CMC, and (g) Si/PVDF electrodes at the 2nd delithiation state prepared by focused ion beam.

Channel cracks with distinct characteristics were also observed in Si/Na-CMC and Si/Nafion electrodes, as shown in Figure 4.5(a) and (b). For example, primary cracks in Si/Na-CMC electrodes are not always connected. At the delithiation state, islands in the Si/Na-CMC electrode are smaller than those in Si/SA and Si/Nafion electrodes. Si/Nafion electrodes have larger crack gap than Si/SA and Si/Nafion electrodes. As shown in Figure 4.6, cracks also periodically open and close at the same locations in Si/Na-CMC electrodes during cycling. Similarly, periodical cracking also happens in Si/Nafion electrodes. Cross-sectional SEM images show that primary cracks in Si/SA, Si/Na-CMC, and Si/Nafion electrodes reach the electrode/Cu current collector interface, deflect laterally, propagate along the interface, and lead to cracks at the electrode/Cu interfaces, as shown in Figure 4.5(d)-(f). In contrast, only several small cracks form on the surface and the cross-section of the Si/PVDF electrode after the 1st delithiation, as shown in Figure 4.5(c) and (g). After lithiation, the Si/PVDF electrode is also intact, as shown in Figure 4.3(n) and (p). Therefore, Si/PVDF electrodes do not crack, at least during initial cycles. Thus, the lithiation/delithiation-induced fracture and cracking behavior of Si composite electrodes depend on polymeric binders.

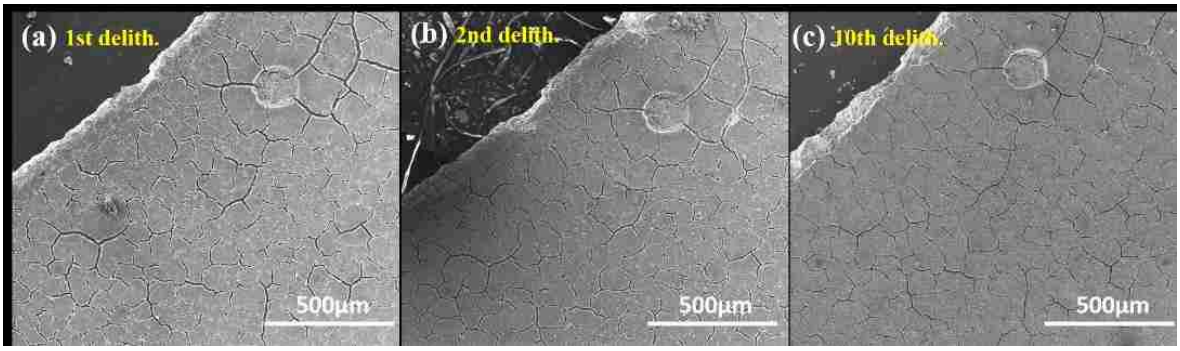

Figure 4.6 Microstructure of the Si/Na-CMC electrode at the delithiation state after different numbers of cycles. The large circle is a marker for locating cracks.

Channel cracking in elastic bilayer film/substrate systems depends on the energy release rate [133],

$$G = \frac{\pi(1-\mu_f^2)\sigma_f^2 h}{2E_f} g(\alpha,\beta) \quad (4.1)$$

where $\mu_f$is the Poisson's ratio of the film, h is the thickness of the film, E_f is the elastic modulus of the film, σ_f is the stress in the film normal to cracks before cracking, and $g(\alpha, \beta)$ is a function of the Dundurs parameters related to the elastic modulus and Poisson's ratio of the film and substrate. This model has been applied to analyze electrochemical-induced fractures of Si thin film electrodes [134-136]. Eq. (4.1) suggests that binder's role in the cracking behavior of Si composite electrodes originates from their influence on the thickness, elastic modulus, Poisson's ratio of Si composite electrodes, and lithiation/delithiation-induced stress, all of which are closely related to the mechanical properties of binders and the adhesion between binders and Si.

Table 4.1 Mechanical properties of binders and the shear strength of the binder@Si interface.

	SA	Na-CMC	Nafion	PVDF
E in the electrolyte / GPa [113]	16.26±0.96	12.01±0.64	0.099±0.034	0.58±0.19
H in the electrolyte / GPa [113]	0.85±0.090	0.49±0.040	0.0097±0.0043	0.035±0.018
σ_t of binders / MPa	close to that of Na-CMC [129]	54.5 [137]	~15 [117]	19.4 [137]
Maximum tensile strain / %	close to that of Na-CMC [129]	9.8 [137]	> 50 [117]	22.5 [137]
Thickness of electrodes (with Cu) after the 1st delithiation / μm	45	44	55	50
Shear strength of the binder@Si interface / MPa [138]	1.03±0.08	0.71±0.18	4.00±1.19	0.12±0.01

Environmental nanoindentation measurements (Table 4.1) show that PVDF and Nafion immersed in the electrolyte have quite small elastic modulus (*E*, < 0.8 GPa) and hardness (*H*, < 0.05 GPa), while *E* and *H* of SA and Na-CMC are larger than 12 GPa and 0.4 GPa, respectively. Nafion has the smallest *E* and *H* among these binders. Tensile tests by Garsuch and Kawano show that the values of engineering tensile strength (σ_t) of binders decreases in the following sequence, SA > Na-CMC > PVDF > Nafion [117, 137]. The maximum tensile strain of binders shows the opposite trend (see Table 4.1). Binders can

influence the mechanical property evolution and thickness change of Si composite electrodes during lithiation and delithiation. Environmental nanoindentation measurements show that the expectation values of *E* and *H* of Si composite electrodes at the 2nd delithiation state also decrease as that of the binders: Si/SA > Si/Na-CMC > Si/PVDF > Si/Nafion (Figure 4.7). Our previous study found that the *E* and *H* of Si composite electrodes with different binders at the same SOCs, in general, also follow the same trend [138]. After the 1st cycle, electrodes made with stiffer binders (SA and Na-CMC) have significantly smaller thickness increments than those made with softer binders (Nafion and PVDF), as shown in Table 1. Since the *E* and *H* values of Si/PVDF are in between that of electrodes with stiff binders (Si/SA and Si/Na-CMC) and soft binders (Si/Nafion) and since Si/PVDF electrodes do not crack, the *E* and *H* values of binders and Si composite electrodes do not seem to dictate the cracking behavior of Si composite electrodes.

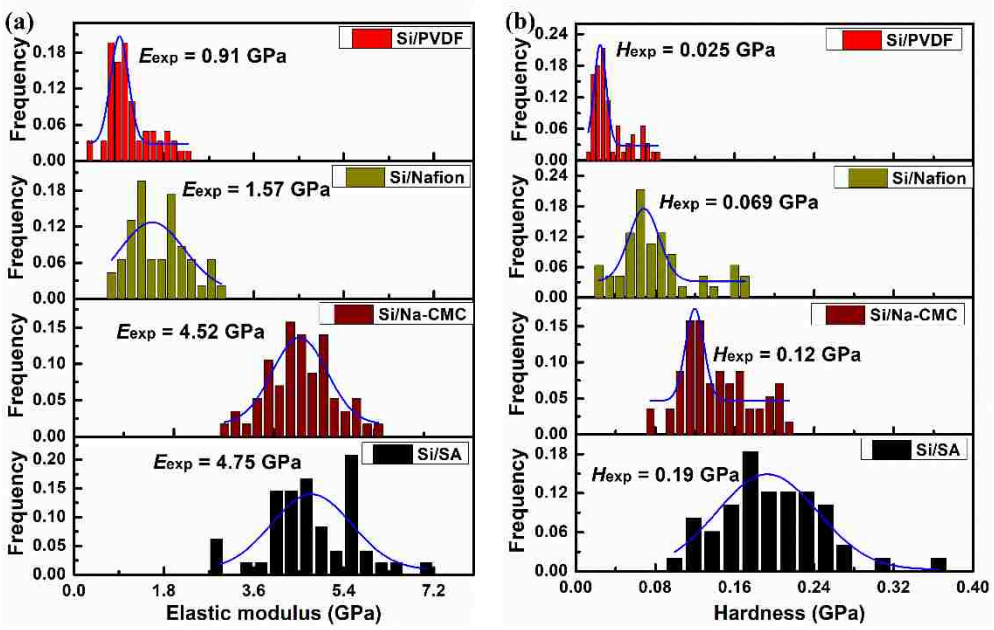

Figure 4.7 Distribution histograms of the (a) elastic modulus and (b) hardness of Si composite electrodes in the electrolyte at the 1st delithiation state.

The cracking behavior of Si composite electrodes is expected to be affected by the lithiation/delithiation-induced stress. *In situ* stress measurements have shown that binders can indeed influence the stress evolution of Si composite electrodes during cycling [69, 139, 140]. For example, Si/PVDF electrodes experience significantly smaller compressive

stress than Si/Na-CMC, Si/Nafion, and Si/SA electrodes during lithiation [139]. Although tensile stress has been measured in Si thin film and Si wafer electrodes during delithiation [135, 136, 141], no tensile stress has been detected in Si composite electrodes by substrate curvature measurements during delithiation in literature, probably because the tensile stress is local and it relaxes upon electrode cracking during delithiation. Thus, the cracking of Si composite electrodes cannot be quantified by Eq. (4.1).

Since binders transfer the mechanical interactions between Si particles and the binder/CB matrix, the adhesion strength between binders and Si may be a major factor responsible for the cracking behavior because it determines localized tensile stress in the composite induced by the volumetric contraction of Si during delithiation. Lap joint shear tests showed that the averaged adhesion strength of the Nafion@Si interface is about 4 times of the SA@Si and Na-CMC@Si interfaces and about 40 times of the PVDF@Si interface [138], as shown in Table 1. Qualitatively, the adhesion strength measured by lap joint shear tests is consistent with the peeling tests [103]. The strong adhesion of the SA@Si, Na-CMC@Si, and Nafion@Si interfaces results from the hydrogen bond between Si and these binders, while the weak adhesion of the PVDF@Si interface can be attributed to the weak van der Waals interaction between PVDF and Si [30, 103, 104]. Since PVDF has large electrolyte up-take capability, excessive SEI forms between PVDF and Si particles, which weakens the bonding between Si and PVDF, as confirmed by the large SEI and charge transfer resistance after delithiation later in Chapter 5. As a result, small localized tensile stress is generated in the Si/PVDF electrode as Li_xSi particles contract, which makes the cracking of the flexible Si/PVDF electrode unlikely. Despite that Nafion is more flexible than PVDF and that Si/Nafion electrodes have lower E and H than Si/PVDF electrodes, the strong adhesion between Si and Nafion enables the contraction of Si particles to induce large localized tensile stress to crack the Si/Nafion electrode.

Based on the above discussion, we propose the following the cracking mechanism for Si/SA, Si/Na-CMC, and Si/Nafion electrodes. During the 1st lithiation, the expansion of Si particles drives the expansion of electrode islands and fills crack spacing in the as-made electrodes, as shown in Figure 4.8(a) and (b). Cracks close by physical contact, instead of chemical bonding, between particles. Due to the constraint of the Cu current collector, compressive stress is generated in the Si composite electrodes during lithiation.

During the 1st delithiation, the progressive contraction of Li_xSi particles causes the shrinkage of the composite electrodes through the interaction between binders and Li_xSi particles. The localized stress state gradually transforms from compressive stress to tensile stress, leading to the separation of electrode islands along the original cracks (cracks in the as-made electrodes) due to the weak physical contact between the islands. As delithiation proceeds, cracks gradually widen, grow deeper, connect with each other, and separate the electrodes into islands, as shown in Figure 4.8(c). When the energy release rate in individual islands exceeds the fracture toughness of the composite electrode, secondary cracks propagate within individual islands. Once extensive cracks form during the 1st delithiation, cracks periodically close and open at the same locations synchronously with the expansion and contraction of Li_xSi particles during cycling.

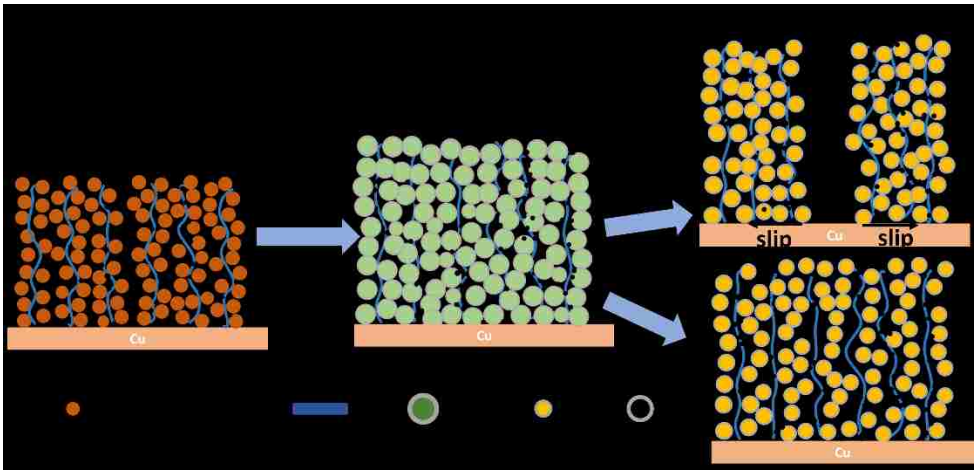

Figure 4.8. Schematic diagrams of the structural change of Si composite electrodes during cycling. (a) As-made Si composite electrodes, (b) electrodes after the 1st lithiation, (c) Si electrodes made with SA, Na-CMC, and Nafion after the 1st delithiation, and (d) Si/PVDF electrodes after the 1st delithiation.

The binder-dependent crack spacing and island size of Si composite electrodes is influenced by the adhesion of the electrode@Cu interface. If we assume that the Si composite electrodes are elastic-plastic solids that only undergo elastic deformation before the interfacial stress reaches its yield strength (σ_Y^{comp}) and neglect the delamination at the electrode@Cu interface, a shear-lag model can be used to model the cracking behavior of Si electrodes (Figure 4.9(a)) [15, 126]. By assuming that additional cracks form by plastic

deformation between two adjacent primary cracks, the force equilibrium at the critical state is [15, 126],

$$\tau_{cr}^{int} L_{cr}/2 = \sigma_Y^{comp} h \quad (4.2)$$

where τ_{cr}^{int} is the adhesion strength of the electrode@Cu interface (considering that the shear flow stress of Cu, $\tau_Y^{Cu} = \sim 40$ MPa [142], is much higher than the adhesion between electrodes and Cu), L_{cr} is the minimum crack space, and *h* is the thickness of the electrode. Eq. (4.2) suggests that the adhesion between the electrode and Cu influences the crack spacing in Si composite electrodes. Although the adhesion strength of the electrode@Cu interface in as-made electrodes has been measured by peel tests [103, 104, 143], the adhesion of the electrode@Cu interface after cycling, especially in the electrolyte, is unknown. If we further assume that the yield strength of the composite electrode is proportional to the nanoindentation hardness, $\sigma_Y^{comp} = cH$ (where *c* is a constant) [58], the adhesion strength of the electrode@Cu interface can be qualitatively determined by,

$$\tau_{cr}^{int} = 2cHh/L_{cr} \quad (4.3)$$

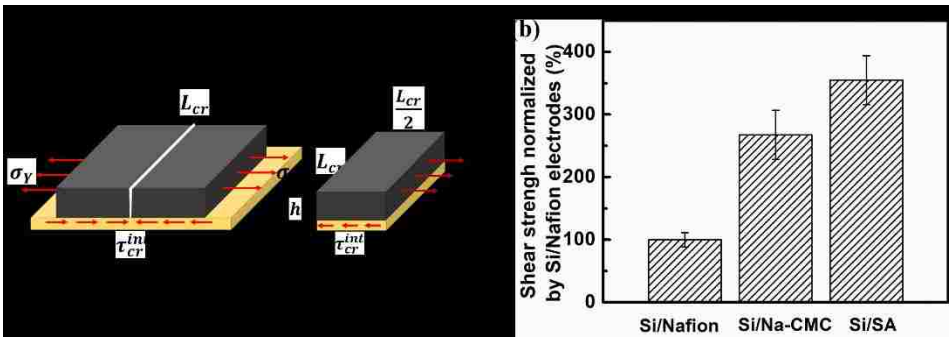

Figure 4.9. (a) A schematic diagram of the shear-lag model for cracks in Si electrodes. (b) The shear strength of the electrode/Cu interface normalized by Si/Nafion electrodes at the 1st delithiation state derived from Eq. (4.3).

As shown in Figure 4.9(b), the shear strength of the Si/Na-CMC@Cu and Si/SA@Cu interfaces is over 250% of that of the Si/Nafion@Cu interface after the 1st cycle. Although binders bridge between the electrode and Cu, the adhesion of the electrode@Cu interface cannot be judged by the bonding strength between binders and Cu. For example, our previous peel tests showed that the peel strength of the PVDF@Cu

interface is about four times larger than that of the SA@Cu interface. However, the peel strength of the Si/PVDF@Cu is only about 1/8 of that of the Si/SA@Cu interface [103].

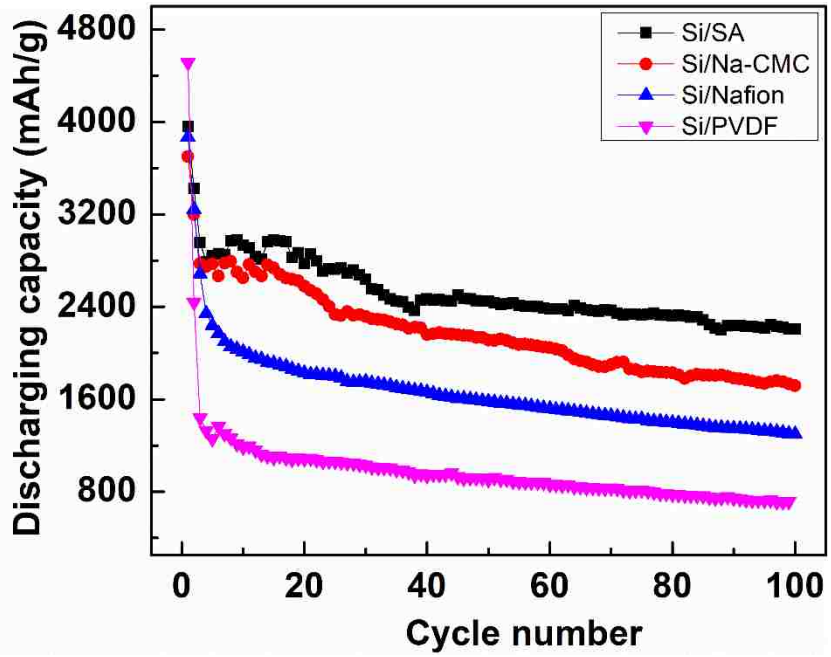

Figure 4.10 Discharging capacity-cycle number profiles of Si composite electrodes made with different binders.

Although Si/Nafion, Si/Na-CMC, and Si/SA electrodes experience severe cracking during cycling, they all have much better capacity retention than the seemingly integrate Si/PVDF electrode, as shown in Figure 4.10. The discharging capacity of the Si/PVDF electrode degrades quickly below 800 mAh g^{-1} after only 77 cycles. In contrast, Si/SA, Si/Na-CMC, and Si/Nafion electrodes retain a high capacity of 2205, 1716, and 1298 mAh g^{-1}, respectively, after 100 cycles. The better electrochemical performance of Si/SA, Si/Na-CMC, and Si/Nafions electrodes than the Si/PVDF electrode is consistent with previous studies [25, 28-30, 103]. The fast degradation of Si/PVDF electrodes is caused by the loss of electronic conductivity between Si particles and the PVDF/CB matrix (Figure 4.8(d), which can be attributed to the weak adhesion between PVDF and Si particles. Despite that channel cracks occur in Si/SA, Si/Na-CMC, and Si/Nafion electrodes, particles in individual islands still have good electronic connectivity with the binder/CB matrix due to the robust adhesion between Si particles and binders. Under external compressive pressures in coin cells and Swagelok cells, electrode islands may still be well connected with the

current collector, remain active, and retain capacity. Nevertheless, channel cracks and the incidental interfacial cracks are detrimental to microstructure integrity and increase the contact resistance of the electrode@Cu interface during long-term cycling, especially in large-format batteries (such as pouch cells) under low pressure. From this perspective, periodical channel cracks should be considered in the design of safe Si-based electrodes and batteries.

Based on Eq. (4.1) and (4.2), channel cracks in Si composite electrodes depend on the electrode thickness, the stress evolution during delithiation, the adhesion of the electrode@Cu interface, and the mechanical properties of electrodes. Considering these controlling factors, several strategies to inhibit cracks in Si composite electrodes emerge: (1) Reducing the electrode thickness. Based on Eq. (4.1), there is a critical thickness (h_c) for bilayer film/substrate systems, under which the film will not crack. For example, Si thin film electrodes with a thickness below 100 nm does not crack during electrochemical cycling [15]. Thin electrodes suppress the crack formation because small stress is generated during lithiation/delithiation due to their low mass loading. Composite electrodes also have a critical thickness. Take Si/SA electrodes as an example. As shown in Figure 4.11, the crack gap and area decrease as the electrode thickness decreases. There are no large and wide cracks in the Si/SA electrode with a thickness of 25 μm (mass loading of 0.11 mg cm^{-2}) although small cracks can still be found in the high magnification SEM image (Figure 4.11(e)). (2) Patterning composite electrodes. Based on Eq. (4.2), cracked films have a critical island size. Xiao *et al.* have shown that patterned Si thin film electrodes below the critical size could inhibit the formation of lithiation/delithiation-induced cracks in individual islands and improve electrochemical performance [126]. A similar patterning method may also be applicable to Si composite electrodes. (3) Using highly recoverable binders. We have shown, in this study, that the strong adhesion strength between binders and Si is essential to maintain the electronic conductivity of the composite electrodes but would induce large localized tensile stress and cracks during delithiation. If binders can be reversibly deformed to relax the localized tensile stress, cracks can be suppressed or "healed" spontaneously. One group of such binders is self-healing polymers, which have been shown to be effective in mitigating cracking of Si composite electrodes during cycling [102, 128, 129]. Among the above methods, reducing the electrode thickness and

patterning electrodes may not be practical from the consideration of energy density and manufacturing cost. Developing low cost, highly recoverable binders with robust adhesion with Si is a promising and scalable method to inhibit cracking and overcome the mechanical degradation of Si composite electrodes.

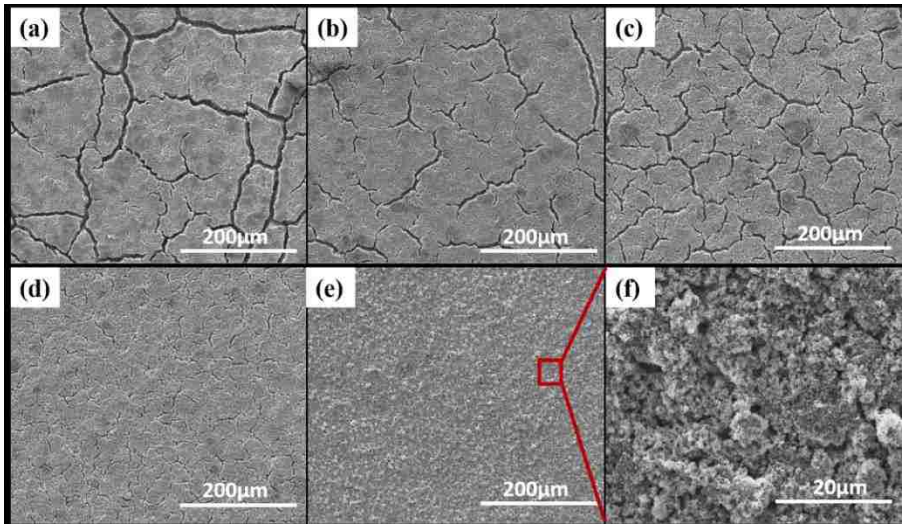

Figure 4.11 Surface morphology of Si/SA electrodes (consisting of 60 wt% Si, 20 wt% CB, and 20 wt% binder) with different thickness and mass loadings after the 2nd delithiation. The thickness (with 24 μm Cu foil) and mass loading of the as-made electrodes are (a) 49 μm, 0.92 mg cm^{-2}, (b) 38 μm, 0.58 mg cm^{-2}, (c) 34 μm, 0.50 mg cm^{-2}, (d) 27 μm, 0.27 mg cm^{-2}, and (e) 25 μm, 0.11 mg cm^{-2}. (f) is the high magnification SEM image of the selected area in (e).

4.5 Conclusions

We investigated the cracking behavior of Si composite electrodes using *in situ* and *ex situ* techniques. Channel cracks form in Si electrodes made with SA, Na-CMC, and Nafion during the 1st delithiation because the strong adhesion of these binders with Si enables the contraction of composite electrodes and causes large localized tensile stresses. Cracks periodically open and close at the same locations as Si particles contract and expand repeatedly during cycling. In contrast, no cracks form in Si/PVDF electrodes since the weak adhesion between PVDF and Si particles is unable to generate localized tensile stress large enough to trigger cracks. The influence of binders on the cracking behavior of Si composite electrodes originates from their distinct adhesion strength with Si and mechanical properties, which determine the localized tensile stresses and mechanical

properties of electrodes. To fully understand the cracking behavior of Si composite electrodes, future work may focus on the effects of particle size, ratio of electrode components, external pressure, and electrolytes. Although there seems no clear relationship between binder-dependent performance and binder-dependent cracking behavior of Si composite electrodes, cracks lead to microstructure destruction and should be considered in designing Si composite electrodes. Based on the proposed cracking mechanism, we suggested three approaches, *i.e.*, reducing the electrode thickness, patterning the electrodes (below the critical island size), and using highly recoverable binders, to suppress cracking of Si composite electrodes during cycling.

CHAPTER 5. ELECTROCHEMICAL DEGRADATION OF SI COMPOSITE ELECTRODES AND A PARTIAL DELITHIATION STRATEGY

5.1 Summary

Our previous studies have shown that periodic cracking occurs in Si composite electrodes during cycling. The micro cracks and microstructure change may affect the electronic connectivity between Si particles and the matrix, thus causing the electrochemical degradation of Si composite electrodes. In this Chapter, electrochemical impedance spectroscopy (EIS) was used to study the evolution of lithiation/delithiaiton kinetics during lithiation and delithiation over long-term cycling. We found that the both SEI resistance (R_{SEI}) and charge transfer resistance (R_{ct}) increase during long-term cycling, indicating electrochemical degradation of Si composite electrodes. Electrodes at the lithiation state have slightly different R_{SEI} from the delithiation state, while R_{ct} at the delithiation state is significantly larger than that at the lithiation state during long-term cycling. The influence of the state of charge (SOC) on R_{ct} is correlated with the periodic cracking behavior, porosity, and electronic conductivity changes of Si composite electrodes within each cycle. Based on these findings, we proposed a partial delithiation approach to reduce R_{ct} and mitigate the electromechanical degradation of Si composite electrodes. Electrochemical measurements show that the partial delithiation protocol enables Si/SA composite electrodes to stabilize at 1200 mA g^{-1} (at C/3) for over 560 cycles, surpassing the partial lithiation protocol (1200 mA g^{-1}, C/3 for about 375 cycles).

5.2 Introduction

Fracture of Si particles and the consequent excessive SEI formation are caused by the large volume change ($\approx$300%) of Si during electrochemical cycling [13, 14, 26, 144]. It is known that the electrochemically induced pulverization is inevitable for Si microparticles [128, 145], while Si nanoparticles could maintain their mechanical integrity during lithiation/delithiation due to their high specific surface energy [13, 24]. Nevertheless, the repeatedly volume change of Si nanoparticle continuously leads to the mechanical degradation of Si composite electrodes, such as the periodic cracking and irreversible volume change on the electrode level, as shown in Chapter 2, 3, and 4. Recently, X-ray

tomography techniques have confirmed that structural degradation could change the spatial distribution of Si particles in the electrodes [26, 95, 146], reducing the electronic conductivity between Si particles and the conductive matrix, and, consequently, slowing down lithiation/delithaition kinetics of Si composite electrodes. Although the mechanical degradation is closely related to the electrochemical degradation, structural changes on the electrode level may not fully reveal the capacity fading of Si composite electrodes, which is evidenced by our recent finding that the cracked Si/SA and Si/Na-CMC electrodes have remarkably better electrochemical performance than the uncracked Si/PVDF electrodes. Therefore, the degradation and the poor cycling stability of Si composite electrodes need to be further understood from a systematic study of the evolution of lithiation/delithiation kinetics. In particular, finding out the controlling kinetics is crucial to develop strategies to improve the electrochemical performance of Si composite electrodes.

Electrochemical impedance spectroscopy (EIS) is a powerful technique to study the lithiation/delithiation kinetics of LIB electrodes [147-149]. The impedance caused by each kinetic step can be quantified from the EIS data using proper equivalent circuits. EIS has been extensively used to investigate the electrochemical activity, kinetics, and degradation of a wide range of electrode materials and electrodes for LIBs [150-152]. Previous EIS studies on Si-based electrodes focus on the impedance evolution at different SOCs within one cycle or during long-term cycling, very often, at the delithiation state [153-155]. Since the microstructure change substantially from the delithiation state to the lithiation state and vice verse, the degradation of lithiation/delithiation kinetics may also be influenced by SOCs. Correlating the degradation of kinetics with the structural change at different SOCs during long-term cycling is critical for understanding the governing degradation kinetic step as well as optimizing the cycling protocol to improve the stability of Si composite electrodes.

In this study, we conducted a comparative study of the evolution of EIS at both lithiation and delithiation states during long-term cycling. The evolution of impedances from SEI and charge transfer are quantified and compared. We established a correlation between impedance and mechanical degradation of Si composite electrodes. Based on

these findings, we proposed and experimentally confirmed a partial delithiation approach to improve the cycling stability of Si composite electrodes.

5.3 Experimental

The electrode preparation method can be found in the Experimental part in Chapter 2.

5.3.1 Electrochemical Impedance Spectroscopy (EIS) Measurements

CR 2025 half coin cells were assembled with Si/PVDF, Si/Na-CMC or Si/SA electrodes as the work electrode and Li metal as the counter electrode. The electrolyte is 1M $LiPF_6$ in ethylene carbonate and diethyl carbonate solution (EC: DEC = 1:1 wt%, Gotion) with 10 wt% fluoroethylene carbonate (FEC, Gotion) as the additive. Potentio EIS tests were conducted in cells after 2nd, 10th, 50th, and 100th delithiation and 3rd, 11th, 51th, and 101th lithiation using a Bio-Logic potentiostat. Before EIS tests, each cell was held at the lithiation (0.01 V) or delithiation (1.00 V) cutoff voltage until the current density decreased to a limit of C/400 $\mu A/cm^2$ and then rested for 6 hours. The frequency range of EIS measurements is from 10 mHz to 100 KHz.

5.3.2 Electrochemical Measurements

The partial delithiation cycling protocol was conducted by cycling the CR 2025 half cells at C/10 between 0.01 V and 1.00 V for the first 2 cycles, then fully lithiating the cell to 0.01 V at C/3 and partially delithiating the cells to a capacity limit of 1200 mAh g^{-1} at C/3 for the rest cycles. A partial lithiation cycling protocol was also used to cycle half cells for comparison. The partial lithiation cycling was conducted by cycling cells at C/10 between 0.01 V and 1.00 V for the first 2 cycles, then partially lithiating the cell to a capacity limit of 1200 mAh g^{-1} at C/3 and fully delithiating the cells to 1.00 V at C/3 for the rest cycles. The voltage-time profiles under both cycling protocols are shown in Figure 5.1.

5.3.3 X-ray Photoelectron Spectroscopy (XPS)

XPS (K-Alpha XPS System, Thermo Scientific) was used to study the surface chemistry of Si electrodes, including the as-made and cycled electrodes (after 2 cycles and

100 cycles). To avoid air exposure of cycled electrodes, a Vacuum Transfer Module (Thermo Scientific) was used to transfer the cycled electrodes from the glovebox to the XPS analysis chamber.

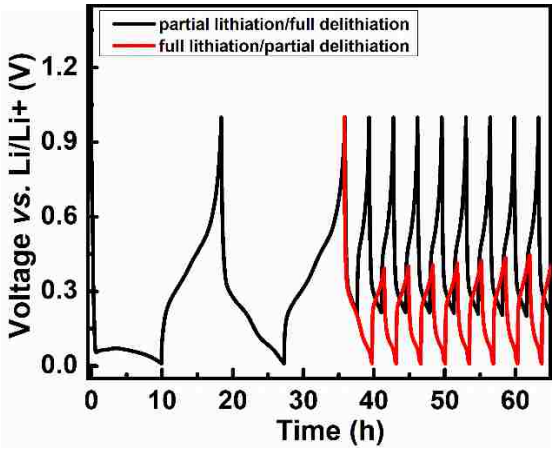

Figure 5.1 Voltage-time profiles of Si composite electrodes cycled under the partial delithiation and partial lithiation protocols.

5.4 Results and Discussion

The Nyquist plots of cells with Si/PVDF, Si/Na-CMC, and Si/SA electrodes at the lithiation and delithiation states after different cycle numbers are show in Figure 5.2. All the Nyquist plots consist of two depressed semicircles in the high and intermediate frequency regions, which can be attributed to the SEI and the charge transfer impedance [150], respectively. Based on this interpretation, an equivalent circuit is proposed for the Nyquist plots, as shown in Figure 5.3(a). The resistor, R_{ele}, is the ohmic resistance of the electrolyte. R_{SEI} in parallel with a constant phase element, Q_{SEI}, represent the SEI impedance, while R_{ct} and Q_{ct} represent charge transfer impedance. W_{s1} is the Warburg element for diffusion. The fitting results of R_{SEI} and R_{ct} are plotted against the cycle number in Figure 5.3(b) and (c). As shown in Figure 5.3(b), R_{SEI} of Si/PVDF is high over the first 50 cycles, while R_{SEI} of Si/Na-CMC and Si/SA electrodes increases gradually. For example, R_{SEI} of Si/Na-CMC at the full delithiation state increases from 18 Ω (the 2nd delithiation) to 116 Ω (the 100th delithiation).

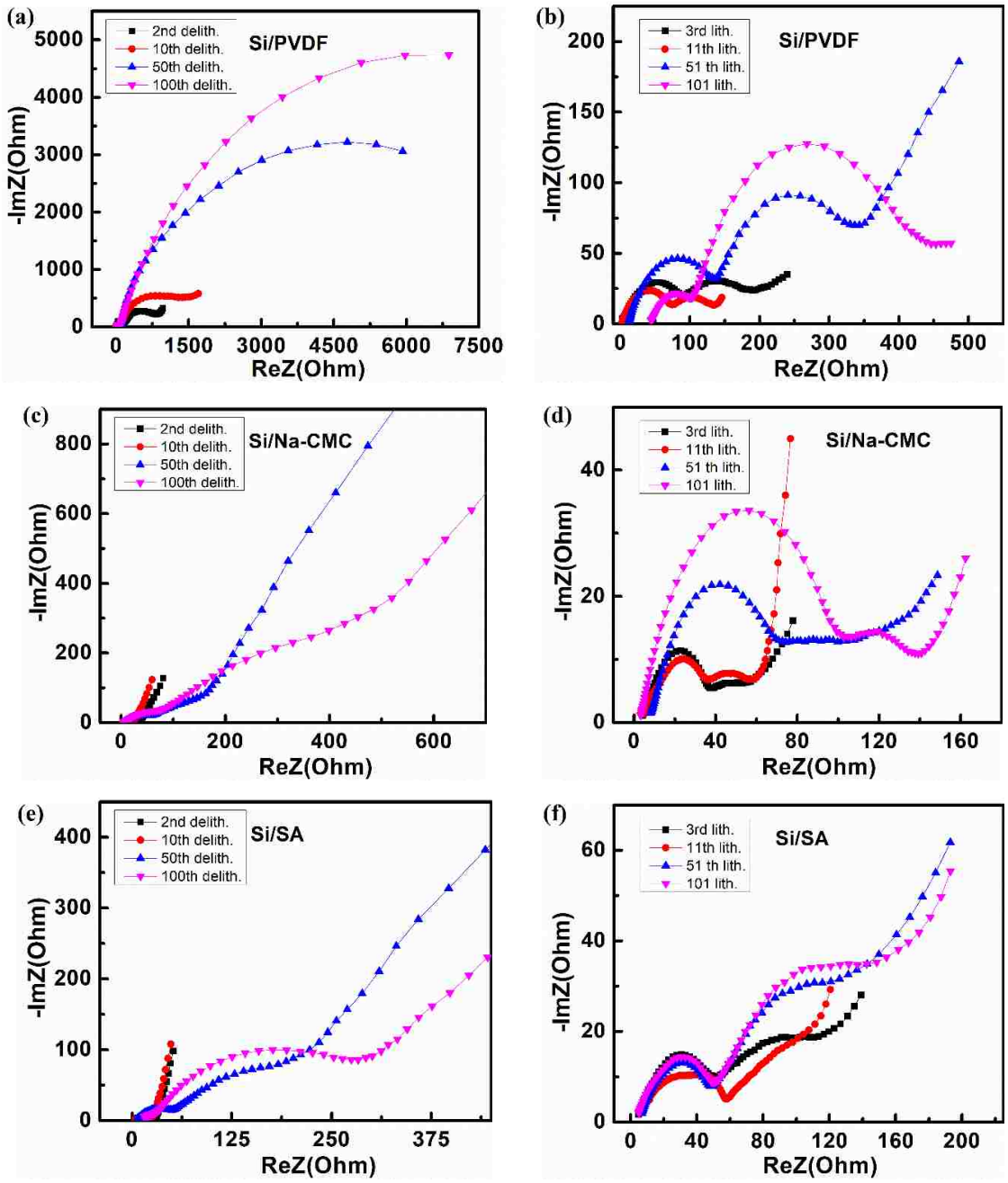

Figure 5.2 Electrochemical impedance spectroscopy of Si composite electrodes at the full lithiation and delithiation states during long-term cycling.

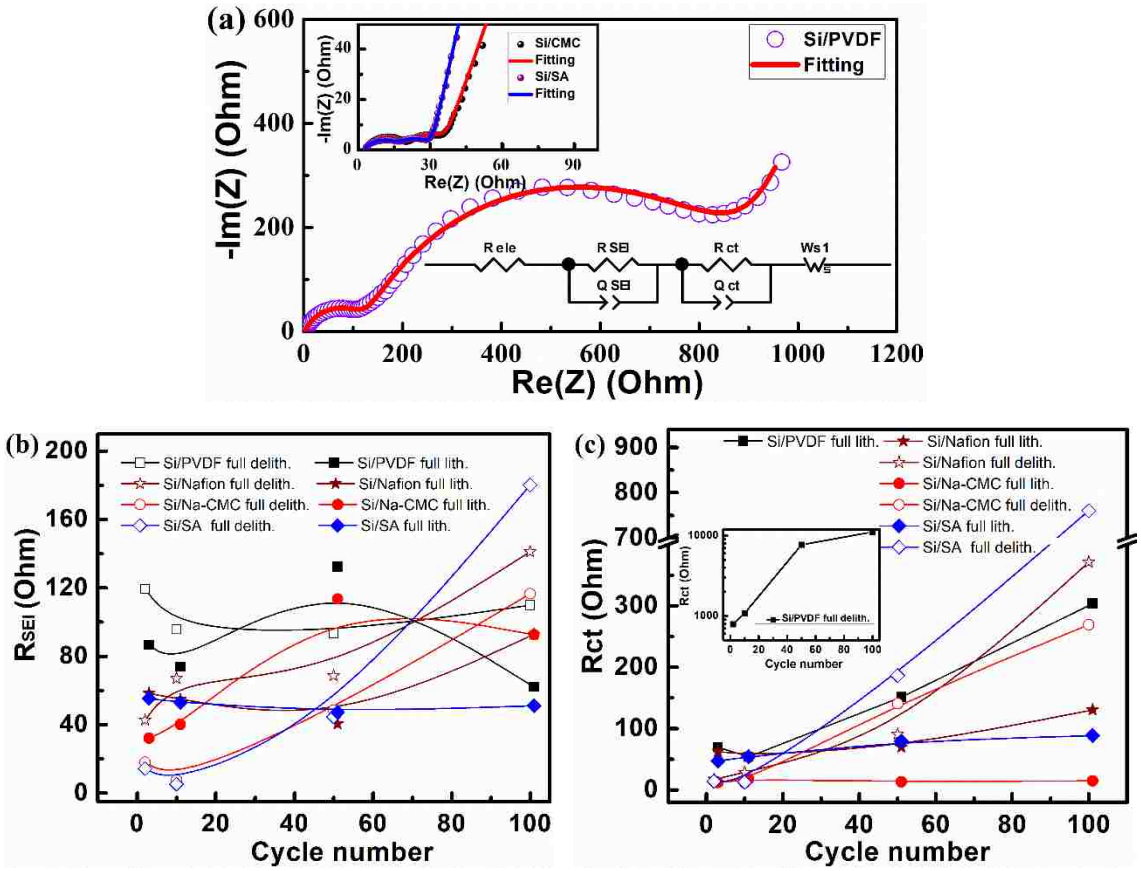

Figure 5.3 (a) A comparison of electrochemical impedance spectroscope of Si composite electrodes at the 2nd full delithiation state. Evolution of R_{SEI} (b) and R_{ct} (c) at the lithiation and delithiation states during long-term cycling.

R_{SEI} is closely related to the formation and growth of the SEI layer in electrodes. As seen from the XPS spectra in Figure 5.4, the SEI layer covered the Si surface after the 2nd cycle since all Si2p peaks disappeared. From the XPS spectra, the major SEI components of Si composite electrodes include Li_2O, LiF, Li_2CO_3, $Li_xPO_yF_z$, R-COOLi, and Li_xPF_y. Electrodes after 100 cycles have more $Li_xPO_yF_z$ compared with these after 2 cycles, as shown in Figure 5.4 (d). Our results suggest that binders in this study have little influence on the composition of the SEI layer, while several other studies showed that binders could influence the surface oxide of Si during the electrode preparation process (through pH and wettability), the reduction of carbonate solvent (EC), FEC and $LiPF_6$, the amount of SEI, and the ratio of SEI components [116, 156, 157]. The large R_{SEI} of Si/PVDF electrodes at 2nd lithiation and 3rd lithiation states is likely to be caused by the excessive formation of SEI during the formation cycles, which is evident from the low initial Coulombic

efficiency. The decrease of R_{SEI} of Si/PVDF electrodes after 100 cycles may result from the delamination of SEI from Li_xSi particles. The high initial Coulombic efficiency of Si/Na-CMC and Si/SA electrodes indicates that a relative small amount of SEI forms during formation cycles. As a result, Si/Na-CMC and Si/SA electrodes have low initial R_{SEI}. The increasing R_{SEI} of Si/Nafion, Si/Na-CMC, and SA electrodes during long-term cycling may be explained by the continuous formation of SEI.

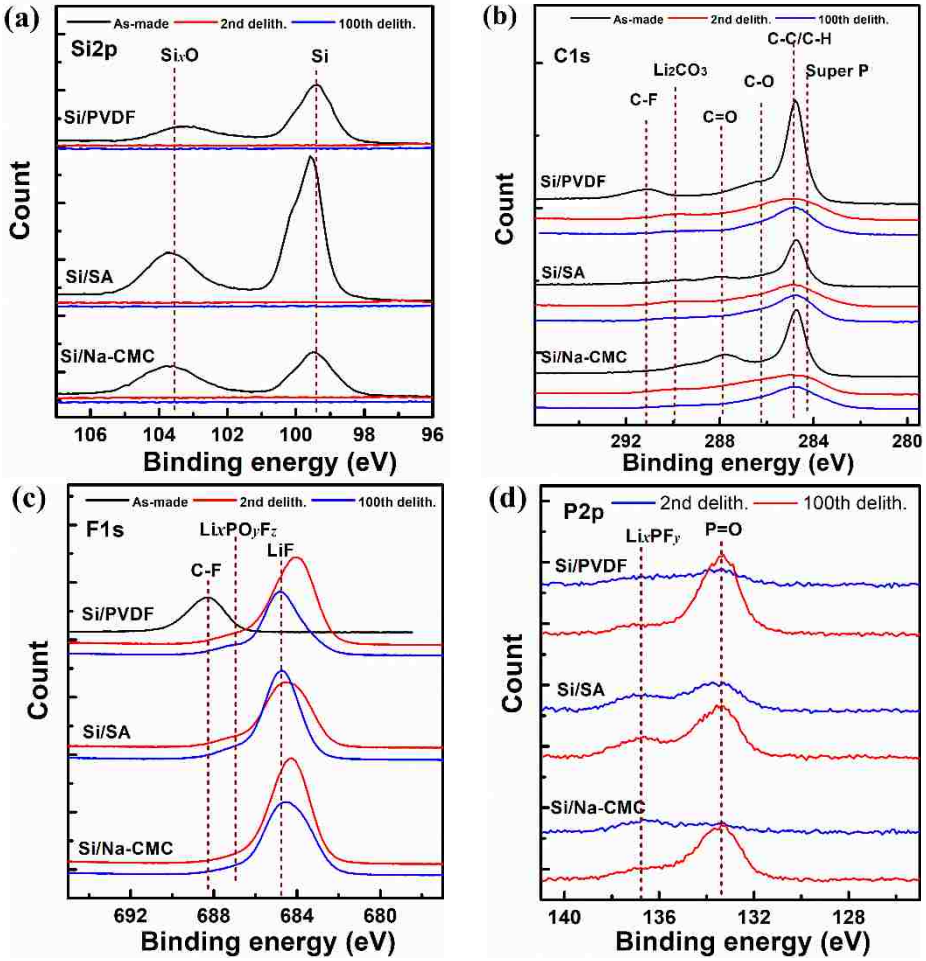

Figure 5.4 XPS spectra of Si composite electrodes: (a) Si 2p, (b) C 1s, (c) F1s, and (d) P 2p.

After the same number of cycles, R_{ct} of Si/PVDF electrodes at both lithiation and delithiation states is significantly higher than that of Si electrodes made with other binders, as shown in Figure 5.3(c). Based on our understanding of the microstructure, adhesion strength, and the SEI characterizations, the large R_{ct} at the delithiation state can be attributed to (1) the stress and repeated volume change of Si particles can damage the

electronic connectivity between Si particles and the PVDF/CB matrix considering the poor adhesion between Si and PVDF and (2) the excessive SEI and insulating side reaction products retard the electron transfer. The high R_{ct} and R_{SEI} account for the fast capacity fading of Si/PVDF electrodes.

As shown in Figure 5.3(c), R_{ct} of all composite Si electrodes at the full delithiation state increases with cycling. For example, R_{ct} of Si/Na-CMC electrodes increases from 14 Ω (after the 2nd delithiation) to 269 Ω after the 100th delithition. R_{ct} accounts for the lithiation/delithiation kinetics of active particles, which is influenced by the electronic contact between Si and the binder/CB matrix, electronic conductivity of the active materials, activity of the electrolyte, and ion transport in the electrodes. During cycling, the repeated volume change of Si particles and the accumulated SEI layer may weaken the adhesion between active particles and the binder/CB matrix. The accumulating irreversible volume change reduces the electronic conductivity between Si particles and the binder/CB matrix. Both factors increase the electronic resistance between Si particles and the matrix and, thus, $R_{ct.}$ Accumulated side reaction products and irreversible volume changes also increase the tortuosity and decrease the porosity of Si electrodes [158, 159]. As a result, the limited lithium ion transport rate also contributes to the increase of R_{ct}. Moreover, the decomposition of $LiPF_6$, FEC, and EC during long-term cycling reduces the activity of the electrolyte.

However, R_{ct} of Si/SA, Si/Na-CMC, and Si/Nafion electrodes at the lithiation state increases only slightly during long-term cycling. The microstructure difference between the lithiation and delithiation states include (1) the phase transformation between *a*-Si and *a*-Li_xSi; (2) the volume of Li_xSi particles at the lithiation state is larger than that of *a*-Si at the delithiation state; (3) channel cracks in electrodes close at the lithiation state but open at the delithiation state; (4) electrodes at the lithiation state have a lower porosity and is thicker than that at the delithiation state. Evidently, the expanded Li_xSi particles in the lithiation state have better physical contact and thus improve electronic connectivity with the matrix, while the low porous and thick electrodes at the lithiation state have inferior lithium ion transport property than that at the delithiation state. In addition, the SEI composition and the activity of the electrolyte between the lithiation and delithiation states

are not likely to change a lot in the same cycle. Therefore, it is the electronic conductivity, instead of the transport of lithium ions, and electrolyte activity, that lead to the increase of the charge transfer kinetics of Si/Na-CMC and SA electrodes, especially at the full delithiation state.

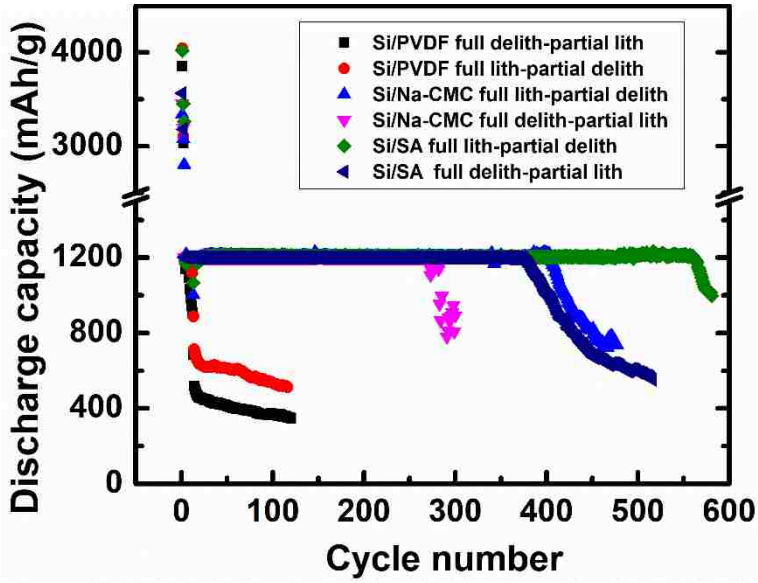

Figure 5.5. Discharging capacity-cycle number profiles of Si composite electrodes cycled under the partial delithiation and partial lithiation protocols.

Recently, several researchers proposed partial lithiation strategies to improve the cycling stability of Si thick film electrodes and Si composite electrodes. For example, Xu *et al*. [25] and Li *et al*.[160] showed that by controlling the lithiation capacity (but still fully charge the cell to the cutoff voltage of 1.0 V or 1.2 V) can improve the cycling stability of Si composite electrodes. Since the average R_{ct} of Si composite electrodes during cycling can be reduced by decreasing the degree of delithiation, as shown in this study, the degree of delithiation state should be restricted to improve the average electrochemical kinetics. Indeed, Verbrugge *et al.* [161] found that Si films cycled within a low cutoff voltage range (between 0.4093 V and 0.05 V) have significantly better efficiency retention than those cycled at a higher voltage range (between 1.2 V and 0.2317 V). Hence, we propose a partial delithiation approach, that is, fully lithiating the Si electrodes to the cutoff voltage of 0.01V but partially delithiating to 1200 mAh g^{-1} (at C/3) in each cycle, to improve the cycle stability of Si composite electrodes. A partial lithiation protocol, that is, partially lithiating

the Si electrodes to 1200 mAh g^{-1} (at C/3) and fully charging to the cutoff voltage of 1.00 V in each cycle, is also used to cycle the electrodes for comparison. Figure 5.5 shows the discharging capacity-cycle number profiles of Si/PVDF, Si/Na-CMC, and Si/SA electrodes under the partial delithiation and partial lithiation protocols. All three electrodes cycled under the partial delithiation protocol can be stabilized at 1200 mAh g^{-1} for more cycles than that cycled under the partial lithiation protocol. For example, the Si/SA electrode maintains a discharging capacity of 1200 mAh g^{-1} for 560 cycles under the partial delithiation protocol, while it can maintain a discharging capacity of 1200 mAh g^{-1} for 375 cycles under the partial lithiation protocol. The improved cycling stability by the partial delithiation protocol can be attributed to reduced average R_{ct} and the enhanced electronic connections between Li_xSi particles with the matrix, both of which are rendered by the increased physical contract between the expanded particles and the dense matrix. In contrast, the average expansion of Si particles is small under the partial lithiation protocol. As a result, the matrix is highly porous and small *a*-Si particles are likely to detach from the matrix and become electronically isolated, which leads to a large R_{ct} and an inferior cycling stability. We believe that this partial delithiation strategy can also be adopted to improve the cycling stability of other negative composite electrodes.

5.5 Conclusions

We investigated the electrochemical degradation of Si composite electrodes by the evolution of lithiation/delithiation kinetics at the lithiation and delithiation states during long-term cycling. R_{SEI} and R_{ct} of Si composite electrodes at lithiation state increases during long-term cycling. A small difference exists in R_{SEI} between the lithiation and delithiation states, while R_{ct} at the delithiation state is significantly higher than that at the lithiation state after 50 cycles, probably because of expanded Li_xSi particles at the lithiation state have improved electronic connection with the conductive matrix. Based on the SOC-dependent R_{ct}, porosity, and cracking behavior of Si composite electrodes, we proposed a partial delithiation cycling protocol to improve the mechanical integrity as well as the cycling stability of Si composite electrodes. Electrochemical measurements showed that this partial delithiation approach can well mitigate the electromechanical degradation and effectively

extend the cycling life of Si composite electrodes compared with the partial lithiation cycling protocol.

CHAPTER 6. MECHANICAL BEHAVIOR OF BULK LITHIUM METAL STUDIED BY NANOINDENTATION[4]

6.1 Summary

Applying mechanical stresses is a possible approach to suppress dendrite and mossy lithium (Li) in Li metal electrodes. We conducted, in this work, nanoindentation tests on pure Li metal in an argon-filled glove box to study its viscoplastic behavior at room temperature. Both load-controlled and strain rate-controlled nanoindentations showed clear viscoplastic characteristics of Li. Based on an iterative finite element (FE) modeling approach, we determined a viscoplastic constitutive law for Li. In addition, we demonstrated by FE modeling that the elastic modulus, on the order of GPas, has a negligible influence on the nanoindentation response of Li at ambient temperature.

6.2 Introduction

With its high theoretical specific capacity (3862 mAh g^{-1}), lowest negative reduction potential (-3.04 V *vs*. the standard hydrogen electrode) and low density, Li metal has been considered a desirable negative electrode material; thus triggered worldwide interest in the rechargeable Li metal-based batteries, such as Li-O_2 and Li-S batteries [162, 163]. However, uncontrollable Li dendrites could penetrate through the separator, leading to short-circuit of batteries. Mechanical suppression through polymer or solid state electrolytes (SSE) [46, 164] and artificial stiffer solid electrolyte interphase (SEI) [165] has been proposed as an economical and promising solution for this problem. Based on the elastic deformation assumption, the theoretical work by Monroe *et al*. [46] indicated that SSE with a shear modulus twice of Li could inhibit Li dendrites. However, since the yield strength of Li is low, the stress generated at the separator/Li interface could cause plastic deformation of Li at a yield strength fraction of the modulus value [166, 167]. Continued plastic deformation during repeated charging/discharging may cause Li redistribution, leading to shape change of Li at the anode/separator interface, and hence posing a threat to

[4] Reproduced from *Wang, Yikai, and Yang-Tse Cheng. "A nanoindentation study of the viscoplastic behavior of pure lithium." Scripta Materialia 130 (2017): 191-195.*

the safety and stability of Li metal batteries [167, 168]. A comprehensive understanding of the mechanical properties, especially the plastic flow behavior, of Li is necessary.

The mechanical test of Li metal is challenging because Li is extremely reactive with oxygen, nitrogen, water vapor, and carbon dioxide. Sample preparation and mechanical tests must be conducted in a protective environment. However, the few early reported tensile [169], compression [170], and resonance tests [171] were not carried out in a protective atmosphere. Thus, it is unsurprising that the reported elastic modulus (E) ranges from 1.84 to 7.8 GPa, and the yield strength from from 0.48 to 1.10 MPa [169-171]. Similar to other soft metals and alloys, such as Sn-alloys [172, 173], indium [174], and lead [175], the deformation behavior of Li exhibits low yield strength and viscoplasticity. Because of the importance of viscoplastic behavior, we report, in this chapter, nanoindentation measurements of Li performed in an argon-fill glove box. Combining FE modeling with nanoindentation measurements, we determined a constitutive law for viscoplastic deformation of bulk Li during indentation loading. The influence of E on the viscoplastic deformation of Li metal was also studied.

6.3 Experimental

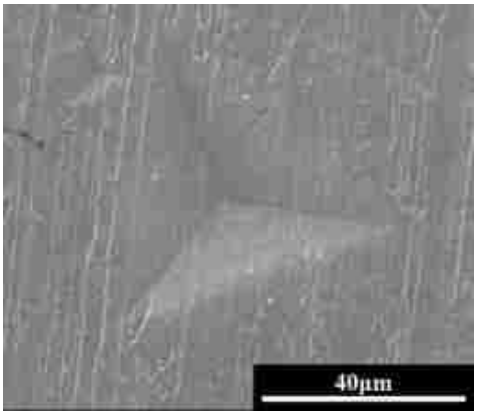

Figure 6.1 A typical SEM image of an indent in the Li foil.

High purity polycrystalline Li foils (99.9%, with thickness of 750 μm, Alfa Aesar) were used for nanoindentation measurements. Nanoindentation tests were conducted using the Nanoindenter G200 (Agilent) inside an argon-filled glove box (both oxygen and moisture < 0.1 ppm, MBRAUN) at 2.1 mbar, as shown in Figure 2.2(a). Load-controlled tests were carried out using a diamond Berkovich indenter (tip radius 200 nm) with loading

rates, $\dot{F}$, ranging from 0.196 to 3.92 mN/s to the maximum load, F, of 5.88 mN. The holding periods were set to be 1s. Constant strain rate-controlled tests were conducted with constant $\dot{F}/F$ values ranging from 0.1 to 1.0 s^{-1}. After nanoindentation measurements, the indents were examined by scanning electron microscope (SEM, FEI Quanta 250). A typical indent is shown in Figure 6.1. Since the maximum depth in each test was larger than 4500 nm, reproducible nanoindentation data were obtained despite of the slight surface roughness.

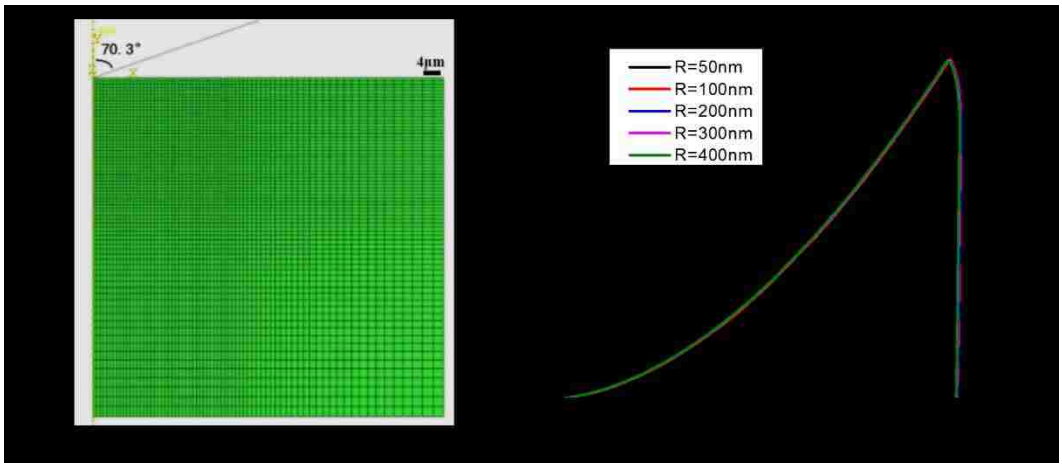

Figure 6.2 (a) The FE model for nanoindentation and (b) the influence of tip radius on the L-D curves obtained from FE modeling. The L-D curves with tip radius in the range between 50 and 400 nm overlap with each other.

6.4 Finite Element (FE) Modeling

FE modeling was conducted by using the commercial software ABAQUS. As illustrated in Figure 6.2(a), an axisymmetric isotropic model with 26244 elements was used with the mesh size finer around the contact area and gradually coarser away from the indent. The Berkovich indenter was represented by a rigid cone with a half apex angle of 70.3° because this conical indenter has the same depth-contact area relationship as the Berkovich indenter [176]. The tip radius was set to be 200 nm, which is the same as the tip radius of the Berkovich indenter in experiments. FEM modeling results show that the tip radius has negligible on the indentation load-displacement (L-D) curves, as shown in Figure 6.2(b). The friction coefficient between the indenter and Li foil was set to be 0.1, which is a typical value for nanoindentation analysis [177].The independent parameters in

the FE modeling are the loading rate and the maximum load, both of which were set to be the same values as those in the indentation measurements. For FEM input, the elastic modulus was assumed to be 3.5 GPa (in the reported range of 1.84 to 7.8 GPa) and Poisson's ratio was taken as 0.3. Later in this Chapter, we show that E, on the order of GPas, and Poisson's ratio, in a reasonable range between 0.05 and 0.45, have little influence on the load-displacement curves.

6.5 Results and Discussion

As shown in Figure 6.3(a) and (b), the L-D curves of Li exhibit obvious rate-dependent characteristics, *i.e.*, the higher the loading rates, $\dot{F}$, the larger the load, F, is needed to reach the same indentation depth. For constant strain rate-controlled nanoindentation tests, the load corresponding to the same depth increases with the value of $\dot{F}/F$. The creep penetration depth during the holding period increases with increasing loading rate. Similar to viscoelastic materials [178], "noses" appeared at the initial part of the unloading curves. The elastic recovery during the unloading is only few tens of nanometers. Therefore, the indentation deformation is mainly plastic. In the following analysis, we focus on the loading part as our interest is the constitutive law of viscoplasticity.

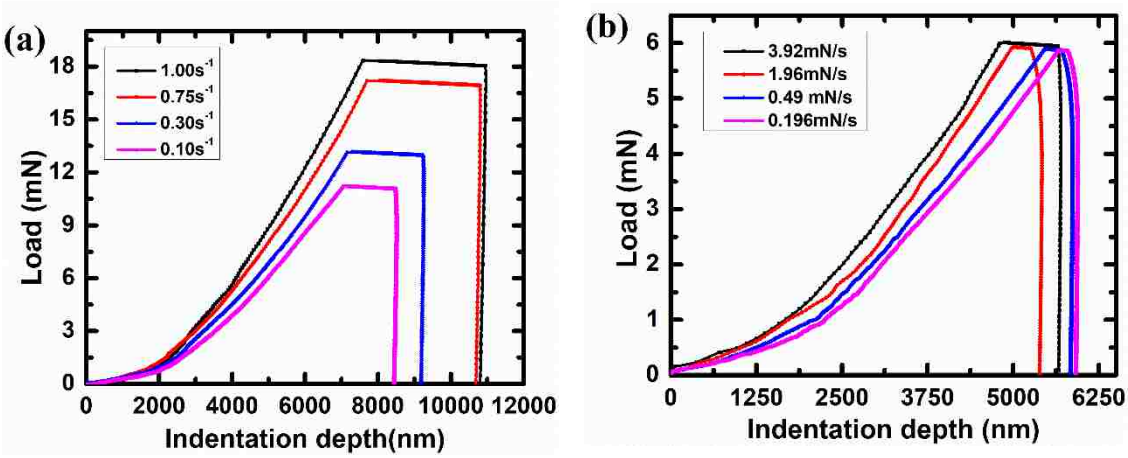

Figure 6.3 (a) Typical L-D curves with different values of $\dot{F}/F$ and (b) typical L-D curves with different loading rates (dF/dt).

The rate-dependent plasticity, or viscoplasticity, of Li during the indentation loading may originate from two mechanisms. First, the thermally activated diffusion and

viscous flow [179], such as Nabarro-Herring creep, Coble creep and dislocation climb, are expected to occur since the homologous temperature, T_{rm}/T_{melt}, is 0.66 at room temperature for Li. Second, the stable crystal structure of Li is body centered cubic (BCC) at room temperature [180]. The plastic deformation of BCC metals and alloys is governed by the motion of screw dislocations via kink pairs, which require thermal activation [179, 180]. Therefore, the viscoplasticity of Li is likely the result of those multiple physical mechanisms. Although a mechanism-based model would have been more reliable in describing the viscoplastic behavior of Li, such a model would require detailed information at the atomic scale (*e.g.*, dislocation structure and diffusion coefficient) that is generally unavailable. Instead, several empirical or phenomenological constitutive models, such as Anand model [181], Johnson-Cook model [182], and Perzyna model [183, 184], have been developed based on different assumptions to describe viscoplastic deformation of soft metals and alloys [173, 174, 185]. Anand model does not have an explicit yield condition or loading/unloading criterion, such that plastic strain can take place under any nonzero stress. This model is preferred for the steady-state creep under constant load or stress [173, 174]. Johnson-Cook model has been widely used for various materials over a wide range of temperature and strain rates, especially for high strain rate deformation. But our preliminary trial found that consistent parameters could not be obtained for Li with Johnson-Cook model. The one-dimension Perzyna model and Cowper-Symonds model [186] have the equivalent functional form. Cowper-Symonds model was derived for high rate impact tests of cantilever beams, and thus suitable for high strain rate deformation; while Perzyna model was derived for general elastic-viscoplastic solids under general stress states [183, 184]. It has a yield surface with a strain rate-hardening mechanism activated only after yielding. Perzyna model has been successfully used to describe the rate-dependent flow behavior of many soft metallic materials (such as Sn-based solder alloys [185, 187]). Considering both the elasticity and viscoplasticity, we assume Li as a Perzyna elastic-viscoplastic solid with work hardening. The flow stress after yielding follows a constitutive law in the form of,

$$\sigma_f = k\varepsilon_p^n[1 + (\frac{\dot{\varepsilon}_p}{\gamma})^m] \tag{6.1}$$

where σ_f is the flow stress, k is the strength coefficient, ε_p is the plastic strain, n is the work hardening exponent, $\dot{\varepsilon}_p$ is the plastic strain rate, γ is the material viscosity parameter, and m is the stain rate sensitivity. This overstress constitutive law was assumed for the indentation loading part. It is not likely to be applicable to the holding and unloading parts because the deformation mechanisms of overstress yielding and creep (under static stress) may be different [188, 189].

There exists a representative strain, ε_r (physically uniaxial or equi-biaxial plastic strain [190, 191]), for self-similar Berkovich indenter [177, 190-192]. For power law work hardening materials, ε_r only relates to the half apex angle (α) of the indenter ($\alpha = 70.3°$ for Berkovich indenter), and does not depend on the work hardening exponent [177, 190-192]. If the rate-dependent part of Eq. (5.1) is treated as a constant (i.e., constant strain-rate indentation tests), the constitutive law can be rewritten as the power law work hardening for a representative strain (ε_r) of nanoindentation. A representative stress is then given by,

$$\sigma_r = k\varepsilon_r^n \tag{6.2}$$

Then, Eq. (5.1) is readily reduced to the power law creep model as,

$$\sigma_{ef} = \sigma_f - \sigma_r = \sigma_r(\frac{\dot{\varepsilon}_p}{\gamma})^m \tag{6.3}$$

where σ_{ef} is here defined as the effective flow stress. There is an effective indentation strain rate, $\dot{\varepsilon}_{ef}$, for power-law creep materials [193, 194],

$$\dot{\varepsilon}_{ef} = 0.12\frac{\dot{h}}{h} \tag{6.4}$$

where $\dot{h}$ is the penetration rate, h is the indentation depth. Since the nanoindentation deformation of Li is mainly plastic, $\dot{\varepsilon}_p$ is assumed to be the same as $\dot{\varepsilon}_{ef}$. From the dimensional analysis [58], the flow stress during the nanoindentation by an ideally sharp self-similar cone indenter is proportional to the ratio of the indentation load to the square of indentation depth,

$$\sigma_f = C\frac{F}{h^2} \tag{6.5}$$

where C is a constant for a given indenter geometry and a material subject to the indentation test (*i.e.*, Li in the present case). Under the above assumptions, Eq. (6.1) can be rewritten as,

$$\frac{F}{h^2} = \frac{k\varepsilon_p^n}{C}[1 + (\frac{\dot{\varepsilon}_{ef}}{\gamma})^m] \quad (6.6)$$

Both γ and m can be obtained from the $F/h^2\ vs.\ \dot{\varepsilon}_{ef}$ curves. Constant effective strain rate $\dot{F}/F$ nanoindentation result was obtained only after 3500 nm, as shown in Figure 6.4(a). Three sets of $F/h^2\ vs.\ \dot{\varepsilon}_{ef}$ corresponding to 4000, 5000, and 6000 nm were extracted. Both averaged F/h^2 and $\dot{\varepsilon}_{ef}$ were used here, as indicated by the error bars in Figure 6.4(b). Fitted with Eq. (6.6), the obtained values of γ and m are quite consistent, as shown in Figure 6.4 (b) and Table 6.1. The average values of γ and m are taken for the constitutive law.

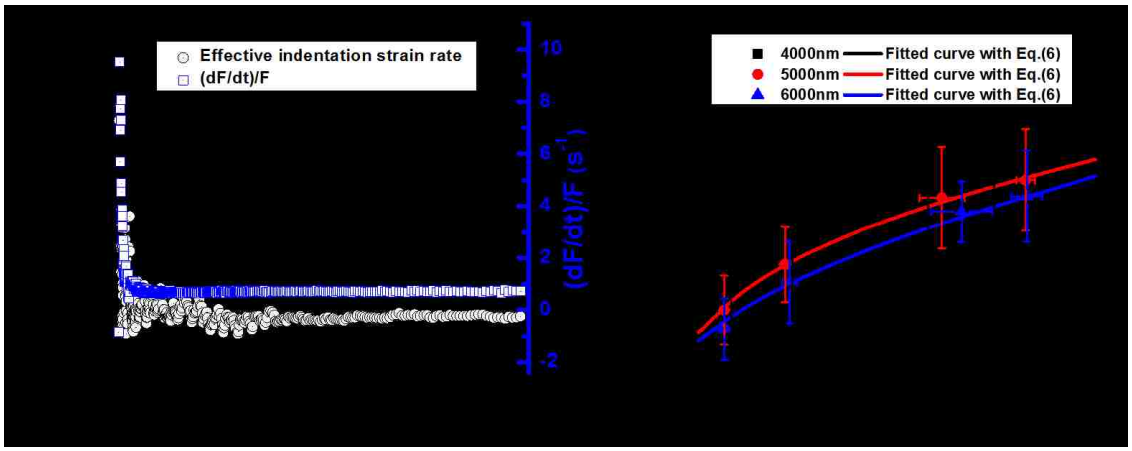

Figure 6.4 The variation of the effective indentation strain rate$(0.12\,\dot{h}/h)$ and $\dot{F}/F$ with indentation depth ($\dot{F}/F$ is $0.75s^{-1}$ in the experiment). Prior to 3500 nm, the distribution of strain rate is scattering. The effective strain rate trends to be a constant value only after 3500 nm. (b) The $F/h^2\ vs.\ \dot{\varepsilon}_{ef}$ relationship corresponding to different indentation depths. The average values of F/h^2 and the effective strain rate $(0.12\,\dot{h}/h)$ were used here.

Table 6.1 Fitting results of the $F/h^2\ vs.\ \dot{\varepsilon}_{ef}$ curves with Eq. (6.6).

Depth(nm)	Fitting results			
	$k\varepsilon_p^n/C$	γ	m	R^2
4000	249.98	0.31	0.59	0.96
5000	220.76	0.29	0.42	1.00
6000	233.87	0.30	0.60	0.99
Average value		0.30	0.54	

FE modeling was conducted to determine *k* and *n*. Since the effective strain rate before 3500 nm indentation depth is scattered to some extent, as shown in Figure 6.4(a),

FE modeling was conducted with load-controlled mode. As shown in Figure 6.5(a) and (b), the indentation load increases with increasing *k* and *n*. A larger *k* means higher flow stress, leading to larger indentation loads. The parameter *n* (usually *n*<1) reflects the non-linearity of flow stress.

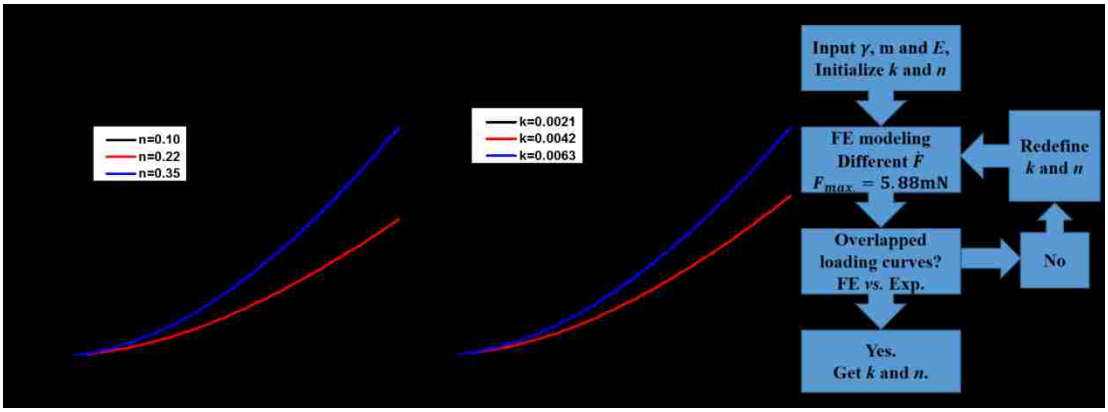

Figure 6.5 The effect of *n* (a) and *k* (b) on the loading curves from FE modeling; and (c) the flow chart for determining *k* and *n* using an iterative FE modeling.

To determine *k* and *n*, an iterative FEM procedure, shown in Figure 6.5 (c), was performed. The main idea is to iteratively compare the L-D curves from FEM and experimental, then refine the values of *k* and *n* until satisfactory match between the two was achieved. The averaged experimental L-D curves are used for this comparison. With this iterative method, *k* and *n* are determined to be 0.0042 and 0.23, respectively. Figure 6.6(a) and (b) show the good agreement between the averaged experimental L-D curves and FEM L-D curves with different loading rates. Therefore, it is reasonable to conclude that the viscoplastic behavior of Li can be described by the following constitutive equation,

$$\sigma_f = 0.0042{\varepsilon_p}^{0.23}[1 + (\frac{\dot{\varepsilon}_p}{0.30})^{0.54}] \quad (6.7)$$

Cheng and Cheng [61] showed that multiple stress-strain relationships of power law work hardening materials could lead to nearly identical L-D curves. In this study, the iterative FEM approach with 4 different loading rates would reduce the choices of *k* and *n*. Although the uniqueness of *k* and *n* is not proven mathematically, alternative sets of *k* and *n* were not found by our iterative FEM approach.

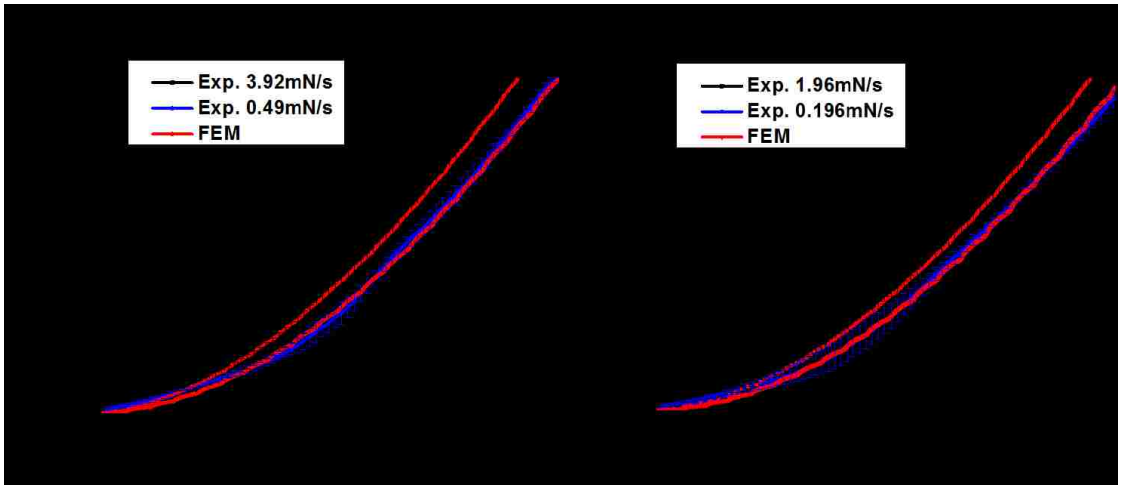

Figure 6.6 Comparisons of averaged experimental loading curves with FE modeling results with different loading rates. (a) 3.92mN/s and 0.49mN/s; and (b) 1.96mN/s and 0.196mN/s.

In the above FEM analysis, E=3.5 GPa was assumed. The reported value of E ranges from 1.84 to 7.8 GPa [169-171, 195]. While one might expect a clear influence of E on the viscoplastic deformation behavior, our FE result shows that E within this range has a negligible influence on the indentation response, as shown in Figure 6.7(a). This can be explained by the very low yield strength (σ_y) of Li. For the continuity of the constitutive law, $\sigma_y = \sqrt[1//(1-n)]{k/E^n} \approx 0.56$ MPa for static deformation. The ratio of σ_y/E is about 1.6×10^{-4}, which is on the same order of magnitude as indium (0.8×10^{-4}) [196], tin (2.4×10^{-4}) [197, 198] and many tin-based solder alloys [199]. Since the homologous temperature, $T_{rm}/T_{melt} = 0.66$, of Li is relative high at room temperature, the thermal diffusion activated creep would make significant contributions to the total deformation [179]. As a result, the elastic deformation is much less than the viscoplastic deformation. The variation of elastic modulus on the order of GPas only causes relatively small change of the overall deformation. In addition, by assuming Poisson's ratio in a reasonable range from 0.05 to 0.45 in FE modeling, the load-displacement curves exhibit little influence of the Poisson's ratio value on the indentation response, see Figure 6.7(b). Therefore, the elastic deformation may not be as important as the viscoplastic deformation of Li in the mechanical design of Li metal electrodes.

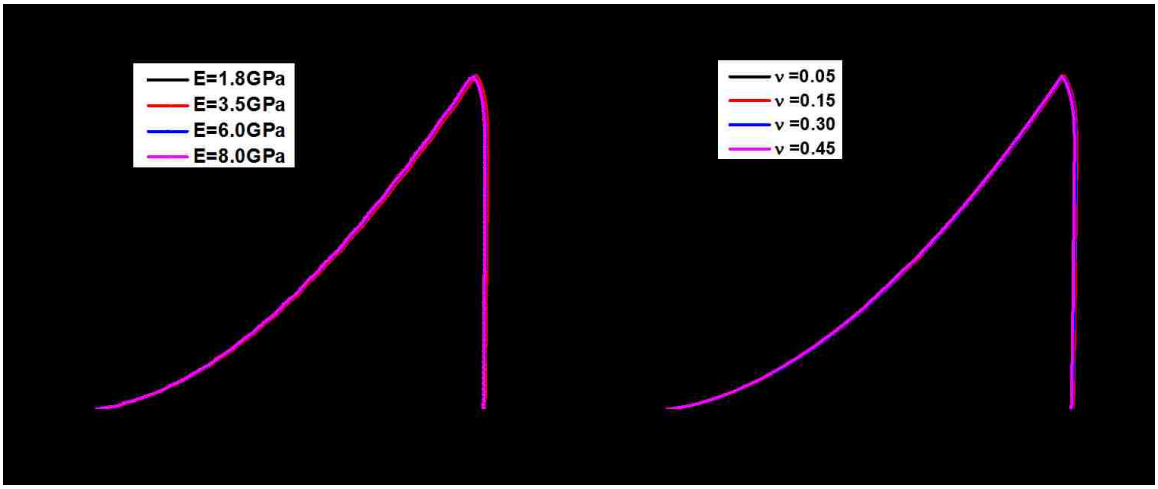

Figure 6.7 The effect of the elastic modulus (a) and Poisson's ratio (b) on the L-D curves. The L-D curves with $E \geq 3.5$ GPa almost overlap with each other.

6.6 Conclusions

The nanoindentation response of Li metal is dominated by viscoplastic deformation at room temperature. Combining nanoindentation measurements with an iterative FE modeling approach, we determined a constitutive law for the viscoplasticity of Li during nanoindentation. The FE modeling results show that the elastic modulus (on the order of GPas) and Poisson's ratio (in the range from 0.05 to 0.45) have a negligible influence on the indentation response of Li. Attention should therefore be paid to the viscoplastic deformation rather than the elastic deformation in designing Li metal electrodes operating at or near room temperature. The method used in this study to determine the viscoplastic constitutive law may also be applied to other viscoplastic metallic electrodes, such as sodium (Na) and potassium (K) metal electrodes.

CHAPTER 7. A COMPARATIVE STUDY OF THE MECHANICAL BEHAVIOR OF BULK AND POROUS MOSSY LITHIUM

7.1 Summary

Li dendrites, excessively grown by consuming the organic electrolyte, can penetrate through the separator and pose safety hazards, is a major obstacle for the application of Li metal electrodes in liquid electrolyte-based batteries. Despite intensive efforts on developing new electrolytes and artificial SEIs to mitigate or even eliminate the dendrite growth, significant roughening of the Li surface and the uncontrollable formation of mossy Li still occur after a number of lithium plating and stripping cycles (usually a few hundreds). Recently, mechanical suppression, by applying proper external pressure, ceramic coated separators, and surface coatings, is emerging as an effective approach to improve the cycling stability of Li electrodes (even with mossy Li) in liquid electrolyte-based batteries. To develop a better mechanical suppression method, it is indispensable to gain a better understanding of the electrochemical-mechanical interactions at the Li | inhibitor interface based on the mechanical properties of bulk Li as well as mossy Li. Although mechanical properties of bulk Li have been quantified by several groups, little is known about the mechanical behavior of porous mossy Li. In this study, we performed nanoindentation measurements on electroplated mossy Li using a flat punch indenter in an environmental nanoindentation system installed in a glovebox. Surprisingly, mossy Li deforms and creeps far less than bulk Li under the same pressure. We propose several possibile mechanisms to understand the significantly high resistance to indentation deformation and creep of mossy Li. The measured mechanical properties of mossy Li are useful parameters for electrochemical-mechanical modeling and designing mechanical inhibitors to improve the cycle stability of Li metal electrodes in liquid electrolyte-based batteries.

7.2 Introduction

Lithium metal has been considered a high capacity negative electrode material to replace the conventional graphite electrodes for next generation batteries (LIBs and beyond) due to its high theoretical capacity (3862 mA g^{-1}). The application of Li metal electrodes has been impeded by the excessive formation of Li dendrites during electrochemical

cycling [34, 36, 41]. In liquid electrolyte-based batteries[5], the continuous formation of Li dendrites is accompanied with the formation of SEI and consumption of electrolytes. In addition, the loose microstructure of mossy Li can hardly maintain electronic conductivity, become inactive, and decrease the Coulombic efficiency [34]. Of equal importance, Li dendrites may penetrate through porous separators and cause short-circuit of batteries, which generates massive heat, may ignite flammable electrolyte solvents, and cause safety hazards. Numerous attempts have been made to develop new electrolytes (both solid and liquid formats) and additives to mitigate or eliminate the formation of Li dendrites. However, Li dendrites and mossy Li inevitably form in Li electrodes after extended cycle life (usually hundreds of cycles) [200, 201]. Recent research found that the cycling stability of Li electrodes (even with mossy Li) can be significantly improved by mechanical suppression, such as applying proper external pressure [202, 203], stiff separator [204], artificial SEIs [205, 206], and functional coatings [207]. Rational design of mechanical suppression requires fundamental understanding of the electrochemical-mechanical interactions of the interface between bulk Li, mossy Li, and inhibitors (separators or coatings), for which the mechanical properties of bulk and mossy Li are required.

Early efforts in mechanical property measurements of Li focused on the elasticity and yielding strength of bulk Li [169-171]. Recently, several groups enriched the understanding of the mechanical behavior of bulk Li, including viscoplasticity [60, 208], creep [195, 209], and the size effect [210]. These studies provide valuable mechanical parameters for modeling the interface interactions associated with bulk Li. However, the mechanical behavior of mossy Li is unknown for analyzing the interface of bulk Li | mossy Li | inhibitors and the deformation of mossy Li under external pressure.

To fill the knowledge gap of the mechanical behavior of mossy Li, we conduct, in this study, flat punch indentation measurements of mossy Li using an environmental nanoindentation system inside an argon-filled glovebox. Mossy Li with various morphology and porosity were obtained by electroplating using different current densities. Our flat punch, with an equivalent diameter of 41.62 μm, can deform a large area ($\approx$1360 μm^2) of mossy Li and thus measure the average mechanical behavior of mossy Li. Flat

[5] This study focuses on mossy Li formed in liquid electrolyte-based batteries since the microstructure and surface chemistry of Li dendrites in solid state batteries are different.

punch indentation measurements are also conducted in bulk Li for comparison. The influence of SEI, morphology, and porosity on the mechanical behavior of mossy Li is discussed.

7.3 Experimental

7.3.1 Electrochemical Method

Mossy Li samples with different microstructures were prepared by electroplating of Li | Li symmetric cells using different current densities, i.e., 0.25, 1.00, 4.00, and 10.00 mA cm^{-2}. To avoid damage to mossy Li during the cell disassembling process, a Swagelok cell (Figure 2.1(a)) was used for the electroplating. The external pressure of the Swagelok cells is controlled be about 0.113 ± 0.05 MPa. The areal capacity of electroplating is 40 mAh cm^{-2} which renders the thickness of mossy Li larger than 200 μm cm^{-2}. Since the maximum depth of our indentation measurements is smaller than 1/10 of the thickness of mossy Li, the substrate effect will not influence the indentation results. The electrolyte is 1M $LiPF_6$ in EC:DEC = 1:1 wt% with 10 wt% FEC (Gotion).

7.3.2 Microstructure Characterizations

The surface and the cross-sectional microstructure of mossy Li were characterized by a field emission scanning electron microscope (SEM, FEI Quanta 250). The cross sections of moss Li were prepared by pulling the mossy Li layer apart using a tweezer and observed by SEM. XPS (K-Alpha XPS System, Thermo Scientific) was used to study the surface chemistry of mossy Li.

7.3.3 Flat Punch Indentation Measurements

Flat punch indentation measurements were conducted using our environmental nanoindentation system (G200, Keysight) inside an argon-filled glovebox. The cross sectional area of the flat punch is about ≈ 1360 μm^2. The maximum indentation load ranges from 6.86 mN to 19.8 mN. The loading/unloading rate is 0.0196 mN/s. A 600 s holding period was conducted at the maximum load to monitor the creep behavior of mossy Li. As a comparative study, flat punch indentation measurements with the maximum load ranging from 5.39 mN to 8.82 mN were conducted in bulk Li (99.9%, thickness 750 μm, Alfa

Aesar). The loading/unloading rate and the holding period of flat punch indentation measurements in bulk Li are the same with mossy Li.

7.4 Results and Discussion

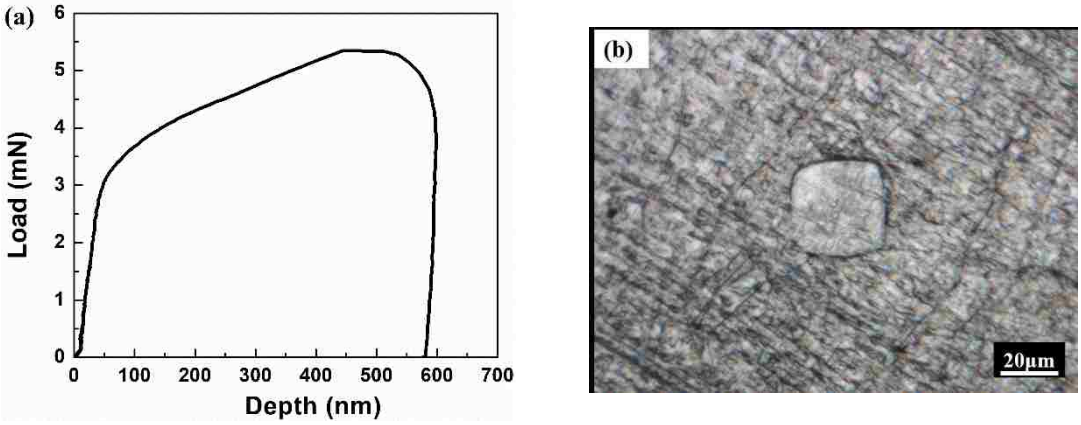

Figure 7.1 (a) Load-displacement curves of a flat punch indentation measurement in bulk Li using depth-controlled mode and (b) the corresponding indent in bulk Li.

Since a large misalignment between the flat punch and samples can result in significant errors in flat punch indentation measurements [211, 212], we measured the angular misalignment by performing shallow indents in bulk Li. As shown in Figure 7.1, the full contract between the flat punch and Li is established with a maximum indentation depth of 594 nm. Since the maximum depth of all flat punch indentation measurements is larger than 3000 nm, full contact between the punch and the samples is established prior to indentation creep measurements. Therefore, the influence of the misalignment on flat punch indentation measurements can be neglected in this study.

Figure 7.2(a) shows that the flat punch indentation load-displacement curves of bulk Li are reproducible. A typical indent is shown in Figure 7.2(b). Bulk Li shows clearly creep behavior during the holding period. The fast increase of the creep displacement even transfers the force from the sample to the springs in the load-controlling system of the Nanoindenter, which results in a continuous drop of the maximum load during the holding period.[6] As shown in Figure 7.2(c), the creep displacement increases quickly during the

[6] Here, the load drop occurs because the current to the actuator's electromagnetic coil was held constant rather than utilizing a feedback loop to change the current with time to maintain a constant load on the sample.

initial holding stage. Then the creep rate gradually decreases over the subsequent holding period. The total creep displacement increases almost linearly with the mean indentation pressure (p_{mean}), as shown in Figure 7.2(d).

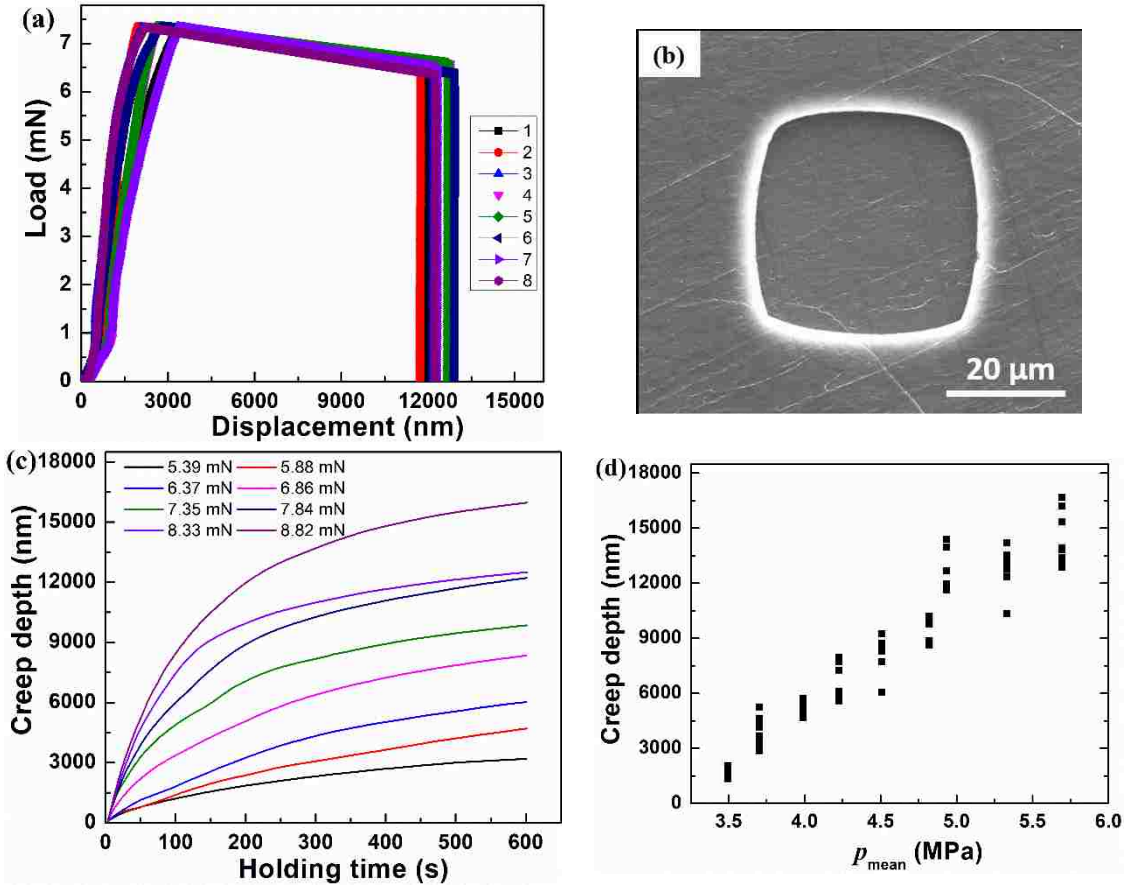

Figure 7.2 (a) Typical load-displacement curves of flat punch indentation measurements in bulk Li. (b) A typical indent in bulk Li. (c) The creep depth-time profiles during the 600 s holding period, and (d) the creep depth - mean pressure profile of bulk Li.

To better understand the creep behavior of bulk Li, it is necessary to derive the relationship between stress and creep strain rate at the steady-state creep stage. The creep strain rate is proportional to strain rate term ($\dot{\varepsilon}_{fp}$) of flat punch indentation measurements [213, 214],

$$\dot{\varepsilon} = C_1 \dot{\varepsilon}_{fp} = C_1 \frac{dh}{D} \frac{1}{dt} \tag{7.1}$$

where C_1 is a constant and D is the equivalent diameter of the flat punch. D = 41.62 μm for our flat punch. As shown in Figure 7.3(a), $\dot{\varepsilon}_{fp}$ shows a decreasing trend at the initial holding period and then reaches to a constant value range after 400 s, which implies the stead-state creep. The expectation value of the steady-state creep strain rate during 400 – 600 s holding is determined by using Gaussian distribution,

$$f = \frac{1}{\sigma\sqrt{2\pi}} e^{-\frac{(x-\mu)^2}{2\sigma^2}} \tag{7.2}$$

where μ is the mean value or the expectation value and σ is the standard deviation. Figure 7.3(b) shows a typical Gaussian distribution histogram of $\dot{\varepsilon}_{fp}$ during the holding period from 400 s to 600 s. The creep stress of flat punch indentation measurements is proportional to the mean pressure [213, 214],

$$\sigma = C_2 p_{mean} = C_2 \frac{F_{max}}{A_{punch}} \tag{7.3}$$

where C_2 is a constant, F_{max} is the maximum load, and A_{punch} is the project area of the flat punch. $A_{punch} \approx 1360$ μm^2 in this study. The average mean pressure between 400 s and 600s holding is used for creep analysis. Here we neglect the lateral friction between the flat punch and Li because it has little influence on the flat punch indentation measurements at the maximum depth (< 20 μm) in this study [215]. If we assume that bulk Li follows the power-law creep [216],

$$\dot{\varepsilon} = A\sigma^n d^{-p} \exp(-Q_c/RT) \tag{7.4}$$

where A is a constant, n is the stress exponent, d is the grain size, and p is the grain size exponent, Q_c is the activation energy for creep, T is absolute temperature and R is the gas constant. Combing Eq. (7.1)-(7.4), the stress exponent can be determined from the slope of the logarithmic relationship of $\dot{\varepsilon}_{fp} - p_{mean}$.

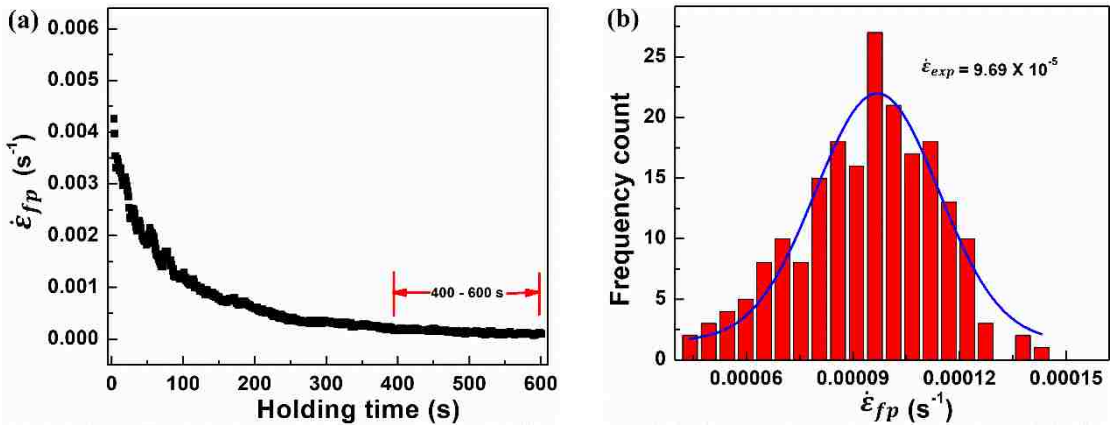

Figure 7.3 (a) A typical $\dot{\varepsilon}_{fp}$ - time profile of bulk Li during the 600 s holding period. The maximum load is 7.84 mN. (b) The corresponding distribution histogram of $\dot{\varepsilon}_{fp}$ during the holding period from 400 s to 600 s.

Figure 7.4(a) shows the $\dot{\varepsilon}_{fp} - p_{mean}$ profile of bulk Li. The creep strain rate increases with increasing nominal stress. The logarithm of the expectation values of $\dot{\varepsilon}_{fp}$ as a function of the logarithm of the p_{mean} is plotted in Figure 7.4(b). In the stress range between 3.49 MPa and 4.5 MPa, the logarithm of $\dot{\varepsilon}_{fp}$ increases linearly with the logarithm of p_{mean}, while it becomes constant under larger mean pressure. If we assume a power law creep mechanism for the linear region, the stress exponent is determined to be 5.75, which is close to those obtained by compression and tensile tests of Li metal at room temperature [195, 209, 216]. The stress exponent suggests that the creep of bulk Li is dominated by dislocation climb at room temperature [216].

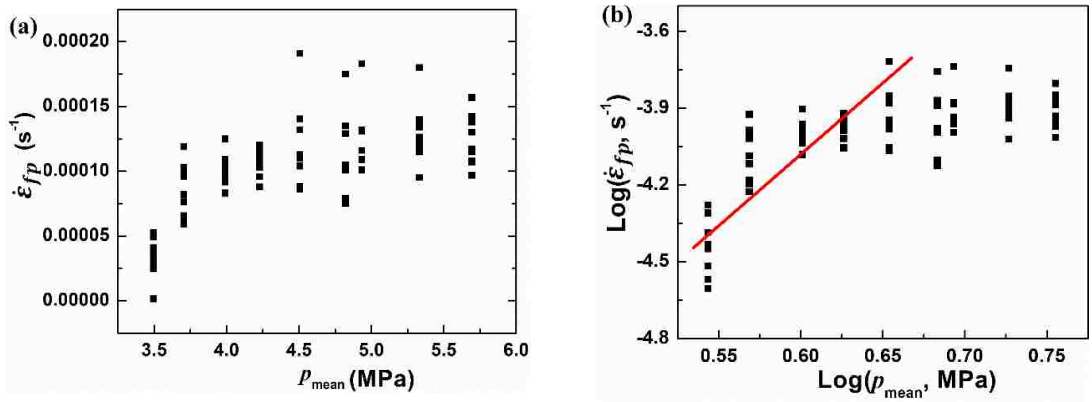

Figure 7.4 (a) The relationship between $\dot{\varepsilon}_{fp}$ and p_{mean} and (b) The logarithm relationship between $\dot{\varepsilon}_{fp}$ and p_{mean} of bulk Li.

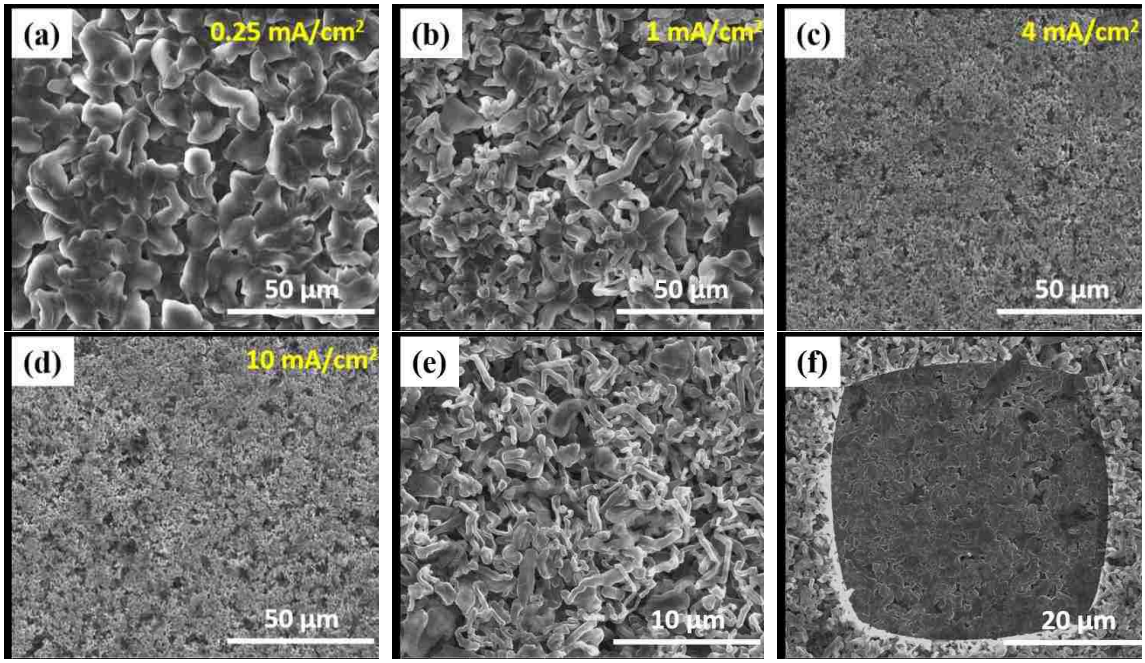

Figure 7.5 Microstructure of mossy Li obtained under different current densities: (a) 0.25 mA cm^{-2}, (b) 1.00 mA cm^{-2}, (b) 4.00 mA cm^{-2}, (b) 10.00 mA cm^{-2}. (e) A high magnification SEM image of the mossy Li plated under the current density of 10 mA cm^{-2}. (f) A typical indent in the mossy Li plated under the current density of 10 mA cm^{-2}.

As shown in Figure 7.5, electroplated mossy Li has porous microstructure. The morphology of Li dendrites depends on the current density. Under a high current density of 10 mA cm^{-2}, needle-like dendrites dominate the mossy Li, as shown in Figure 7.5(e). As the current density increases, the dimensions of dendrites increase, especially large Li chunks are generated under a low current density of 0.25 mA cm^{-2}, as shown in Figure 7.5(a).

Cross-sectional SEM images, as shown in Figure 7.6, show that the dendrite aligned perpendicularly to the bulk Li surface and there are numerous pore spaces in the mossy Li. Cross sectional observations also show that the dendrite morphology in the mossy layer also depends on the current density, that is, a low current density generate more needle-like dendrite, while large Li chunks are generated under low current density. The average porosity of mossy Li is determined from the thickness of the mossy layer and listed in

Table 7.1. Both the thickness and the porosity does not show a clear dependence on the current density.

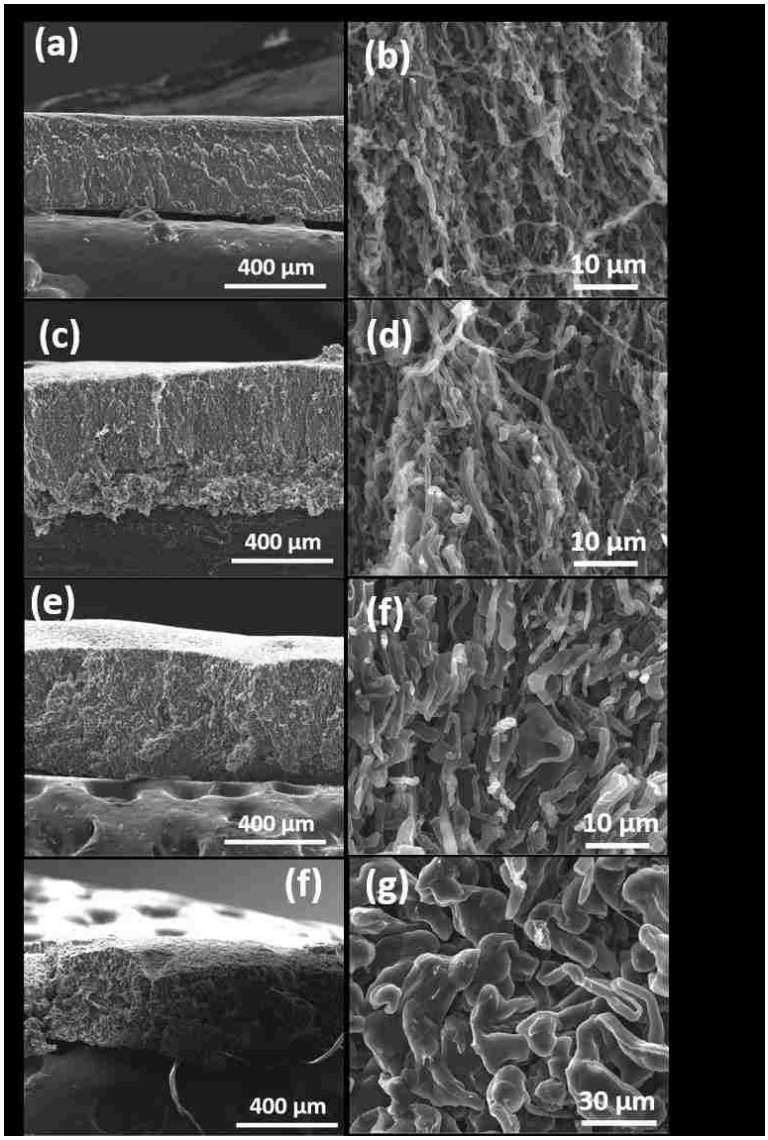

Figure 7.6 (a), (c), (e), and (f) are cross sectional SEM images of mossy Li obtained from electroplating under the current densities of 10.00 mA cm^{-2}, 4.00 mA cm^{-2}, 1.00 mA cm^{-2}, and 0.25 mA cm^{-2}, respectively. (b), (d), (f), and (g) are high magnification images corresponding to (a), (c), (e), and (f), respectively.

Table 7.1 The thickness and porosity of mossy Li obtained from electroplating under different current densities.

Current density (mA cm^{-2})	Thickness (μm)	Porosity (%)
0.25	356 ± 28.3	45 ± 4.5
1.00	502 ± 10.1	61 ± 0.76
4.00	441 ± 4.1	56 ± 0.4
10.00	360 ± 4.4	46 ± 0.7

Figure 7.7(a) shows that the flat punch indentation load-displacement curves of mossy Li are not ideally consistent, probably because of the random nature of the distribution of pores and surface roughness. Overall, the indentation depth corresponding to the maximum load and the creep displacement during the holding period of mossy Li are remarkably smaller than those of bulk Li. Although densification also contributes to the deformation of mossy Li, flat punch indentation indeed induces the deformation of Li dendrites, as shown in Figure 7.5(f).

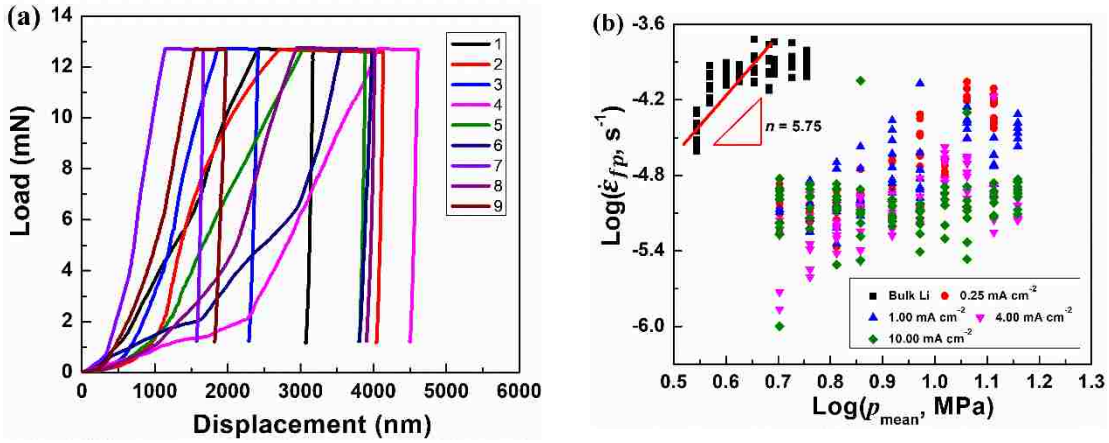

Figure 7.7 (a) Typical load-displacement curves of flat punch indentation measurements of mossy Li plated under a current density of 1 mA cm^{-2} with the maximum load of 12.74 mN. (b) The logarithmic relationship between $\dot{\varepsilon}_{fp}$ and p_{mean}.

Statistically, the steady-state creep strain rate ($\dot{\varepsilon}_{fp}$) of mossy is much smaller than that of bulk Li under the same stress level, as shown in Figure 7.7(b). Therefore, mossy Li has significantly higher deformation and creep resistance than bulk Li. In addition, the creep strain rate of mossy Li plated under the current densities of 0.25 mA cm^{-2} and 1.0 mA cm^{-2} show slightly dependence on the average indentation stress, while the strain rate

of mossy Li plated under the current densities of 4.0 mA cm^{-2} and 10.0 mA cm^{-2} keeps almost constant over the mean pressure range between 5.04 MPa and 14.41 MPa.

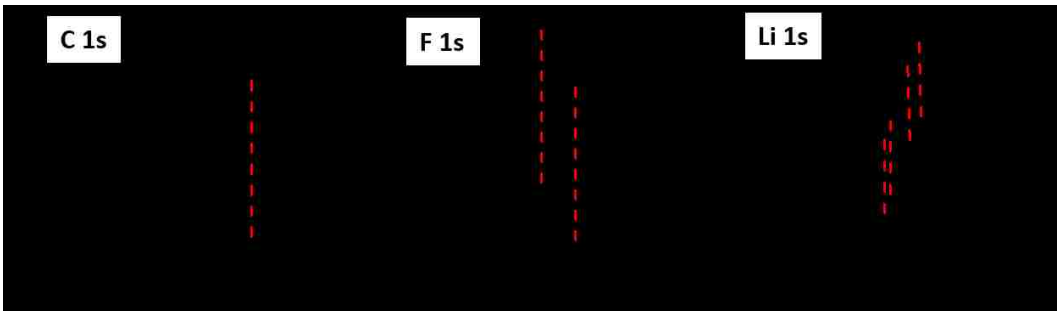

Figure 7.8 XPS spectra of the mossy Li: (a) C 1s, (b) F 1s, and (c) Li 1s.

Since the homologous temperature of Li metal is 0.66 at room temperature, both diffusion- and dislocation-mediated plasticity may dominate the indentation deformation and creep of bulk Li, which has a BCC crystalline structure. Different from bulk Li, mossy Li consists of numerous Li dendrites. The surface of Li dendrites is "coated" with a SEI layer consisting of LiF, Li_2CO_3, LiOH, Li_2O, and Li_xFP_y, as shown in the XPS spectra (Figure 7.8). Knowing the microstructure of mossy Li, we suggest that the enhanced deformation and creep resistance of mossy Li may be attributed to the following reasons. (a) Dislocation starvation. Dislocations escape easily in Li dendrites because of their small size, leaving dendrites in a ''dislocation-starved'' state. Plastic deformation thus requires a continuous supply of fresh dislocations by nucleation from the surface, to sustain the strain rate, which requires a high stress [217-219]. (b) Strengthening effect of the SEI layer. Inorganic components of the SEI layer, such as LiF and Li_2CO_3, have much high modulus and strength than Li metal [90]. The deformation of SEI layer itself can increase the deformation resistance of mossy Li. (3) Suppressed diffusion of Li at the Li/SEI interface. Although SEI components synergistically promote the Li ion conductivity of SEI [144], SEI cannot conduct Li atoms on the surface. Therefore, surface diffusion-assisted creep is inhibited although Li dendrites have high specific surface area. To clarify the effect of SEI on the mechanical behavior of mossy Li, future study should focus on the influence of the surface chemistry on the mechanical behavior of mossy Li. Overall, the limited dislocation sources, high strength of SEI, and suppressed surface diffusion lead to the enhanced

deformation and creep resistance of mossy Li. Further efforts are needed to quantify the contribution of each factor.

7.5 Conclusions

We investigated the mechanical behavior of bulk and mossy Li using flat punch indentation measurements. Both bulk Li and mossy Li show clearly indentation creep behavior. The steady-state creep of bulk Li is dominated by dislocation climb over the mean pressure range between 3.49 MPa and 4.50 MPa. The steady-state creep strain rate of bulk Li trend to be constant under mean pressures larger than 4.50 MPa. Compared with bulk Li, mossy Li has significantly enhanced deformation and creep resistance. Therefore, cautions should be taken when using the mechanical properties of bulk Li to model the electrochemical-mechanical interactions associated with mossy Li. We proposed possible mechanisms, including the limited sources of dislocations in Li dendrites, SEI, and suppressed surface diffusion for the distinct mechanical behavior of mossy Li from bulk Li. To fully understand the mechanical behavior of mossy Li, future study may focus on the influence of porosity, surface chemistry, dendrite morphology, and mechanical properties of individual electroplated Li dendrites.

CHAPTER 8. CONCLUSIONS AND FUTURE WORK

8.1 Conclusions

Electromechanical degradation caused by the huge volume changes of Si particles during lithiation/delithiation cycling remains a major challenge for high capacity Si composite electrodes. To help understand and mitigate the degradation of Si-based electrodes, I have studied the evolution of mechanical properties, microstructure change, and associated lithiation/delithiation kinetics of Si composite electrodes made with different polymeric binders. Important insights into the correlation between mechanical properties and structural degradation of Si composite electrodes are as follows.

(1) During lithiation, the expansion of Si particles reduces the porosity but increase the thickness of Si composite electrodes, while the contraction of Si particles during delithiation increases the porosity but causes the decrease of the thickness of Si composite electrodes. The overall irreversible thickness change of Si composite electrodes show an increase trend during long-term cycling because an increasing amount of Si particles lose electronic conductivity and electrochemical activity during cycling.

(2) Unlike the lithiation-induced softening of Si thin film and Si wafer electrodes, the elastic modulus and hardness of Si composite electrodes increase with increasing lithium concentration within one cycle mainly due to the porosity change and the porosity-dependent deformation mechanisms (*i.e.*, densification *vs.* deformation of individual particles). The elastic modulus and hardness of Si composite electrodes decreases as the cycling number increases due to the accumulated porosity and irreversible volume changes.

(3) The mechanical properties of Si composite electrodes are highly influenced by the electrolyte. Both the elastic modulus and hardness of Si composite electrodes measured under wet conditions are smaller than those measured under dry conditions because polymeric binders soften in the liquid organic electrolyte.

Polymeric binders are an essential component of Si composite electrodes to enhance mechanical integrity, maintain electronic conductivity, and improve the cycle life and stability of Si composite electrodes. Understanding the binder-dependent electromechanical degradation of Si composite electrodes is indispensable to guiding the

design of polymeric binders for Si-based electrodes. My comparative study on the influence of polymeric binders on the mechanical degradation of Si composite electrodes revealed that,

(1) Binders influence the porosity and irreversible thickness change of Si composite electrodes. Stiff binders, such as Na-CMC and SA, can well constrain the volume changes and help maintain the electronic conductivity of Si composite electrodes during cycling. In contrast, soft binders (such as PVDF and Nafion) are not strong enough to accommodate the repeated volume change and lead to large irreversible thickness change of Si composite electrodes during cycling.

(2) Mechanical properties of polymeric binders, instead of the adhesion between binders and Si, largely determine the magnitudes of the elastic modulus and hardness of Si composite electrodes. In addition, the softening behavior of binders in the electrolyte influences the mechanical properties of Si composite electrodes measured under wet conditions. But binders do not change the increasing trend of the elastic modulus and hardness of Si composite electrodes with increasing lithium concentration during cycling.

(3) Although strong adhesion between binders and Si benefits the connection between Si particle and the binder/carbon black matrix, it induces large localized tensile stress and leads to extensive cracks of Si composite electrodes during delithiation. Cracks periodically open and close at the same locations in Si/SA, Si/Na-CMC, and Si/Nafion electrodes as Si particles contract and expand repeatedly during cycling. In contrast, no cracks form in Si/PVDF electrodes since the weak adhesion between PVDF and Si particles is unable to generate localized tensile stress large enough to trigger cracking.

(4) The capacity fading of Si composite electrodes has a positive correlation with the evolution of the increasing SEI and charge transfer resistance during long-term cycling. The loss of electronic connection of Si particles from the matrix caused by the weak Si/binder adhesion or the irreversible volume change is one of the major factors for the degradation of Si composite electrodes.

(5) Neither the adhesion strength between binders and Si nor the mechanical properties of binders themselves can solely determine the electrochemical performance of Si composite electrodes. Effective binders for Si composite electrodes may require a certain

balance between their adhesion with Si and the mechanical properties of themselves, which require future efforts.

Based on the above understanding of the mechanical and electrochemical degradation of Si composite electrodes, a facile approach, that is, partial delithiation, was proposed to improve the mechanical integrity as well as cycling stability of Si composite electrodes. Experimental results confirmed the feasibility and effectiveness of this approach.

Mechanical behavior of Li is indispensable to gain a fundamental understanding of the electrochemical-mechanical interactions associated with Li electrodes. Considering the high sensitivity of Li metal to oxygen and water vapor, I adopted an environmental nanoindentation system to measure the mechanical behavior of bulk and mossy Li using a Berkovich indenter and a flat punch indenter. The knowledge gap of mechanical properties of bulk Li metal and mossy Li is partially filled with the following conclusions.

(1) Indentation responses of bulk Li showed clearly time-dependent deformation behavior. Using an iterative finite element modeling approach, I determined the viscoplastic constitutive law for bulk Li as Eq. (6.7). In addition, finite element modeling show that the elastic modulus, on the order of GPas, and the Poisson's ratio, over the range between 0.05 to 0.45 has little influence on the indentation deformation of bulk Li.

(2) Flat punch indentation measurements showed that the creep behavior of bulk Li over the mean pressure between 3.49 MPa and 4.50 MPa follows the power law creep. The stress exponent of 5.75 indicates that dislocation climb-controlled creep dominates the steady-state creep of bulk Li. The steady-state creep strain rate under higher mean pressure keeps constant.

(3) Statistical analysis of the flat punch indentation measurements shows that the porous mossy Li has significantly higher deformation and creep resistance than bulk Li, which can be attributed to the limited dislocation source in Li dendrites and SEI.

8.2 Future Work

Based on the understanding of the binder-dependent electromechanical degradation of Si composite electrodes in this dissertation, future efforts to overcome the

electromechanical degradation and improving the stability of Si composite electrodes are suggested as,

(1) Novel polymeric binders. Other than electrochemical stability, the mechanical properties of binders together with the adhesion between binders and Si can strongly affect the performance of Si composite electrodes based on the comparative studies between PVDF, Nafion, Na-CMC, and SA. An effective binder should, therefore, have a balance between adhesion strength (with Si and CB), strength, and elasticity. Modeling efforts are needed to quantify such a balance and guide the synthesis of new binders or chemical modifications of conventional binders for Si-based electrodes.

(2) Designing heterostructure of Si composite electrodes. Irreversible volume changes, micro channel cracks, and the delamination of Si particles from the conductive matrix are three major factors for the mechanical degradation of Si composite electrodes made of existing "effective" binders, such as Na-CMC and SA. Porous heterostructure which can accommodate the volume change of Si particles as well as form strong adhesion between Si and the matrix would effectively alleviate these mechanical degradations and stabilize the electrochemical performance of Si-based electrodes.

The mechanical characterization of mossy Li in this dissertation is limited to the average mechanical response of mossy Li. Future mechanical measurements can be conducted on individual Li dendrites by using atomic force microscopy (AFM) and *in situ* micropillar indentation in a SEM or transmission electron microscopy (TEM). After knowing the mechanical behavior of Li dendrites, localized electrochemical-mechanical interactions between Li dendrites and mechanical inhibitors (*e.g.*, coatings, separators, and SEIs) can be better understood, which, in return, help design mechanical inhibitors and improve the safety and cycling performance of Li metal electrodes.

REFERENCES

[1] T. Berry, The dream of the earth, Sierra Club Books San Francisco, 1988.
[2] V. Etacheri, R. Marom, R. Elazari, G. Salitra, D. Aurbach, Energy & Environmental Science, 4 (2011) 3243-3262.
[3] K. Xu, Chemical Reviews, 114 (2014) 11503-11618.
[4] A. Manthiram, Y. Fu, Y.-S. Su, Accounts of chemical research, 46 (2012) 1125-1134.
[5] J. Song, Z. Yu, M.L. Gordin, D. Wang, Nano letters, 16 (2016) 864-870.
[6] B.-C. Yu, K. Park, J.-H. Jang, J.B. Goodenough, ACS Energy Letters, 1 (2016) 633-637.
[7] T. McKeown, The role of medicine: dream, mirage, or nemesis?, Princeton University Press, 2014.
[8] D. Aurbach, B.D. McCloskey, L.F. Nazar, P.G. Bruce, Nature Energy, 1 (2016) 16128.
[9] U. Farooqui, A. Ahmad, N. Hamid, Renewable and Sustainable Energy Reviews, 77 (2017) 1114-1129.
[10] M. Obrovac, V. Chevrier, Chemical reviews, 114 (2014) 11444-11502.
[11] X. Zuo, J. Zhu, P. Müller-Buschbaum, Y.-J. Cheng, Nano Energy, 31 (2017) 113-143.
[12] P. Meister, H. Jia, J. Li, R. Kloepsch, M. Winter, T. Placke, Chemistry of Materials, 28 (2016) 7203-7217.
[13] X.H. Liu, L. Zhong, S. Huang, S.X. Mao, T. Zhu, J.Y. Huang, Acs Nano, 6 (2012) 1522-1531.
[14] X.H. Liu, H. Zheng, L. Zhong, S. Huang, K. Karki, L.Q. Zhang, Y. Liu, A. Kushima, W.T. Liang, J.W. Wang, Nano letters, 11 (2011) 3312-3318.
[15] J. Li, A.K. Dozier, Y. Li, F. Yang, Y.-T. Cheng, Journal of The Electrochemical Society, 158 (2011) A689-A694.
[16] F. Holtstiege, A. Wilken, M. Winter, T. Placke, Physical Chemistry Chemical Physics, 19 (2017) 25905-25918.
[17] X. Su, K. Guo, T. Ma, P.A. Tamirisa, H. Ye, H. Gao, B.W. Sheldon, ACS Energy Letters, 2 (2017) 1729-1733.
[18] G. Belomoin, J. Therrien, M. Nayfeh, Applied Physics Letters, 77 (2000) 779-781.
[19] J. Kong, W.A. Yee, Y. Wei, L. Yang, J.M. Ang, S.L. Phua, S.Y. Wong, R. Zhou, Y. Dong, X. Li, Nanoscale, 5 (2013) 2967-2973.
[20] Y. Fan, Q. Zhang, C. Lu, Q. Xiao, X. Wang, B. kang Tay, Nanoscale, 5 (2013) 1503-1506.
[21] X. Huang, J. Yang, S. Mao, J. Chang, P.B. Hallac, C.R. Fell, B. Metz, J. Jiang, P.T. Hurley, J. Chen, Advanced Materials, 26 (2014) 4326-4332.
[22] G.-b. Cho, J.-k. Kim, S.-h. Lee, G.-t. Kim, J.-p. Noh, K.-k. Cho, K.-w. Kim, T.-h. Nam, H.-j. Ahn, Electrochimica Acta, 224 (2017) 649-659.
[23] X. Wang, L. Sun, R.A. Susantyoko, Y. Fan, Q. Zhang, Nano Energy, 8 (2014) 71-77.
[24] Y.-T. Cheng, M.W. Verbrugge, Journal of Applied Physics, 104 (2008) 083521.
[25] J. Xu, L. Zhang, Y. Wang, T. Chen, M. Al-Shroofy, Y.-T. Cheng, ACS applied materials & interfaces, 9 (2017) 3562-3569.
[26] O.O. Taiwo, J.M. Paz-García, S.A. Hall, T.M. Heenan, D.P. Finegan, R. Mokso, P. Villanueva-Pérez, A. Patera, D.J. Brett, P.R. Shearing, Journal of Power Sources, 342 (2017) 904-912.
[27] S. Choi, T.-w. Kwon, A. Coskun, J.W. Choi, Science, 357 (2017) 279-283.

[28] A. Magasinski, B. Zdyrko, I. Kovalenko, B. Hertzberg, R. Burtovyy, C.F. Huebner, T.F. Fuller, I. Luzinov, G. Yushin, ACS applied materials & interfaces, 2 (2010) 3004-3010.
[29] J. Xu, Q. Zhang, Y.-T. Cheng, Journal of The Electrochemical Society, 163 (2016) A401-A405.
[30] I. Kovalenko, B. Zdyrko, A. Magasinski, B. Hertzberg, Z. Milicev, R. Burtovyy, I. Luzinov, G. Yushin, Science, (2011) 1209150.
[31] D.M. Piper, J.J. Travis, M. Young, S.B. Son, S.C. Kim, K.H. Oh, S.M. George, C. Ban, S.H. Lee, Advanced Materials, 26 (2014) 1596-1601.
[32] S.-B. Son, Y. Wang, J. Xu, X. Li, M. Groner, A. Stokes, Y. Yang, Y.-T. Cheng, C. Ban, ACS applied materials & interfaces, 9 (2017) 40143-40150.
[33] Y. Sun, J. Lopez, H.W. Lee, N. Liu, G. Zheng, C.L. Wu, J. Sun, W. Liu, J.W. Chung, Z. Bao, Advanced Materials, 28 (2016) 2455-2461.
[34] W. Xu, J. Wang, F. Ding, X. Chen, E. Nasybulin, Y. Zhang, J.-G. Zhang, Energy & Environmental Science, 7 (2014) 513-537.
[35] X.-B. Cheng, R. Zhang, C.-Z. Zhao, Q. Zhang, Chemical reviews, 117 (2017) 10403-10473.
[36] X.B. Cheng, T.Z. Hou, R. Zhang, H.J. Peng, C.Z. Zhao, J.Q. Huang, Q. Zhang, Advanced Materials, 28 (2016) 2888-2895.
[37] M.H. Ryou, Y.M. Lee, Y. Lee, M. Winter, P. Bieker, Advanced Functional Materials, 25 (2015) 834-841.
[38] Z. Li, J. Huang, B.Y. Liaw, V. Metzler, J. Zhang, Journal of power sources, 254 (2014) 168-182.
[39] V. Giordani, W. Walker, V.S. Bryantsev, J. Uddin, G.V. Chase, D. Addison, Journal of The Electrochemical Society, 160 (2013) A1544-A1550.
[40] F. Ding, W. Xu, G.L. Graff, J. Zhang, M.L. Sushko, X. Chen, Y. Shao, M.H. Engelhard, Z. Nie, J. Xiao, Journal of the American Chemical Society, 135 (2013) 4450-4456.
[41] J.K.S. Goodman, P.A. Kohl, Journal of The Electrochemical Society, 161 (2014) D418-D424.
[42] Q. Yun, Y.B. He, W. Lv, Y. Zhao, B. Li, F. Kang, Q.H. Yang, Advanced Materials, 28 (2016) 6932-6939.
[43] R. Mukherjee, A.V. Thomas, D. Datta, E. Singh, J. Li, O. Eksik, V.B. Shenoy, N. Koratkar, Nature communications, 5 (2014) 3710.
[44] R. Zhang, X.B. Cheng, C.Z. Zhao, H.J. Peng, J.L. Shi, J.Q. Huang, J. Wang, F. Wei, Q. Zhang, Advanced Materials, 28 (2016) 2155-2162.
[45] Z. Liang, G. Zheng, C. Liu, N. Liu, W. Li, K. Yan, H. Yao, P.-C. Hsu, S. Chu, Y. Cui, Nano letters, 15 (2015) 2910-2916.
[46] C. Monroe, J. Newman, Journal of The Electrochemical Society, 151 (2004) A880-A886.
[47] C. Wang, Y. Gong, B. Liu, K. Fu, Y. Yao, E. Hitz, Y. Li, J. Dai, S. Xu, W. Luo, Nano letters, 17 (2016) 565-571.
[48] N.W. Li, Y.X. Yin, C.P. Yang, Y.G. Guo, Advanced materials, 28 (2016) 1853-1858.
[49] D. Zhou, R. Liu, Y.B. He, F. Li, M. Liu, B. Li, Q.H. Yang, Q. Cai, F. Kang, Advanced Energy Materials, 6 (2016) 1502214.
[50] L. Kawashita, D. Moore, J. Williams, Journal of Adhesion, 81 (2005) 561-586.

[51] S.F. Messner, R. Rosenfeld, Crime and the American dream, Cengage Learning, 2012.
[52] A.M. Gaikwad, A.C. Arias, ACS applied materials & interfaces, 9 (2017) 6390-6400.
[53] M. Park, H. Cha, Y. Lee, J. Hong, S.Y. Kim, J. Cho, Advanced Materials, 29 (2017) 1605773.
[54] H.A. Gasteiger, N.M. Marković, science, 324 (2009) 48-49.
[55] J. Chen, J. Liu, Y. Qi, T. Sun, X. Li, Journal of The Electrochemical Society, 160 (2013) A1502-A1509.
[56] W.C. Oliver, G.M. Pharr, Journal of materials research, 7 (1992) 1564-1583.
[57] Y.-T. Cheng, C.-M. Cheng, Journal of Materials Research, 20 (2005) 1046-1053.
[58] Y.-T. Cheng, C.-M. Cheng, Materials Science and Engineering: R: Reports, 44 (2004) 91-149.
[59] W. Liu, Y. Wang, Y. Ma, Q. Yu, Y. Huang, Materials Science and Engineering: A, 653 (2016) 13-22.
[60] Y. Wang, Y.-T. Cheng, Scripta Materialia, 130 (2017) 191-195.
[61] Y.-T. Cheng, C.-M. Cheng, Journal of Materials Research, 14 (1999) 3493-3496.
[62] R. Xu, H. Sun, L.S. de Vasconcelos, K. Zhao, Journal of The Electrochemical Society, 164 (2017) A3333-A3341.
[63] L.S. de Vasconcelos, R. Xu, J. Li, K. Zhao, Extreme Mechanics Letters, 9 (2016) 495-502.
[64] S. Bourderau, T. Brousse, D. Schleich, Journal of power sources, 81 (1999) 233-236.
[65] Q. Zhang, L. Han, J. Pan, Z. Chen, Y.-T. Cheng, Applied Physics Letters, 110 (2017) 133901.
[66] K. Zhao, W.L. Wang, J. Gregoire, M. Pharr, Z. Suo, J.J. Vlassak, E. Kaxiras, Nano letters, 11 (2011) 2962-2967.
[67] X. Wang, F. Fan, J. Wang, H. Wang, S. Tao, A. Yang, Y. Liu, H.B. Chew, S.X. Mao, T. Zhu, Nature communications, 6 (2015) 8417.
[68] D. Li, Y. Wang, J. Hu, B. Lu, D. Dang, J. Zhang, Y.-T.J.J.o.P.S. Cheng, 387 (2018) 9-15.
[69] D. Li, Y. Wang, J. Hu, B. Lu, Y.-T. Cheng, J. Zhang, Journal of Power Sources, 366 (2017) 80-85.
[70] H. Kim, C.-Y. Chou, J.G. Ekerdt, G.S. Hwang, The Journal of Physical Chemistry C, 115 (2011) 2514-2521.
[71] V.B. Shenoy, P. Johari, Y. Qi, Journal of Power Sources, 195 (2010) 6825-6830.
[72] B. Hertzberg, J. Benson, G. Yushin, Electrochemistry Communications, 13 (2011) 818-821.
[73] L.S. de Vasconcelos, R. Xu, K. Zhao, Journal of The Electrochemical Society, 164 (2017) A3840-A3847.
[74] M.D. Levi, N. Shpigel, S. Sigalov, V. Dargel, L. Daikhin, D. Aurbach, Electrochimica Acta, 232 (2017) 271-284.
[75] L.A. Riley, A.S. Cavanagh, S.M. George, S.-H. Lee, A.C. Dillon, Electrochemical and Solid-State Letters, 14 (2011) A29-A31.
[76] D. Antartis, S. Dillon, I. Chasiotis, Journal of Composite Materials, 49 (2015) 1849-1862.
[77] S. Malmgren, K. Ciosek, R. Lindblad, S. Plogmaker, J. Kühn, H. Rensmo, K. Edström, M. Hahlin, Electrochimica Acta, 105 (2013) 83-91.

[78] K.W. Schroder, H. Celio, L.J. Webb, K.J. Stevenson, The Journal of Physical Chemistry C, 116 (2012) 19737-19747.
[79] M. Gu, Z. Wang, J.G. Connell, D.E. Perea, L.J. Lauhon, F. Gao, C. Wang, ACS nano, 7 (2013) 6303-6309.
[80] W.-R. Liu, M.-H. Yang, H.-C. Wu, S. Chiao, N.-L. Wu, Electrochemical and Solid-State Letters, 8 (2005) A100-A103.
[81] K. Takahashi, K. Higa, S. Mair, M. Chintapalli, N. Balsara, V. Srinivasan, Journal of The Electrochemical Society, 163 (2016) A385-A395.
[82] C. Ban, S.M. George, Advanced Materials Interfaces, 3 (2016) 1600762.
[83] K. Rhodes, R. Meisner, Y. Kim, N. Dudney, C. Daniel, Journal of the electrochemical society, 158 (2011) A890-A897.
[84] J. Li, J. Dahn, Journal of The Electrochemical Society, 154 (2007) A156-A161.
[85] T. Hatchard, J. Dahn, Journal of The Electrochemical Society, 151 (2004) A838-A842.
[86] S. Misra, N. Liu, J. Nelson, S.S. Hong, Y. Cui, M.F. Toney, Acs Nano, 6 (2012) 5465-5473.
[87] G. Constantinides, F.-J. Ulm, Journal of the Mechanics and Physics of Solids, 55 (2007) 64-90.
[88] V. Kuznetsov, A.-H. Zinn, G. Zampardi, S. Borhani-Haghighi, F. La Mantia, A. Ludwig, W. Schuhmann, E. Ventosa, ACS applied materials & interfaces, 7 (2015) 23554-23563.
[89] J. Zhang, R. Wang, X. Yang, W. Lu, X. Wu, X. Wang, H. Li, L. Chen, Nano letters, 12 (2012) 2153-2157.
[90] Q. Zhang, X. Xiao, W. Zhou, Y.T. Cheng, M.W. Verbrugge, Advanced Energy Materials, 5 (2015) 1401398.
[91] C.R. Becker, S. Prokes, C.T. Love, ACS applied materials & interfaces, 8 (2016) 530-537.
[92] J. Zhao, L. Liao, F. Shi, T. Lei, G. Chen, A. Pei, J. Sun, K. Yan, G. Zhou, J. Xie, Journal of the American Chemical Society, 139 (2017) 11550-11558.
[93] H. Chen, M. Ling, L. Hencz, H.Y. Ling, G. Li, Z. Lin, G. Liu, S. Zhang, Chemical reviews, 118 (2018) 8936-8982.
[94] T.-w. Kwon, J.W. Choi, A. Coskun, Chemical Society Reviews, 47 (2018) 2145-2164.
[95] O.O. Taiwo, M. Loveridge, S.D. Beattie, D.P. Finegan, R. Bhagat, D.J. Brett, P.R. Shearing, Electrochimica Acta, 253 (2017) 85-92.
[96] J. Wen, Y. Wei, Y.-T. Cheng, Journal of the Mechanics and Physics of Solids, 116 (2018) 403-415.
[97] H. Wu, G. Zheng, N. Liu, T.J. Carney, Y. Yang, Y. Cui, Nano letters, 12 (2012) 904-909.
[98] F. Zhang, L. Wan, J. Chen, X. Li, X. Yan, Electrochimica Acta, 280 (2018) 86-93.
[99] J. Shin, E. Cho, Chemistry of Materials, 30 (2018) 3233-3243.
[100] P.-F. Cao, M. Naguib, Z. Du, E. Stacy, B. Li, T. Hong, K. Xing, D.N. Voylov, J. Li, D.L. Wood III, ACS applied materials & interfaces, 10 (2018) 3470-3478.
[101] Z.-J. Han, N. Yabuuchi, K. Shimomura, M. Murase, H. Yui, S. Komaba, Energy & environmental science, 5 (2012) 9014-9020.
[102] X. Zhu, F. Zhang, L. Zhang, L. Zhang, Y. Song, T. Jiang, S. Sayed, C. Lu, X. Wang, J. Sun, Advanced Functional Materials, 28 (2018) 1705015.

[103] J. Hu, Y. Wang, D. Li, Y.-T. Cheng, Journal of Power Sources, 397 (2018) 223-230.
[104] M.H. Ryou, J. Kim, I. Lee, S. Kim, Y.K. Jeong, S. Hong, J.H. Ryu, T.S. Kim, J.K. Park, H. Lee, Advanced materials, 25 (2013) 1571-1576.
[105] H. Buqa, M. Holzapfel, F. Krumeich, C. Veit, P. Novák, Journal of Power Sources, 161 (2006) 617-622.
[106] B. Hu, I.A. Shkrob, S. Zhang, L. Zhang, J. Zhang, Y. Li, C. Liao, Z. Zhang, W. Lu, L. Zhang, Journal of Power Sources, 378 (2018) 671-676.
[107] W. Porcher, S. Chazelle, A. Boulineau, N. Mariage, J. Alper, T. Van Rompaey, J.-S. Bridel, C. Haon, Journal of The Electrochemical Society, 164 (2017) A3633-A3640.
[108] Y. Bie, J. Yang, Y. Nuli, J. Wang, Journal of Materials Chemistry A, 5 (2017) 1919-1924.
[109] C.R. Hernandez, A. Etiemble, T. Douillard, D. Mazouzi, Z. Karkar, E. Maire, D. Guyomard, B. Lestriez, L. Roué, Advanced Energy Materials, 8 (2018) 1701787.
[110] Y. Zhao, P. Stein, Y. Bai, M. Al-Siraj, Y. Yang, B.-X. Xu, Journal of Power Sources, 413 (2019) 259-283.
[111] C. Zhang, J. Xu, L. Cao, Z. Wu, S. Santhanagopalan, Journal of Power Sources, 357 (2017) 126-137.
[112] L. Yang, M. Furczon, A. Xiao, B. Lucht, Z. Zhang, D. Abraham, Journal of Power Sources, 195 (2010) 1698-1705.
[113] Y. Wang, Q. Zhang, D. Li, J. Hu, J. Xu, D. Dang, X. Xiao, Y.T. Cheng, Advanced Energy Materials, 8 (2018) 1702578.
[114] R.F. Landel, L.E. Nielsen, Mechanical properties of polymers and composites, CRC press, 1993.
[115] L.J. Gibson, M.F. Ashby, Cellular solids: structure and properties, Cambridge university press, 1999.
[116] C.C. Nguyen, T. Yoon, D.M. Seo, P. Guduru, B.L. Lucht, ACS applied materials & interfaces, 8 (2016) 12211-12220.
[117] Y. Kawano, Y. Wang, R.A. Palmer, S.R. Aubuchon, Polímeros, 12 (2002) 96-101.
[118] C. Zhao, T. Wada, V. De Andrade, D. Gürsoy, H. Kato, Y.-c.K. Chen-Wiegart, Nano energy, 52 (2018) 381-390.
[119] E. Radvanyi, W. Porcher, E. De Vito, A. Montani, S. Franger, S.J.S.J.P.C.C.P. Larbi, 16 (2014) 17142-17153.
[120] Y. Oumellal, N. Delpuech, D. Mazouzi, N. Dupre, J. Gaubicher, P. Moreau, P. Soudan, B. Lestriez, D.J.J.o.M.C. Guyomard, 21 (2011) 6201-6208.
[121] S. Ahmed, I. Bloom, A.N. Jansen, T. Tanim, E.J. Dufek, A. Pesaran, A. Burnham, R.B. Carlson, F. Dias, K. Hardy, Journal of Power Sources, 367 (2017) 250-262.
[122] Y. Jin, K. Liu, J. Lang, D. Zhuo, Z. Huang, C.-a. Wang, H. Wu, Y. Cui, Nature Energy, 3 (2018) 732.
[123] Z. Liu, Q. Yu, Y. Zhao, R. He, M. Xu, S. Feng, S. Li, L. Zhou, L. Mai, Chemical Society Reviews, 48 (2019) 285-309.
[124] Y. Son, S. Sim, H. Ma, M. Choi, Y. Son, N. Park, J. Cho, M. Park, Advanced Materials, 30 (2018) 1705430.
[125] S.P. Nadimpalli, V.A. Sethuraman, S. Dalavi, B. Lucht, M.J. Chon, V.B. Shenoy, P.R. Guduru, Journal of Power Sources, 215 (2012) 145-151.
[126] X. Xiao, P. Liu, M. Verbrugge, H. Haftbaradaran, H.J.J.o.P.S. Gao, 196 (2011) 1409-1416.

[127] J.R. Szczech, S. Jin, Energy & Environmental Science, 4 (2011) 56-72.
[128] T. Munaoka, X. Yan, J. Lopez, J.W. To, J. Park, J.B.H. Tok, Y. Cui, Z. Bao, Advanced Energy Materials, 8 (2018) 1703138.
[129] C. Wang, H. Wu, Z. Chen, M.T. McDowell, Y. Cui, Z. Bao, Nature chemistry, 5 (2013) 1042.
[130] C.R. Hernandez, Z. Karkar, D. Guyomard, B. Lestriez, L. Roué, Electrochemistry Communications, 61 (2015) 102-105.
[131] C.-S. Tang, Y.-J. Cui, B. Shi, A.-M. Tang, C. Liu, Geoderma, 166 (2011) 111-118.
[132] M. Stein, A. Mistry, P.P. Mukherjee, Journal of The Electrochemical Society, 164 (2017) A1616-A1627.
[133] J.W. Hutchinson, Z. Suo, Mixed mode cracking in layered materials, in: Advances in applied mechanics, Elsevier, 1991, pp. 63-191.
[134] T. Yoon, C. Xiao, J. Liu, Y. Wang, S. Son, A. Burrell, C. Ban, Journal of Power Sources, 425 (2019) 44-49.
[135] Y.S. Choi, M. Pharr, K.H. Oh, J.J. Vlassak, Journal of Power Sources, 294 (2015) 159-166.
[136] M. Pharr, Z. Suo, J.J. Vlassak, Nano letters, 13 (2013) 5570-5577.
[137] R.R. Garsuch, D.-B. Le, A. Garsuch, J. Li, S. Wang, A. Farooq, J. Dahn, Journal of The Electrochemical Society, 155 (2008) A721-A724.
[138] G.A. Ozin, I. Manners, S. Fournier‐Bidoz, A. Arsenault, Advanced Materials, 17 (2005) 3011-3018.
[139] D. Li, Y. Wang, J. Hu, B. Lu, D. Dang, J. Zhang, Y.-T. Cheng, Journal of Power Sources, 387 (2018) 9-15.
[140] R. Kumar, J.H. Woo, X. Xiao, B.W. Sheldon, Journal of The Electrochemical Society, 164 (2017) A3750-A3765.
[141] M.J. Chon, V.A. Sethuraman, A. Mccormick, ., V. Srinivasan, ., P.R. Guduru, Physical Review Letters, 107 (2011) 045503.
[142] Q. Li, K.-S. Kim, in: Proceedings of the Royal Society of London A: Mathematical, Physical and Engineering Sciences, The Royal Society, 2008, pp. 1319-1343.
[143] D. Mazouzi, Z. Karkar, C.R. Hernandez, P.J. Manero, D. Guyomard, L. Roué, B. Lestriez, Journal of Power Sources, 280 (2015) 533-549.
[144] Q. Zhang, J. Pan, P. Lu, Z. Liu, M.W. Verbrugge, B.W. Sheldon, Y.-T. Cheng, Y. Qi, X. Xiao, Nano letters, 16 (2016) 2011-2016.
[145] Z. Xu, J. Yang, T. Zhang, Y. Nuli, J. Wang, S.-i. Hirano, Joule, 2 (2018) 950-961.
[146] V. Vanpeene, J. Villanova, A. King, B. Lestriez, E. Maire, L. Roué, Advanced Energy Materials, (2019) 1803947.
[147] D. Andre, M. Meiler, K. Steiner, C. Wimmer, T. Soczka-Guth, D. Sauer, Journal of Power Sources, 196 (2011) 5334-5341.
[148] D. Andre, M. Meiler, K. Steiner, H. Walz, T. Soczka-Guth, D. Sauer, Journal of Power Sources, 196 (2011) 5349-5356.
[149] A. Eddahech, O. Briat, N. Bertrand, J.-Y. Deletage, J.-M. Vinassa, International Journal of Electrical Power & Energy Systems, 42 (2012) 487-494.
[150] J. Guo, A. Sun, X. Chen, C. Wang, A. Manivannan, Electrochimica Acta, 56 (2011) 3981-3987.
[151] E. Pollak, G. Salitra, V. Baranchugov, D. Aurbach, The Journal of Physical Chemistry C, 111 (2007) 11437-11444.

[152] E. Casero, A. Parra-Alfambra, M. Petit-Domínguez, F. Pariente, E. Lorenzo, C. Alonso, Electrochemistry Communications, 20 (2012) 63-66.
[153] R. Ruffo, S.S. Hong, C.K. Chan, R.A. Huggins, Y. Cui, The Journal of Physical Chemistry C, 113 (2009) 11390-11398.
[154] M. Klett, J.A. Gilbert, S.E. Trask, B.J. Polzin, A.N. Jansen, D.W. Dees, D.P. Abraham, Journal of The Electrochemical Society, 163 (2016) A875-A887.
[155] W.-R. Liu, J.-H. Wang, H.-C. Wu, D.-T. Shieh, M.-H. Yang, N.-L. Wu, Journal of the electrochemical society, 152 (2005) A1719-A1725.
[156] K.K. Chandrasiri, C.C. Nguyen, B.S. Parimalam, S. Jurng, B.L. Lucht, Journal of The Electrochemical Society, 165 (2018) A1991-A1996.
[157] K. Schroder, J. Alvarado, T.A. Yersak, J. Li, N. Dudney, L.J. Webb, Y.S. Meng, K.J. Stevenson, Chemistry of Materials, 27 (2015) 5531-5542.
[158] Y. Oumellal, N. Delpuech, D. Mazouzi, N. Dupre, J. Gaubicher, P. Moreau, P. Soudan, B. Lestriez, D. Guyomard, Journal of Materials Chemistry, 21 (2011) 6201-6208.
[159] E. Radvanyi, W. Porcher, E. De Vito, A. Montani, S. Franger, S.J.S. Larbi, Physical Chemistry Chemical Physics, 16 (2014) 17142-17153.
[160] Y. Li, B. Lu, B. Guo, Y. Song, J. Zhang, Electrochimica Acta, 295 (2019) 778-786.
[161] M. Verbrugge, X. Xiao, Q. Zhang, M. Balogh, K. Raghunathan, D. Baker, Journal of The Electrochemical Society, 164 (2017) A156-A167.
[162] P.G. Bruce, S.A. Freunberger, L.J. Hardwick, J.-M. Tarascon, Nature materials, 11 (2012) 19.
[163] X. Ji, L.F. Nazar, Journal of Materials Chemistry, 20 (2010) 9821-9826.
[164] Y. Cao, X. Meng, J.W. Elam, ChemElectroChem, 3 (2016) 858-863.
[165] M. Wu, Z. Wen, Y. Liu, X. Wang, L. Huang, Journal of Power Sources, 196 (2011) 8091-8097.
[166] A. Ferrese, J. Newman, Journal of The Electrochemical Society, 161 (2014) A948-A954.
[167] A. Ferrese, J. Newman, Journal of The Electrochemical Society, 161 (2014) A1350-A1359.
[168] A. Ferrese, P. Albertus, J. Christensen, J. Newman, Journal of The Electrochemical Society, 159 (2012) A1615-A1623.
[169] S. Tariq, K. Ammigan, P. Hurh, R. Schultz, P. Liu, J. Shang, in: Proceedings of the 2003 particle accelerator conference, IEEE, 2003, pp. 1452-1454.
[170] R.P. Schultz, in, Fermi National Accelerator Lab., Batavia, IL (US), 2002.
[171] W. Robertson, D. Montgomery, Physical Review, 117 (1960) 440.
[172] G. Zhao, F. Yang, Materials Science and Engineering: A, 591 (2014) 97-104.
[173] F.-J. Wang, X. Ma, Y.-Y. Qian, Journal of materials science, 40 (2005) 1923-1928.
[174] R.W. Chang, F.P. McCluskey, Journal of Electronic Materials, 38 (2009) 1855-1859.
[175] I. Thornton, R. Rautiu, S. Brush, IC Consultants Ltd, London, UK, (2001).
[176] A. Bolshakov, W. Oliver, G. Pharr, Journal of Materials Research, 11 (1996) 760-768.
[177] J. Yan, A.M. Karlsson, X. Chen, International Journal of Solids and Structures, 44 (2007) 3720-3737.
[178] A. Ngan, B. Tang, Journal of Materials Research, 17 (2002) 2604-2610.
[179] H.F. William, USA: University of Michigan, (2005).
[180] G. Ernst, C. Artner, O. Blaschko, G. Krexner, Physical Review B, 33 (1986) 6465.

[181] L. Anand, International Journal of Plasticity, 1 (1985) 213-231.
[182] G.R. Johnson, Proc. 7th Inf. Sympo. Ballistics, (1983) 541-547.
[183] P. Perzyna, Quarterly of applied mathematics, 20 (1963) 321-332.
[184] P. Perzyna, Zeitschrift für angewandte Mathematik und Physik ZAMP, 35 (1984) 848-867.
[185] R. Ubachs, P. Schreurs, M. Geers, Mechanics of materials, 39 (2007) 685-701.
[186] G.R. Cowper, P.S. Symonds, in, Brown Univ Providence Ri, 1957.
[187] M. Ahmad, K. Hubbard, M. Hu, Journal of Electronic Packaging, 127 (2005) 290-298.
[188] B. Wang, S. Yi, Journal of materials science letters, 21 (2002) 697-698.
[189] A. Skipor, S. Harren, J. Botsis, Journal of Engineering Materials and Technology, 118 (1996) 1-11.
[190] M. Dao, N.v. Chollacoop, K. Van Vliet, T. Venkatesh, S. Suresh, Acta materialia, 49 (2001) 3899-3918.
[191] N. Ogasawara, N. Chiba, X. Chen, Journal of Materials Research, 20 (2005) 2225-2234.
[192] Y.P. Cao, X.Q. Qian, J. Lu, Z.H. Yao, Journal of Materials Research, 20 (2005) 1194-1206.
[193] J. Alkorta, J.M. Martínez-Esnaola, J.G. Sevillano, Acta Materialia, 56 (2008) 884-893.
[194] J. Alkorta, J.M. Martínez-Esnaola, J.G. Sevillano, Journal of Materials Research, 23 (2008) 182-188.
[195] A. Masias, N. Felten, R. Garcia-Mendez, J. Wolfenstine, J. Sakamoto, Journal of Materials Science, 54 (2019) 2585-2600.
[196] R. Reed, C. McCowan, R. Walsh, L. Delgado, J. McColskey, Materials Science and Engineering: A, 102 (1988) 227-236.
[197] M.F. Ashby, D.R.H. Jones, Engineering Materials: An Introduction to Their Properties and Applications, Butterworth-Heinemann, 1996.
[198] P. Adeva, G. Caruana, O.A. Ruano, M. Torralba, Materials Science and Engineering: A, 194 (1995) 17-23.
[199] H. Ma, J.C. Suhling, Journal of materials science, 44 (2009) 1141-1158.
[200] J. Qian, W.A. Henderson, W. Xu, P. Bhattacharya, M. Engelhard, O. Borodin, J.-G. Zhang, Nature communications, 6 (2015) 6362.
[201] Q. Pang, X. Liang, A. Shyamsunder, L.F. Nazar, Joule, 1 (2017) 871-886.
[202] P. Barai, K. Higa, V. Srinivasan, Journal of The Electrochemical Society, 165 (2018) A2654-A2666.
[203] X. Yin, W. Tang, K.C. Phua, S. Adams, S.W. Lee, G.W. Zheng, Nano energy, 50 (2018) 659-664.
[204] P. Bai, J. Guo, M. Wang, A. Kushima, L. Su, J. Li, F.R. Brushett, M.Z. Bazant, Joule, 2 (2018) 2434-2449.
[205] C. Gao, Q. Dong, G. Zhang, H. Fan, H. Li, B. Hong, Y. Lai, ChemElectroChem, 6 (2019) 1134-1138.
[206] N.W. Li, Y. Shi, Y.X. Yin, X.X. Zeng, J.Y. Li, C.J. Li, L.J. Wan, R. Wen, Y.G. Guo, Angewandte Chemie International Edition, 57 (2018) 1505-1509.
[207] R. Xu, X.Q. Zhang, X.B. Cheng, H.J. Peng, C.Z. Zhao, C. Yan, J.Q. Huang, Advanced Functional Materials, 28 (2018) 1705838.

[208] S. Narayan, L. Anand, Extreme Mechanics Letters, 24 (2018) 21-29.
[209] W.S. LePage, Y. Chen, E. Kazyak, K.-H. Chen, A.J. Sanchez, A. Poli, E.M. Arruda, M. Thouless, N.P. Dasgupta, Journal of The Electrochemical Society, 166 (2019) A89-A97.
[210] C. Xu, Z. Ahmad, A. Aryanfar, V. Viswanathan, J.R. Greer, Proceedings of the National Academy of Sciences, 114 (2017) 57-61.
[211] N.B. Shahjahan, Z. Hu, Journal of Materials Research, 32 (2017) 1456-1465.
[212] P. Gourgiotis, T. Zisis, K.P. Baxevanakis, International Journal of Solids and Structures, 85 (2016) 34-43.
[213] S. Chu, J. Li, Journal of Materials Science, 12 (1977) 2200-2208.
[214] J.C. Li, Materials Science and Engineering: A, 322 (2002) 23-42.
[215] Y.C. Lu, S.N. Kurapati, F. Yang, Journal of Physics D: Applied Physics, 41 (2008) 115415.
[216] P. Sargent, M. Ashby, Scripta metallurgica, 18 (1984) 145-150.
[217] C.R. Weinberger, W. Cai, Proceedings of the National Academy of Sciences, 105 (2008) 14304-14307.
[218] W.D. Nix, S.-W. Lee, Philosophical Magazine, 91 (2011) 1084-1096.
[219] J.R. Greer, W.D. Nix, Physical Review B, 73 (2006) 245410.

VITA

Yikai Wang

Education

Ph.D. candidate, Materials Science and Engineering, University of Kentucky, Lexington, KY, USA (Advisor: Prof. Yang-Tse (YT) Cheng) 08/2015 –05/2019
M.S., Materials Science & Engineering, Central South University, China 09/2012 – 06/2015
B.S., Material Chemistry, Central South University, China 09/2008 – 06/2012

Research Experience

Research assistant, University of Kentucky 01/2018 – Now
Intern, National Renewable Energy Laboratory (NREL), Golden, CO 10/2018 – 12/2018
Research assistant, University of Kentucky 06/2016 – 09/2018
Teaching assistant, University of Kentucky 01/2016 – 05/2016
Research assistant, University of Kentucky 08/2015 – 12/2015

Scientific and Professional Society

President, Materials Research Society (MRS) – UK Chapter 04/2017 – 04/2018
Student member, Materials Research Society (MRS) 04/2017 – 12/2019
Student member, The Electrochemical Society (ECS) 04/2016 – 05/102
Student member, Society for Experimental Mechanics (SEM) 12/2017 – 12/2018
Student member, Materials Science & Technology (MS&T) 10/2018 –10/2019

Awards

The 2nd place in the poster competition of MACE Spring Symposium 05/2018
Travel award, Graduate Student Congress, University of Kentucky 05/2018
Outstanding MSE Graduate Students, University of Kentucky 04/2019

Publication List

- **Peer-reviewed journal papers**

24. **Yikai Wang**, Dingying Dang, Ming Wang, Xingcheng Xiao, Yang-Tse Cheng. "Mechanical Behavior of Electroplated Mossy Lithium at Room Temperature Studied by Flat Punch Indentation." Applied Physics Letters *(2019, accepted).*

23. **Yikai Wang**, Dingying Dang, Dawei Li, Jiazhi Hu, Xaiowen Zhan, Yang-Tse Cheng. "Effects of Polymeric Binders on the Cracking Behavior of Silicon Composite Electrodes during Electrochemical Cycling", *Under review.*

22. **Yikai Wang**, Dingying Dang, Dawei Li, Jiazhi Hu, Yang-Tse Cheng. "Influence of polymeric binders on mechanical properties and microstructure evolution of silicon composite electrodes during electrochemical cycling." *Journal of Power Sources 425 (2019): 170-178.*

21. Yoon, Taeho, Chuanxiao Xiao, Jun Liu, **Yikai Wang**, Seoungbum Son, Anthony Burrell, and Chunmei Ban. "Electrochemically induced fractures in crystalline silicon anodes." *Journal of Power Sources 425 (2019): 44-49.*

20. Sun, Yan, Xiaowen Zhan, Jiazhi Hu, **Yikai Wang**, Shuang Gao, Yuhua Shen, and Yang-Tse Cheng. "Improving ionic conductivity with bimodal-sized Li7La3Zr2O12 fillers for composite polymer electrolytes." *ACS Applied Materials & Interfaces 11 (13), 12467–12475* (2019).

19. Wenqi Li, Yan Zhang, Lalitendu Das, **Yikai Wang**, Mi Li, Namal Wanninayake, Yunqiao Pu, Doo Young Kim, Yang-Tse Cheng, Arthur J Ragauskas, Jian Shi. "Linking lignin source with structural and electrochemical properties of lignin-derived carbon materials." *RCS Advances* 8(68): 38721-38732 (2018)

18. **Yikai Wang**, Qinglin Zhang, Dawei Li, Jiazhi Hu, Jiagang Xu, Dingying Dang, Xingcheng Xiao, Yang-Tse Cheng. "Mechanical property evolution of silicon composite electrodes studied by environmental nanoindentation." *Advanced Energy Materials* 8 (10): 1702578 (2018)

17. Jiazhi Hu, **Yikai Wang**, Dawei Li, Yang-Tse Cheng. "Effects of adhesion and cohesion on the electrochemical performance and durability of silicon composite electrodes." *Journal of Power Sources* 397: 223-230 (2018)

16. Dawei Li, **Yikai Wang**, Jiazhi Hu, Bo Lu, Dingying Dang, Junqian Zhang, Yang-Tse Cheng. "Role of polymeric binders on mechanical behavior and cracking resistance of silicon composite electrodes during electrochemical cycling." *Journal of Power Sources* 387: 9-15 (2018)

15. Meysam Haghshenas, **Yikai Wang**, Yang-Tse Cheng, Manoj Gupta. "Indentation-based rate-dependent plastic deformation of polycrystalline pure magnesium." *Materials Science and Engineering: A* 716: 63-71 (2018)

14. Yufeng Huang, Wensheng Liu, Yunzhu Ma, **Yikai Wang**, Siwei Tang. "Effects of cooling rate and magnetic field on solidification characteristics of Au80Sn20 eutectic solder." *Journal of Materials Science: Materials in Electronics* 29 (1): 436-445 (2018)

13. Seoung-Bum Son, **Yikai Wang**, Jiagang Xu, Xuemin Li, Markus Groner, Adam Stokes, Yongan Yang, Yang-Tse Cheng, Chunmei Ban. "Systematic investigation of the alucone-coating enhancement on silicon anodes." *ACS Applied Materials & Interfaces* 9 (46): 40143-40150 (2017)

12. Dawei Li, **Yikai Wang**, Jiazhi Hu, Bo Lu, Yang-Tse Cheng, Junqian Zhang. "*In situ* measurement of mechanical property and stress evolution in a composite silicon electrode." *Journal of Power Sources* 366: 80-85 (2017)

11. **Yikai Wang**, Yang-Tse Cheng. "A nanoindentation study of the viscoplastic behavior of pure lithium." *Scripta Materialia* 130: 191-195 (2017)

10. Jiagang Xu, Long Zhang, **Yikai Wang**, Tao Chen, Mohanad Al-Shroofy, Yang-Tse Cheng. "Unveiling the critical role of polymeric binders for silicon negative electrodes in lithium-ion full cells." *ACS Applied Materials & Interfaces* 9 (4): 3562-3569 (2017)

9. Yunzhu Ma, Tong Wu, Wensheng Liu, Yufeng Huang, Siwei Tang, **Yikai Wang**. "Interfacial microstructure evolution and shear behavior of Au–12Ge/Ni solder joints during isothermal aging." *Journal of Materials Science: Materials in Electronics* 28 (4): 3685-3694 (2017)

8. Wensheng Liu, **Yikai Wang**, Yunzhu Ma, Yufeng Huang, Qiang Yu. "Interfacial reaction mechanism and kinetics between Au–20Sn and Sn." *Journal of Materials Science: Materials in Electronics* 27 (6): 5982-5991 (2016)

7. Wensheng Liu, **Yikai Wang**, Yunzhu Ma, Qiang Yu, Yufeng Huang. "Nanoindentation study on micromechanical behaviors of Au–Ni–Sn intermetallic layers in Au–20Sn/Ni solder joints." *Materials Science and Engineering: A* 653: 13-22 (2016)

6. Wensheng Liu, **Yikai Wang**, Yunzhu Ma, Qiang Yu, Yufeng Huang. "Interfacial microstructure evolution and shear behavior of Au–20Sn/(Sn) Cu solder joints bonded at 250℃." *Materials Science and Engineering: A* 651: 626-635 (2016)

5. Yunzhu Ma, Huiting Luo, Yongjun Li, Wensheng Liu, **Yikai Wang**, Boyun Huang. "Formation and evolution of intermetallic compounds between the In-3Ag solder and Cu substrate during soldering." *Journal of Materials Science: Materials in Electronics* 26 (10): 7967-7976 (2015)

4. Fan Cheng, Wensheng Liu,Juan Wang, **Yikai Wang**. "Research progress of Ag_3PO_4-based photocatalyst: Fundamentals and performance enhancement." *Transactions of Nonferrous Metals Society of China* 25 (1): 112-121 (2015)

3. **Yikai Wang**, Wensheng Liu, Yunzhu Ma, Yufeng Huang, Ya Tang, Huiting Luo, Qiang Yu. "Indentation depth dependent micromechanical properties and rate dependent pop-in events of $(Au, Cu)_5Sn$." *Materials Letters* 131: 57-60 (2014)

2. **Yikai Wang**, Wensheng Liu, Yunzhu Ma, Yufeng Huang, Ya Tang, Fan Cheng, Qiang Yu. "Indentation size effect and micromechanics characterization of intermetallic compounds in the Au–Sn system." *Materials Science and Engineering: A* 610: 161-170 (2014)

1. Wensheng Liu, **Yikai Wang**, Yunzhu Ma, Yufeng Huang, Ya Tang, Fan Cheng. "Indentation size effect of stress exponent and hardness in homogeneous duplex eutectic 80Au/20Sn." *Materials Letters* 120: 151-154 (2014)

- **6 technical presentations in professional conferences/meetings**

6. **Yikai Wang**, Dingying Dang, Jiazhi Hu, Xingcheng Xiao, Tang-Tse Cheng. “Role of polymeric binders in the degradation of silicon composite electrodes.” 2018 MRS Fall Meeting, Boston, MA, 11/2018 (Abstract NO. 3039885, Oral Presentation)

5. **Yikai Wang**, Xingcheng Xiao, Yang-Tse Cheng. “Time-dependent mechanical properties of Li metal studied by nanoindentation.” 2018 MS&T, Columbus, OH, 10/2018 (Abstract NO. 18-9655, Oral Presentation)

4. **Yikai Wang**, Dingying Dang, Ming Wang, Xingcheng Xiao, Yang-Tse Cheng. “Mechanical behavior of Li metal electrodes studied by environmental nanoindentation.” 2018 Beyond Lithium Ion XI, Cleveland, OH, 07/2018 (Poster)

3. **Yikai Wang**, Yang-Tse Cheng. “Environmental nanoindentation for lithium-ion battery research” 2018 Annual Meeting of Society for Experimental Mechanics, Greenville, SC, 06/2018 (Abstract NO. 499, Oral Presentation)

2. **Yikai Wang**, Qinglin Zhang, Dawei Li, Jiazhi Hu, Jiagang Xu, Dingying Dang, Xingcheng Xiao, Yang-Tse Cheng. “Mechanical properties and microstructure evolution of silicon composite electrodes.” 233rd ECS Meeting, Seattle, WA, 05/2018 (Abstract NO. 1953, Oral Presentation)

1. **Yikai Wang**, Yang-Tse Cheng, “Determining viscoplastic properties of lithium metal by nanoindentation.” 2017 MRS Spring Meeting, Phoenix, AZ, 04/2017 (Abstract NO. ES6.10.04, Oral Presentation)